***Regional-Scale Modeling at NASA Goddard Space Flight Center***

W.-K. Tao[1], R. Adler[1], D. Baker[2], S. Braun[1], M.-D. Chou[1], M. F. Jasinski[3], Y. Jia[4], R. Kakar[5], M. Karyampudi[6], S. Lang[4], W. Lau[1], B. Lynn[7], Z.-X. Pu[8], M. Shepherd[1], J. Simpson[1], D. Starr[1], Y. Wang[8], P. Wetzel[1], and J. Weinman[3]

[1]*Laboratory for Atmospheres*
*NASA Goddard Space Flight Center*
*Greenbelt, MD 20771*

[2]*Physics Department*
*Austin College*
*Sherman, TX 75090*

[3]*Laboratory for Hydrospheric Processes*
*NASA Goddard Space Flight Center*
*Greenbelt, MD 20771*

[4]*Science Systems and Applications Inc.*
*NASA Goddard Space Flight Center*
*Greenbelt, MD 20771*

[5]*NASA/Headquarters*
*Washington DC*

[6]*NCEP/Environmental Modeling Centers*
*Washington, D. C. 20233*

[7]*Department of Atmospheric Science*
*Hebrew University of Jerusalem*
*Jerusalem, Israel*

[8]*Goddard Earth Sciences and Technology Center*
*University of Maryland, Baltimore County*
*Baltimore, MD*

"Recent Research Developments in Atmospheric Science"
*Research Signpost*

(December 2002)

Corresponding author address: Dr. Wei-Kuo Tao, Mesoscale Atmospheric Processes Branch, Code 912, NASA GSFC, Greenbelt, MD 20771
email: tao@agnes.gsfc.nasa.gov

*Regional-Scale Modeling at NASA Goddard Space Flight Center*

W.-K. Tao, R. Adler, D. Baker, S. Braun, M.-D. Chou, M. F. Jasinski, Y. Jia, R. Kakar, M. Karyampudi, S. Lang, W. Lau, B. Lynn, Z.-X. Pu, M. Shepherd, J. Simpson, D. Starr, Y. Wang, P. Wetzel, and J. Weinman

Submitted to "Recent Research Developments in Atmospheric Science"
*Research Signpost*

## Popular Summary

Over the past decade, the Goddard Mesoscale Modeling and Dynamics Group has used a popular regional scale model, MM5, to study precipitation processes. Our group is making contributions to the MM5 by incorporating the following physical and numerical packages: improved Goddard cloud processes, a land processes model (Parameterization for Land-Atmosphere-Cloud Exchange - PLACE), efficient but sophisticated radiative processes, conservation of hydrometeor mass (water budget), four-dimensional data assimilation for rainfall, and better computational methods for trace gas transport.

At NASA Goddard, the MM5 has been used to study: (1) the impact of initial conditions, assimilation of satellite-derived rainfall, and cumulus parameterizations on rapidly intensifying oceanic cyclones, hurricanes and typhoons, (2) the dynamic and thermodynamic processes associated with the development of narrow cold frontal rainbands, (3) regional climate and water cycles, (4) the impact of vertical transport by clouds and lightning on trace gas distribution/production associated with South and North American mesoscale convective systems, (5) the development of a westerly wind burst (WWB) that occurred during the TOGA COARE and the diurnal variation of precipitation in the tropics, (6) a Florida sea breeze convective event and a Mid-US flood event using a sophisticated land surface model, (7) the influence of soil heterogeneity on land surface energy balance in the southwest GCIP region, (8) explicit simulations (with 1.33 to 4 km horizontal resolution) of hurricanes Bob (1991) and Bonnie (1998), (9) a heavy precipitation event over Taiwan, and (10) to make real time forecasts for a major NASA field program. In this paper, the modifications and simulated cases will be reviewed and discussed.

## ABSTRACT

Over the past decade, the Goddard Mesoscale Modeling and Dynamics Group has used a popular regional scale model, MM5, to study precipitation processes. Our group is making contributions to the MM5 by incorporating the following physical and numerical packages: improved Goddard cloud processes, a land processes model (Parameterization for Land-Atmosphere-Cloud Exchange - PLACE), efficient but sophisticated radiative processes, conservation of hydrometeor mass (water budget), four-dimensional data assimilation for rainfall, and better computational methods for trace gas transport.

At NASA Goddard, the MM5 has been used to study: (1) the impact of initial conditions, assimilation of satellite-derived rainfall, and cumulus parameterizations on rapidly intensifying oceanic cyclones, hurricanes and typhoons, (2) the dynamic and thermodynamic processes associated with the development of narrow cold frontal rainbands, (3) regional climate and water cycles, (4) the impact of vertical transport by clouds and lightning on trace gas distribution/production associated with South and North American mesoscale convective systems, (5) the development of a westerly wind burst (WWB) that occurred during the TOGA COARE and the diurnal variation of precipitation in the tropics, (6) a Florida sea breeze convective event and a Mid-US flood event using a sophisticated land surface model, (7) the influence of soil heterogeneity on land surface energy balance in the southwest GCIP region, (8) explicit simulations (with 1.33 to 4 km horizontal resolution) of hurricanes Bob (1991) and Bonnie (1998), (9) a heavy precipitation event over Taiwan, and (10) to make real time forecasts for a major NASA field program. In this paper, the modifications and simulated cases will be described and discussed.

## 1. INTRODUCTION

The interactions of thunderstorms and mesoscale convective systems with their environment is an important link in a chain of regional and global processes responsible for monsoons, the Baiu frontal depression, tropical cyclones, El Nino-Southern Oscillation (ENSO) events [i.e., super cloud clusters (SSCs) and westerly wind bursts WWBs)] and other climate variations (e.g., 30-60 day intra-seasonal oscillations). Convective systems can also play a crucial role in the earth's radiation budget and in interactions with ocean and land characteristics. Computer models provide essential insights into the interactions between clouds and/or convective systems and their surroundings. Numerical models are also used in the development and refinement of space-borne retrievals.

The Goddard Cumulus Ensemble (GCE) Model[1], a cloud-resolving model, the Penn State/NCAR Mesoscale Model Version 5 (MM5), a regional-scale model, and various synoptic-scale model analyses are being used to study the physical and dynamical processes associated with tropical cyclones, mesoscale convective systems (MCSs) and frontal rainbands in various geographic locations by the Goddard Mesoscale Dyanmics and Modeling Group. The main missions of the Goddard Mesoscale Dynamics and Modeling Group are:

o To understand the role of precipitation processes, their interaction with the surface, their influence on regional and global hydrological cycles with regard to climate variations, and their contribution to the energy budget;

o To help development and refine space-borne retrievals;

o To use observations from both field campaigns and satellite missions to improve simulations and forecasts of severe weather events such as MCSs, fronts, monsoons, cyclones, and hurricanes;

o To improve the representation of moist processes as well as their interaction with radiation and their effect on transporting chemical species in global and climate models;

o To assess the effects of assimilating satellite-derived fields (i.e., rainfall) on the prediction and forecasting of tropical and midlatitude precipitation systems.

These missions are closely related to the NASA Earth Science Enterprise (ESE), NASA satellite missions (i.e., the Tropical Rainfall Measuring Mission - TRMM, and the Global Precipitation Mission - GPM), the GEWEX Cloud System Study (GCSS), the U.S. Weather Research Program (USWRP), and Weather Research Forecast (WRF) model development.

Over the past seven to eight years, the Goddard Mesoscale Dyanmics and Modeling Group has gained extensive experience in the use of MM5. The MM5 is a meso-alpha (200-

---

[1] The GCE Model has been developed and improved at NASA Goddard Space Flight Center over the past two decades. Improvements and testing were presented in [106, 109]. A review on the application of the GCE model to the understanding of precipitation processes can be found in [92, 104].

2000km) and meso-beta (20-200km) scale primitive equations model, and its non-hydrostatic version (MM5) is described by [32, 41]. It uses finite differences (second-order for advection and fourth-order for diffusion) and a time-splitting scheme to solve prognostic equations [i.e., horizontal and vertical momentum (u, v and w), pressure perturbation (p'), temperature (T) and water vapor (qv)] on an Arakawa-B staggered grid with a terrain-following vertical coordinate. The time-splitting scheme uses two steps: a large one which employs a leapfrog scheme with an Asselin filter to integrate slow moving meteorological waves and a small one which employs a semi-implicit scheme to integrate faster moving acoustic waves. In additional, MM5 has both a cumulus parameterization scheme and a simple explicit moisture scheme which can be activated simultaneously in the model. MM5 has a reliable front-end pre-processor to provide realistic initial conditions from NCEP and ECMWF analyses. Running non-hydrostatically with multiple, nested grids, the model can resolve down to a few kilometers and is an excellent tool for studying multi- scale dynamics associated with precipitation processes as well as their impact on regional hydrological cycles. MM5 has been used to study scientific problems including real-time weather forecasting, four-dimensional data assimilation, and severe storms research (see a review given in [1]). These MM5 studies have shown that a mesoscale model with realistic treatments of surface topography and physical processes (i.e., moist convective and surface processes), and initialized with good large-scale conditions, is capable of simulating and predicting a variety of synoptic and mesoscale phenomena in different parts of the world.

This article describes the new improvements and options made to the physics (i.e., microphysics, radiation, land surface processes and air-sea interaction) of the MM5 at NASA Goddard Space Flight Center (GSFC). Some of these new options will be available through NCAR or PSU to MM5 users. In addition, this article also describes the application of the MM5 at Goddard to the following scientific problems: **i)** the effects of land- and ocean-surface processes on precipitation processes and their roles in the water cycle and regional climate variations (simulations); **ii)** the vertical redistribution of trace constituents by convective clouds/systems over continental scales; **iii)** the physical processes that contribute to deepening of hurricanes and the factors that could help or hinder our ability to accurately simulate these storms; **iv)** the effects of assimilating satellite-derived fields (i.e., water vapor, temperature, wind, precipitation and latent heating profiles) on simulations of tropical and extratropical convective systems; **v)** the processes that determine the westerly wind burst and diurnal variation of precipitation in the tropics; **vi)** the impact of soil/vegetation on convective systems and flood events; **vii)** the influence of soil heterogeneity on the partitioning of land surface fluxes in the southwest GCIP region; **viii)** the dynamic processes associated with narrow cold frontal rainbands; **ix)** the precipitation processes associated with heavy rainfall over Taiwan; and **x)** a real time forecast system for a major NASA field campaign program in and around the Florida peninsula.

## 2. NEW MM5 PHYSICAL MODULES DEVELOPED AT NASA GSFC

A mesoscale (MM5) model that allows for various grid resolutions can be used to study multiscale interactions associated with atmospheric circulation. In order to realistically simulate tropical/midlatitude precipitation systems and their role in the regional hydrological cycle, the model must have well-founded representations of microphysical, atmospheric

radiative, land-soil-vegetation-surface and air-sea interactive processes. Over the last decade, several of these physical processes have been developed, tested and incorporated into the GCE model (e.g., [106, 109]). In addition, these new and sophisticated physical modules have been implemented into and tested in the MM5 model. Table 1 shows the major characteristics of MM5 including the processes modified at Goddard.

| Parameters/Processes | Penn State/NCAR MM5 |
|---|---|
| Vertical Coordinate | sigma-p (z) |
| Explicit Convective Processes | 1-2 class water & 1-2 class ice<br>***3 ice scheme**** |
| Implicit Convective Processes | Cumulus Parameterization<br>Schemes |
| Numerical Methods | Leapfrog in Time and 2nd Order Scheme in Advection for both Scalar and Dynamic Variables<br>***Off-line positive definite transport**** |
| Initialization | *Goddard DAO**, NCEP and ECMWF Analyzed (and/or Bogus) Data |
| FDDA | Nudging/Adjoint<br>***Rainfall**** |
| Radiation | Emissivity Method in LW<br>***Goddard k-distribution and four-stream discrete-ordinate scattering (8 bands)**** |
| Sub-Grid Diffusion | Smagorinski |
| Planetary Boundary Processes | Blackadar PBL or Dry Convective Adjustment<br>*TKE (PSU)** |
| Topography | Sigma-p (z) |
| Two-Way Interactive Nesting | Traditional but with Monotonic Interpolation |
| Surface Energy Budget | Force-restore Method or<br>***7-Layer Soil Model (PLACE)**** |

**Table 1** Characteristics of the PSU/NCAR MM5. Processes modified by the Goddard Mesoscale Modeling and Dynamics Group are marked with an *.

### *2.1 The Goddard Cloud Microphysics Module*

A two-class liquid and three-class ice microphysical scheme developed and coded by [105, 106] has already been implemented into MM5. The microphysical scheme implemented into MM5 was mainly based on [64] with additional processes from [89]. However, the Goddard microphysical scheme has several modifications. The first modification is the option to choose either graupel or hail as the third class of ice (e.g., [74]). Graupel has a low density and a large intercept (i.e., high number concentration). In contrast, hail has a high density and a small intercept (i.e., low number concentration). These differences can affect not only the description of the hydrometeor population, but also the relative importance of the microphysical-dynamical-radiative processes. Second, a saturation technique was implemented following [107]. This saturation technique is basically designed to ensure that supersaturation (subsaturation) cannot exist at a grid point that is clear (cloudy). This saturation technique is one of the last microphysical processes to be computed. It is only done prior to evaluating the evaporation of rain and deposition or sublimation of

snow/graupel/hail[2]. A third difference is that all microphysical processes (transfer rates from one type of hydrometeor to another) are calculated based on one thermodynamic state. This ensures that all processes are treated equally. The opposite approach is to have one particular process calculated first modifying the temperature and water vapor content (i.e., through latent heat release) before the second process is computed. The fourth difference is that the sum of all the sink processes associated with one species will not exceed its mass. This ensures that the water budget will be balanced in the microphysical calculations.

A two-class ice cloud microphysics scheme [31] is a standard option for the resolvable-scale convection. This scheme allows for simple ice-phase processes. Cloud water becomes cloud ice and rain water becomes snow when the temperature is below the freezing point. This cloud scheme has been designed and used mainly for coarse grid resolutions in MM5.

### *2.2 Goddard Radiative Processes Module*

The interaction between clouds and radiation is two-way. On the one hand, clouds can reflect incoming solar and outgoing long-wave radiation. On the other hand, radiation can enhance or reduce cloud activity. Differential cooling between cloudy and clear regions can enhance cloud activity in the cloudy region [39]. Longwave radiation cools the stratiform cloud top but warms the stratiform cloud base [29]. As a result, longwave radiation can destabilize the stratiform cloud layer. This destabilization was quite an important process in the light precipitation region during WMONEX [123]. Furthermore, the effects of radiation on the growth and sublimation rates of ice particles can be significant [99]. Particle growth is enhanced (suppressed) in a radiatively cooled (heated) environment. Radiative cooling could also destabilize the large-scale environment [31]. Cloud-radiation interaction can also have a major impact on the diurnal variation of precipitation processes over the tropics. For example, two different (thermodynamic and dynamic) mechanisms responsible for the diurnal variation of precipitation over tropical oceans have been proposed. The thermodynamic response of clouds to radiative heating (cloud development is reduced by solar heating and enhanced by IR cooling) can be the main mechanism responsible for the diurnal variation of precipitation [e.g., 55, 86]. On the other hand, [39] indicated that the large-scale dynamic response to the radiational differences between cloudy and clear regions was the main mechanism.

The Goddard radiative transfer package [22, 23, 26] was recently implemented into MM5. This radiation scheme is a broad- band model and is considered state-of-the-art in the General Circulation Modeling (GCM) community (the UCLA GCM, Goddard GCM, CSU GCM and FSU global model have all adopted this radiative scheme). The shortwave radiation model [24, 25] is used to compute solar heating in the atmosphere/clouds and at the surface. The solar spectrum is divided into two regions: the ultraviolet (UV) and visible region (wavelengths $< 0.69$ um) and the near infrared (IR) region (wavelengths $> 0.69$ um). In

[2] Melting processes of snow and graupel/hail are calculated after all these transfer processes. Other exceptions are the processes associated with water vapor directly (i.e., evaporation of rain is calculated after the saturation adjustment).

the UV and visible spectral region, ozone absorption and Rayleigh and cloud scattering are included. In the near IR region, absorption due to water vapor, cloud, CO2 and O2, and scattering due to clouds are included. The UV and visible region is further grouped into four bands, and an effective ozone absorption coefficient and an effective Rayleigh scattering coefficient are given for each band. The near IR region is divided into seven water vapor absorption bands. The k-distribution method is applied to each of the seven bands for computing the absorption of solar radiation by water vapor and clouds. The four-stream discrete-ordinate scattering algorithm [66] is used to compute multiple scattering within a cloud layer. The simple scattering albedos for each of the seven near IR bands are taken from [54].

The Goddard longwave radiation model [27] is used to compute cloud and atmospheric infrared cooling. The IR spectrum is divided into eight bands. The water vapor transmission function is computed using the k-distribution method, and the CO2 and O3 transmission functions are computed using look-up tables. The absorption due to cloud hydrometeors is also included. Clouds are assumed to be gray and non-scattering. The multiplication approximation is used to take into account the effect of overlapping of different gas and cloud absorption. Use of a fully explicit microphysics scheme (liquid and ice) and a fine horizontal resolution (5 km or less) can give realistic cloud optical properties and cloudiness which are crucial for determining the radiation budgets with less tuning.

The standard MM5 atmospheric radiation model includes longwave (infrared) and shortwave (visible) parameterizations that interact with the atmosphere (e.g., [31]). This scheme uses a broad-band two-stream (upward and downward fluxes) approach for the radiative flux calculations. Its longwave radiation scheme is an emissivity-type (which uses a pre-calculated emissivity function to represent the frequency integrated absorption spectrum of water vapor weighted by a suitable envelope function). MM5's shortwave radiation scheme takes into account the effect of the solar zenith angle, clouds having their own albedo and absorption coefficient, and clear air (scattering and water vapor absorption).

### *2.3 Goddard Land-Soil-Vegetation-Surface Processes (PLACE)*

The land and atmosphere form a highly coupled system. Surface convective fluxes are coupled to the net surface radiative flux, the vegetation state, and the profiles of temperature and water below the surface and up through the atmospheric planetary boundary layer. These processes at the land-atmosphere interface are influenced in a fundamental way by topographic features and the heterogeneous character of the land surface layer. The fluxes of heat and moisture across the interface vary on spatial scales ranging from meters to thousands of kilometers. Modeling these coupled surface-atmospheric processes is crucial to the understanding and simulation of climate system interactions. A detailed soil-vegetation land model was recently implemented into MM5 to study precipitation processes that involve the interaction between land and atmosphere.

The PLACE model (Parameterization for Land-Atmosphere Cloud Exchange) has recently been incorporated into MM5 as an option via coupling with four popular boundary layer options: the Blackadar high resolution PBL, the MRF model, a simple O'Brien K-

profile boundary layer, and the Seaman-Stauffer TKE boundary layer. PLACE is a detailed interactive process model of the heterogeneous land surface (soil and vegetation) and adjacent near-surface atmosphere. PLACE basically consists of three elements. These are: (i) a soil module that includes at least seven water reservoirs (i.e., plant internal storage, dew/intercepted precipitation, surface material (no roots), a topsoil root layer, a subsoil root layer, and two deeper layers that regulate seasonal and interannual variability of the soil hydrology); (ii) a surface slab of vegetation, litter and other loose material which shades the soil and acts as the source for sensible heat flux, and which intercepts precipitation and dew; and (iii) the surface layer of the atmosphere (up to the lowest computational level of the model to which it is coupled) within which the fluxes of sensible heat and water vapor are calculated. More details on PLACE can be found in [124]. PLACE has been an active participant in two major international intercomparison projects sponsored by the World Climate Research Project (WCRP)/GEWEX: the Project for the Intercomparison of Land surface Parameterization Schemes (PILPS, see [42, 43]) and the Global Soil Wetness Project (GSWP, see [8]). These studies have demonstrated that PLACE is as accurate as other widely used land-surface schemes in GCMs, such as BATS. However, PLACE has been specifically designed to be applied to mesoscale models with grid resolutions of 100 km or smaller. PLACE was linked to the GCE model to study the impact of soil moisture patches and atmospheric boundary conditions on cloud structure, rainfall, and soil moisture distribution [67]. The performance of coupled MM5-PLACE on sea-breeze generated deep convection over the Florida peninsula during the Convection and Precipitation Electrification Experiment (CaPE) was tested [67]. They indicated that land processes, initial soil moisture and the planetary boundary layer could have a major influence on the sea breeze, lake breezes and moist convection.

A simple surface model in which the surface temperature is computed from a surface energy budget following the "force-restore" method developed by Blackadar [126] has also been used in MM5. This surface model is termed the SLAB model in MM5.

### *2.4 Goddard Cloud-Chemistry Tracer Transport Module*

A Multi-dimensional Positive Definite Advection Transport Algorithm (MPDATA) [95, 96] with a non-oscillatory option [97] was recently implemented into MM5. In the cloud-chemistry tracer transport module, the four-dimensional wind as well as cumulus parameterization schemes from MM5 are used to estimate tracer transport by cloud systems in regional-scale simulations [109]. The basic numerical method for solving the continuity equation of trace gases is forward in time and upstream differencing in space. The upstream scheme will not introduce negative values in the solution as would second- or fourth-order horizontal advection, but it can suffer from excessive numerical diffusion. An iterative method which can reduce the implicit diffusion by introducing a second ``upstream" step was developed [95]. This modified upstream scheme (termed the positive definite advection scheme) has been improved with a multi-dimensional application [96] and a non-oscillatory option [97]. This scheme has been tested in MM5 and has produced features in better agreement with observational studies in terms of the redistribution of trace gases by convective cells associated with several different MCSs (see [109]). This cloud-chemistry tracer transport module can also be coupled with a cumulus parameterization scheme and a

photo-chemistry module (see a review given in [115]).

### *2.5 Water Budget Adjustment*

The temporal differencing used in MM5 consists of leapfrog steps with an Asselin filter. A centered finite difference method is used for advection. It is well known that these difference methods can generate negative mass for hydrometeors near and at cloud boundaries. The adjustment used in MM5 is to reassign all negative hydrometeors to be zero. This can cause an imbalance in the water budget. Note that the error grows with the number of time iterations not the length of model integration.

To remedy this shortcoming (especially for long term model integration and for fine model resolution simulations), a mass conservation-adjustment scheme was implemented into MM5. The procedure for this mass conservation scheme for all hydrometeors is as follows: (i) compute the total positive mass (P) and negative mass (N) over the entire domain, (ii) set all negative mass to be zero, and (iii) recompute the positive mass by multiplying by a factor of (P-N)/P. This type of adjustment has been used in many cloud-scale models (i.e., [98]; the GCE model, and many others).

### *2.6 Four-Dimensional Data Assimilation (FDDA)*

At Goddard, MM5 has been used to assess the impact of initial conditions and the assimilation of satellite-derived rainfall rates (synthesized SSM/I-GOES/IR- and TRMM-derived rainfall rates) and vertical latent heating profiles on the simulations of tropical cyclones. The rainfall assimilation-nudging technique was first developed at Goddard [72] with a few minor modifications [53].

Large-scale rainfall distributions are most effectively measured by means of microwave (i.e., SMM/I) radiometry. Unfortunately microwave radiometers are confined to low orbiting satellites that only provide intermittent snapshots of rainfall and integrated liquid water (ILW). A "morphing" technique [3] was employed to assimilate satellite-derived rainfall data assimilation. Morphing is an image processing technique that smoothly metamorphes one image into another. This is achieved by identifying tie points, such as the center of a cyclone and features of a squall line, in two successive images that may be separated by several hours. A bi-cubic coordinate transformation distorts the first image to match the second in a least square sense. A backward transformation also is used to transform the second image to the first. The coefficients in both bi-cubic transformations are then interpolated in time. The magnitudes of the integrated liquid water (ILW) and/or rainfall rate in each distorted grid element are also interpolated to produce a smooth interpolation from one image to the next.

Two additional major improvements have been made during the past three years. The first one was the introduction of mesoscale bogus vortices, which are generated by four-dimensional variational data assimilation (4DVAR) using the MM5 adjoint system [129] into the initial conditions for hurricane simulations [82]. The second one was to apply the 4DVAR adjoint technique on TRMM-retrieved rainfall data to improve the initial conditions

[83].

## 3. APPLICATIONS

### *3.1 Regional Water and Energy Cycles*

A Regional Land-Atmosphere Climate Simulation (RELACS) System is being developed and implemented at NASA Goddard Space Flight Center. One of the major goals of RELACS is to use a regional-scale model (MM5) with improved physical processes, in particular land-related processes, to understand the role of the land surface and its interaction with convection and radiation as well as the water and energy cycles in Indo-China, the South China Sea (SCS), China, N. America and S. America. The RELACS is typically run within a domain covering 6000-8000 km by 6000-8000 km using interactive nesting techniques with two grid resolutions (60- and 20-km, respectively). The South China Sea Monsoon Experiment (SCSMEX) was conducted in May-June 1998 and can provide observations for model validation. Multiple observation platforms (e.g., soundings, Doppler radar, ships, wind profilers, radiometers, etc.) during SCSMEX provided a first attempt at investigating the detailed characteristics of convection and circulation changes associated with monsoons over the South China Sea region [60].

(a) Mechanisms of Torrential Rain Associated with the Mei-Yu Development during SCSMEX

The RELACS has been used to simulate the Yantze River flood in June 1998 (from June 13 to 19). The model results showed that there are two major physical processes associated with Mei-Yu precipitation over central China [85]. The first one is the local effect of the land surface. Two experiments, one allowing full interaction between precipitation and surface evaporation via the PLACE and the other one not, were conducted. In the second experiment (NF), precipitation is assumed to completely and immediately run off without having any impact on soil moisture or vegetation. The results suggested that storms responsible for the rainfall are themselves critical to the development and maintenance of the front. The heat released by the storms acts to increase the wind speed of the low-level jet (LLJ), providing a positive feedback that sustains the storm system along the Mei-yu front. It was also found that local precipitation recycling shifts heavy rain toward the warm side of the front. The shift is due to the pronounced increase of atmospheric moisture and decrease in surface temperature on the warm side of the front and allows the model to better predict the Mei-Yu front itself (Fig. 1).

The next step was to determine the remote moisture sources that physically accounted for the Mei-yu precipitation/flood. Sensitivity tests reducing the atmospheric water vapor fluxes from the western, southern and eastern lateral boundaries, were performed. Results indicated that Mei-Yu precipitation is basically determined by moisture transported from the Bay of Bengal through Indo-China. The moisture was transported out of the southwest by a strong LLJ. There was very little impact do to moisture transported from the South China Sea and the Pacific Ocean.

In addition, the model results were very sensitive to the cumulus parameterization schemes used in MM5. The Betts-Miller scheme [7] produced too much rainfall over the East Coast of China. The Kain-Fritsch scheme [52], on the other hand, simulated rainfall in good agreement with observations.

(b) On set of the South China Sea Monsoon

The onset of the South China Sea monsoon (SCSM) in 1997 and 1998 has also been studied using RELACS [121]. In both 1997 and 1998, signals for the onset of the monsoon were strong. The pre-onset was associated with the development of a "double cyclone" in the Bay of Bengal. The northern cyclone strengthened and the southern dissipated. When the northern cyclone reached the northwest part of the Indo-China Peninsula, it spun up a strong southwestly flow across the peninsula. The onset of the monsoon in both cases coincided with the arrival of strong southwest winds in the South China Sea.

However, the onset of the 1997 and 1998 monsoon is different in the following ways. First, the penetration of southwesterly winds into the SCS is much stronger in 1997. The onset is also much more abrupt than in 1998. The strong southwestly winds completely pushed the west Pacific high pressure system out the SCS region during the first two days of the onset (May 19-20) in 1997. Secondly, the northern cold front from southern China was also stronger than that in 1998. And third, the precipitation was much more intense in 1997 during the onset period.

A series of two-week numerical experiments were carried out to study the effects of local land-cover changes on convective activity over Indo-China and the South China Sea during the May 18 to May 29, 1997 monsoon period. The temporal variation of simulated rainfall compared well with Global Precipitation Climatology Project (GPCP)[3] estimates (Fig. 2). The maximum rainfall that occurred on May 24 and 25 was well simulated. The run without PLACE produced more rainfall compared to GPCP, and its maximum occurred on May 25. Sea surface temperature (SST) variation only had a small impact on rainfall[4]. For the 1998 case, the RELACS simulated rainfall can be compared with TRMM[5] and GPCP rainfall products. Both satellite-derived rainfall products showed several peaks in rainfall over the S. China Sea in May 1998 (Fig. 2). Both also showed daily rainfall increasing with time. In general, the RELACS system captured these observed features. For example, the model correctly simulated the onset of the SCSM on May 17, with the build up of westerlies over the northern part of the Indian Ocean, and the movement of strong convection and

[3] This dataset is the merged satellite-gauge rainfall estimate. The satellite data includes Special Sensor Microwave/Imager (SSM/I) and infrared (IR) precipitation estimates from geostationary satellites and other low-earth orbit estimates from the Television Infrared Observation Satellite (TIROS) Operational Vertical Sounder (TOVS). The gauge data are assembled and analyzed by the Global Precipitation Climatology Center of Deutscher Wetterdienst and by the Climate Prediction Center of the NOAA. The version of data used here has a spatial resolution of 1 degree x 1 degree and a daily time resolution.

[4] For the sensitivity test, SST was not allowed to vary with time and was kept the same as on the first day of integration (May 18).

[5] The rainfall is based on the Goddard Profiling (GPROF) algorithm for microwave sensing. This rainfall data has higher spatial and time resolutions (0.5 x 0.5, hourly) compared to the GPCP rainfall data. However, the TRMM rainfall data has large gaps due to the nature of the TRMM satellite orbit.

precipitation from the Bay of Bengal to the South China Sea. These features were observed and simulated by MM5. In addition, the model results are in very good agreement with TRMM rainfall during the first 4 days of integration and with GPCP during the last 5 days of integration. The run without PLACE did not capture the observed multiple rainfall peaks.

The water and energy cycles (surface precipitation and its associated latent heat release and surface fluxes) were calculated to assess the role of the atmosphere and the land-surface components responsible for the development of the monsoon for the 1997 and 1998 cases. The results indicated that there were no significant differences in terms of evaporation, rainfall and precipitation between the two cases (left panels in Fig. 2). One of the major differences was that significant moisture was transported into the northern boundary (towards S. China) in 1998 but not in 1997. Another difference was that the eastern Pacific was a moisture source in 1998 but a sink in 1997. There was also a greater contribution from the equatorial region in 1997.

GCE model simulations were also used to provide a better understanding of the precipitation efficiency and surface energy budget associated with convection that developed over the S. China Sea in 1998 [110, 111]. These results indicate that latent heat fluxes (or evaporation) have more of an impact on precipitation in the regional model simulations than in the cloud-resolving model simulation. The results also indicate that the impact of latent heat fluxes on precipitation processes is smaller for the S. China than over the S. China Sea in the MM5 simulations. This is because latent heat fluxes over land have a smaller contribution to precipitation than those from the ocean.

### *3.2 Cloud-Chemistry Interactions*

Organized mesoscale convection provides an effective means for the rapid removal of air from the boundary layer into the overlying free troposphere. The transport within convective-scale updrafts and downdrafts, and the mixing of cloud-free tropospheric air with cloud-processed air can produce a post-storm trace chemical distribution that differs markedly from pre-storm values. The degree of vertical redistribution (or overturning) is indicative of the intensity of the convection, and reflects the transport structure responsible for the mixing. MM5 has been used to investigate the vertical transport and mixing of important trace species by MCSs observed during the NASA Global Tropospheric Experiment (GTE) mission TRansport and Atmospheric Chemistry near the Equator-Atlantic (TRACE-A) experiment (1992).

The TRACE-A experiment measured several different trace gases associated with biomass burning in the convective outflows of MCSs in Brazil. The model produced a fairly accurate surface precipitation field compared with the rain gauge observations. The transport of CO, a trace gas that results from biomass burning, was simulated with the Goddard cloud-chemistry tracer transport module driven by the MM5-generated wind field and a sub-grid cumulus parameterization scheme. The CO field was initialized using mixing ratio profiles taken from field measurements. A detailed description of the TRACE-A MCS and associated tracer transport simulation is described in [119].

Sub-grid transport, which is determined by the cumulus parameterization scheme, accounted for 45% of the total upward tracer transport (Fig. 3). Downward transport was mainly driven by the grid-scale motions, while upward transport was a mixture of both grid- and sub-grid scale motions. MCSs were the principle mechanism by which tracers were transported from the lower troposphere into the upper troposphere. Figure 4 shows a horizontal cross-section of CO mixing ratio after 24 hours of simulation time at 9.5 km and 11.5 km respectively. CO mixing ratios were highest in the two main convective bands.

CO mixing ratios in cloud-processed air were measured at altitudes of 11.5 km and 9.5 km by the NASA DC-8 during TRACE-A flight 6 as given in [81]. To compare the observations with the simulated results, the simulated CO mixing ratios from the regions surrounding the aircraft flight lines were averaged for the two altitudes. The results indicated that tracer transport simulations with MM5-wind fields and either the Grell [40] or Kain-Fritsch [52] cumulus parameterization schemes on average yielded good predictions at the 9.5 km altitude. CO transport from both cumulus schemes produced lower average values than observed at 11.5 km. The simulations are also compared with observations in terms of frequency distributions (Fig. 5). The CO observations from both flight lines have a double peak in the mixing ratio frequency distribution, whereas the simulations show only a single peak. The frequency distributions of simulated CO mixing ratio compare reasonably well with those of the observations at 11.5 km, but not as well as at 9.5 km. The model did not predict enough low CO mixing ratios. Differences in the distributions may be due to the slight difference in the location of the convective system.

### *3.3 Hurricanes*

Hurricanes derive much of their energy from the exchanges of heat and moisture near the ocean surface. However, observations of these exchanges in the inner-core region of hurricanes are rare. This lack of data forces modelers to use boundary layer parameterizations that apply largely to lower wind-speed conditions. It is important to understand how assumptions regarding the character of surface fluxes and vertical mixing within the boundary layer impact simulations of hurricanes so that we may understand the limitations of current assumptions and have some direction for future observational studies.

(a) Sensitivity to Boundary Layer Parameterization

MM5 was used to simulate Hurricane Bob (1991) at high (4-km) resolution [10]. The model was able to reproduce to varying degrees the track and intensity of the hurricane, but results exhibited strong sensitivity to the parameterization of planetary boundary layer (PBL) processes. The PBL parameterizations used in the simulations included the Burk-Thompson, Blackadar, bulk-aerodynamic, and the Medium-Range Forecast (MRF) model PBL schemes. Among the sensitivity tests, simulated minimum sea-level pressures and maximum winds varied by about 16 mb and 15 m $s^{-1}$, respectively, with the Burk-Thompson and bulk-aerodynamic schemes producing the strongest storms and the MRF PBL scheme producing the weakest storm in this case.

Each PBL scheme is different in its formulation of the vertical mixing within the PBL and the surface fluxes, with the exception of the MRF and Blackadar schemes, which share essentially the same surface flux parameterization. Emanuel [33, 34] suggested that the intensity of a hurricane increases as the ratio of the exchange coefficients for enthalpy and momentum, $C_k/C_D$, increases. Vertical motion in the eyewall can be related to vertical motion associated with Ekman pumping at the top of the boundary layer, which scales as $(C_k C_D)^{1/2}$. Analysis of the surface flux schemes under identical conditions indicates that the Blackadar and MRF schemes are associated with a low value of $C_k/C_D$=0.7, while the Burk-Thompson and bulk-aerodynamic schemes have larger values of 1.0 and 1.3, respectively. The low values of $C_k/C_D$, and hence weaker storms, in the Blackadar and MRF cases are due to the relative small value of the exchange coefficient for moisture compared to the Burk-Thompson and bulk-aerodynamic cases. The bulk-aerodynamic case has a large value of $C_k/C_D$, but a small value of $(C_k C_D)^{1/2}$, which explains why it develops a strong vortex despite having the weakest mean eyewall vertical motions of all the cases.

In order to isolate the effects of vertical mixing and surfaces fluxes, additional simulations were conducted in which each of the surface flux schemes was used in conjunction with an identical vertical mixing scheme, and vice versa. Simulations that vary only the surface fluxes indicate that, as long as the surface roughness parameter increases with wind speed, the intensity of the simulated hurricane increases with increasing values of $C_k/C_D$. However, even for identical values of $C_k/C_D$, the simulated intensity varies significantly depending on the wind speed dependence of the surface roughness parameter $z_0$. For simulations that use identical surface fluxes but different vertical mixing schemes, the results show that the Burk-Thompson, Blackadar and bulk-aerodynamic vertical mixing schemes produce storms of comparable intensity and structure, while the MRF vertical mixing scheme produces a weaker storm primarily because it diagnoses an excessively deep boundary layer and causes drying of the lower portion of the PBL.

(b) Storm Structure and Eyewall Buoyancy

The simulation of Hurricane Bob (1991) was redone using a finer grid spacing of 1.3 km [9], a scale similar to many convective cloud models. The vertical motion characteristics of the eyewall was examined in [9] to evaluate the role of buoyancy and "hot towers" [93]. The vertical motions comprising a simulated wavenumber 1 asymmetry in this case are generally associated with small-scale convective updrafts that, at any given time, cover only a small portion of the eyewall area but account for a large proportion of the upward mass flux. For example, the statistical distribution of vertical velocity within the eyewall indicates that updrafts exceeding 2 m $s^{-1}$ generally take the form of either isolated updraft cores or short bands of updraft cores that account for only about 16% of the eyewall area, but 64% of the upward mass flux at mid-levels. These results reaffirm the importance of convective "hot towers" as the primary mechanism for vertical transport of mass in the eyewall.

The fact that the majority of the upward mass flux occurs in small-scale updraft cores suggests that buoyancy plays an important role in the eyewall dynamics that may be masked

by composites or azimuthal averages. The small scale of the updrafts motivates the inclusion of the wavenumber 0 and 1 fields into the reference state used to identify buoyancy, with the resulting perturbations indicating positive buoyancy in the eyewall (Fig. 6). Calculated eyewall trajectories possess strong vertical accelerations up to the melting level, above which water loading significantly dampens the accelerations or reverses them until precipitation falls out. Calculations along the trajectories show sufficient buoyancy to account for the simulated vertical velocities.

A key source for the eyewall buoyancy is the energy gained near the surface by fluxes of moisture and heat from the ocean. Examination of the radial distribution of $\theta_e$ reveals that in the eyewall, tongues of high $\theta_e$ air extend upward from the boundary layer along the inner edge of the eyewall updrafts instead of being collocated with the updrafts, as is seen in convection outside of the eyewall. Trajectory calculations (Fig. 7) suggest that the air in these high $\theta_e$ tongues generally originates from outside of the eyewall, with the highest $\theta_e$ air coming from very near the surface, where it picks up substantial moisture and heat, and penetrating furthest into the eye before rising, allowing the parcels to reach lower pressures and possibly mix with high $\theta_e$ air in the eye boundary layer. Occasionally, high $\theta_e$ air within the eye is drawn into the eyewall updrafts, suggesting an episodic rather than continuous venting of the eye air into the eyewall.

The low-level vertical motions, inflow and outflow, and buoyancy are strongly modulated by a pronounced wavenumber 2 disturbance that creates an elliptically shaped eyewall. The disturbance rotates around the eye at about half the speed of the maximum tangential winds, consistent with theory for vortex Rossby edge waves. Other potential source mechanisms for this wavenumber 2 disturbance include counter-propagating vortex Rossby waves that form in the region of a barotropically unstable mean radial vorticity gradient and large-scale deformation forcing.

(c) An Effective Bogus Vortex Technique

The forecast and simulation of mesoscale systems requires accurate initial conditions for the model. In order to improve model initialization, efforts have been made on mesoscale data assimilation with more advanced techniques, such as adjoint-based four-dimensional variational data assimilation (4DVAR). Further studies have also been made to explore the impact of satellite data (e.g., TRMM) on the forecast of mesoscale systems.

Forecasts of track and intensity changes for mature hurricanes require accurate representation of the hurricane vortex in the model initial conditions. Vortices contained in large-scale analyses from operational centers are often too weak and sometimes misplaced as observations in the vicinity of the hurricane are usually sparse. In order to improve the storm representation, the effectiveness of a 4DVAR technique for creating "bogus" vortices in numerical simulations of hurricanes was evaluated [82]. A series of numerical experiments was conducted to generate initial vortices for hurricanes Georges and Bonnie (1998) in the Atlantic Ocean by assimilating bogus sea-level pressure and wind information into the MM5. Several different strategies were tested to investigate the sensitivity of the initial vortex representation to the type of bogus information. While some of the results in this study

confirmed conclusions made in previous studies [125, 129], some significant differences were found regarding the role of bogus wind data in creating a realistic bogus vortex. In contrast with previous studies in which the bogus wind data had only a marginal impact on creating a realistic hurricane, this study concludes that the wind information is very important because: i) with assimilation of only bogus sea-level pressure information, the response in the wind field is contained largely within the divergent component with strong low-level convergence leading to strong upward motion near the center; and ii) with assimilation of bogus wind data only an expected dominance of the rotational component of the wind field is generated. In this latter case, the minimum pressure is also adjusted significantly, although the adjusted sea-level pressure does not always match the actual hurricane minimum pressure. The generated vortex offers a smooth start to the forecast and leads to a significant improvement in the forecast. Only when both the bogus sea-level pressure and wind information are assimilated together does the model produce a vortex that represents the actual intensity of the hurricane and results in significant improvements to forecasts (Fig. 8) of both hurricane intensity and track. The substantial impact of the bogus wind data in this study suggests a large potential for improvement of model initial conditions and forecasts of hurricane track and intensity by using satellite remotely sensed winds, particularly when pressure information is unavailable or highly uncertain.

### *3.4 Satellite Rainfall Assimilation*

Over the past decade, many studies have shown that the use of satellite-derived rainrates in diabatic or physical initialization can reduce model spin-up and improve short range forecasts ([30, 57, 57, and many others]; see [47, 128] for a brief review). At NASA Goddard, we have examined the impact of assimilating rainfall on the track and intensity forecasts of rapidly intensifying tropical cyclones and hurricanes and have studied the structure and dynamics of tropical cyclones using budget calculations from model simulations.

(a) Assimilation of Rainfall Rates and Vertical Latent Heating Profiles

At Goddard, MM5 has been used to assess the impact of initial conditions and the assimilation of satellite-derived rainfall rates (combined SSM/I-GOES/IR-derived rainfall rates) and vertical latent heating profiles on the simulations of tropical cyclones (Hurricane Florence, 9-10 September 1988, and Hurricane Opal, 3-5 October 1995). The continuous rain assimilation technique [72] was to improve the simulations of a rapidly developing ERICA IOP-4 extra-tropical cyclone. Subsequently, this scheme was modified [53] to simulate the development of Hurricane Florence by performing sensitivity tests with enhanced initial conditions (i.e., initial conditions enhanced with Omega dropwindsondes (ODWs) at 0000 UTC 9 September 1988), rainfall assimilation and cumulus parameterization schemes. Results suggest that rain assimilation (within the first 12 h of 24 h simulations) alone without enhanced initial conditions (i.e., without ODW enhancement) yields a positive impact similar to that given by the enhanced initial conditions (Fig. 9). Both the rain-assimilation and the enhanced-initial-conditions simulations gave a similar intensity for Florence at the end of 24 h, although the location of Florence in the rain-assimilation run lagged behind that in the enhanced-initial-conditions run particularly after 12 h of simulation. The slow movement of Florence in the rain-assimilation run appeared to be related to the asymmetrical location of

the observed rainfall to the south of the center at the initial time. This resulted in a slight southward movement in the first few hours of the rain-assimilation run. Despite the initial position error given by the rain assimilation, rain assimilation without enhanced initial conditions gave intensity and location errors comparable to those using enhanced initial conditions by the end of the simulation. The best simulation, however, was obtained when both the enhanced initial conditions and rain assimilation were combined.

The assimilation scheme was further improved [53] by replacing the specified parabolic heating profiles, which has plagued many tropical rain assimilation studies in the past (e.g., [36, 77]), with the satellite-derived vertical latent heating profiles[6] derived [88] for Hurricane Opal (1995). They performed sensitivity simulations of Hurricane Opal by running the model with and without specified parabolic heating profiles (i.e., by replacing the parabolic heating profile with the satellite-derived vertical heating profiles). The 48-h intensity forecasts from the control and the two sensitivity simulations are shown in Fig. 10 including the observed central pressure from the best track data. Both the rain assimilation simulations (identified by SSM/I assimilation in the blue dashed line and SSM/I - Q1 assimilation in the purple color) yield far superior simulations of Opal compared to the control run (indicated by the green line). However, the SSM/I - Q1 simulation (i.e., the simulation with the satellite-derived vertical latent heating profiles) gives a slightly more intense central pressure, particularly during the latter part of assimilation (i.e., between 1200 UTC on the 3 Oct and 0000 UTC 4 Oct) compared to the run with the specified parabolic heating profiles. Note that neither simulation captured the second rapid pressure fall between 0600 and 1200 UTC on 4 October perhaps due to the coarse, 40 km resolution. Nevertheless, the successful use of satellite-derived vertical latent heating profiles in rainfall assimilation is a major step forward for rain assimilation schemes since no assumptions need to be made with respect to specifying the vertical structure of the latent heating.

(b) Assimilation of Rainfall Rates, Lightening and Integrated Liquid Water

The morphing technique [3, 4] assimilated rainfall rates and integrated liquid water (ILW) into the MM5 to improve a 24 hr forecast of the 13 March 1993 Superstorm. In addition, continuous ground-based measurements of lightning [3] guided the organization, intensification and decay of precipitation in a squall line associated with the 1993 Superstorm as it evolved. Flash rates and convective rainfall rates were scaled at those times when the SSM/I microwave radiometer passed over the storm system. Flash rates at intervening times were then used to provide intervening convective rain rates and locations (Fig. 11). The ILW distribution generated by the MM5 was also morphed during the assimilation using the coefficients of the bi-cubic transformation to keep the ILW distribution consistent with the location of the lightning. Microwave radiometer measurements, improved long-range lightning observations and the morphing technique [13] were used to analyze the 1998 Groundhog's Day Storm. That analysis also led to an improved 6-hour forecast of precipitation and vertical motion fields in the Caribbean. The effect of utilizing morphed ILW on a forecast of the 1993 Superstorm is shown in Fig. 12 which shows the minimum sea level pressure as a function of time. The measured pressure is compared to that derived from the control run

[6] These profiles were mainly simulated by the Goddard Cumulus Ensemble Model.

which only used conventional meteorological data, a run that employed rainfall data uniformly interpolated between SSM/I overpasses, another run that changed the magnitude of the morphed rainfall to be consistent with the evolution of the GOES-IR imagery and finally a run that related flash rates to convective rainfall and stratiform rainfall to IR brightness temperature distributions. The lightning-IR-microwave blended rainfall estimate best described the minimum sea level pressure. It remains to be seen whether other forecasts will work as well.

A major disadvantage of the morphing technique [3, 13] was that it required human identification of the tie points. That precluded the use of the technique for operational applications. An Automatic Morphing Image Registration (AMIR) wavelet transform genetic algorithm [117] was developed to allow complete radar images of hurricanes obtained at 4-hour intervals to be continuously morphed. The correlation coefficient between the morphed and actual radar images at midpoints (2 hours) was 0.88! The AMIR utilized complete images of a hurricane of comparable extent. Unfortunately, swaths of rainfall retrieved by microwave radiometers may only provide partial coverage of a hurricane or frontal system. A technique was recently developed [94] to overcome that limitation. Figure 13 shows rainfall over the North Pacific automatically derived from advected rainfall distributions obtained from NOAA-Advaced Microwave Sounding Unit (AMSU) and SSM/I on the DMSP F-13, 14 and 15 satellites.

(c) Assess the Impact of TRMM Products on Typhoon/Hurricane Simulation

The launch of the TRMM satellite, a joint U.S.-Japan project, in November of 1997 made it possible for quantitative measurements of tropical rainfall to be obtained on a continuous basis over the entire global tropics. TRMM provides a much needed and accurate measurement of rainfall as well as an estimate of the four-dimensional structure of latent (diabatic) heating over the global tropics. The distributions of rainfall and inferred heating can be used to advance our understanding as well as to improve forecasts (simulation) of the global and regional energy and water cycle. In addition, this information can be used for global circulation and climate models for validating and improving their parameterizations.

The impact of TRMM Microwave Imager (TMI)-derived surface rainfall data on the numerical simulation of Super Typhoon Paka (1997) was assessed [84]. A series of mesoscale numerical simulations were conducted for Super Typhoon Paka during its mature stage using the MM5 with initial conditions derived from the Goddard Earth Observing System (GEOS) global analyses both with and without assimilation of the TMI surface rainfall data. The results show that the GEOS analysis with TMI rainfall data leads to a better MM5 simulation of Typhoon Paka in terms of storm intensity, structures and precipitation, because inclusion of rainfall data in the initial and boundary conditions improved the environment of the storm (Fig. 14).

Four-dimensional variation data assimilation, based on optimal control theory, is a unique method because it is based solely on the control objective, the equations governing atmospheric flow, and the instantaneous observations of the flow [62, 78]. 4DVAR rainfall assimilation can improve rainfall prediction as well as the analyses (i.e., [48, 116, 128, 131,

116]). In order to evaluate the impact of TRMM data on mesoscale simulations and forecasts, TMI-derived surface rainfall data was assimilated into the MM5 using an adjoint-based 4DVAR technique [83]. The results demonstrated that assimilation of TMI rainfall data improved the intensity forecast for Hurricane Bonnie (1998). With the assimilation of the TMI rainfall data, the model produced a more realistic eye and outer rain bands. The assymmetric structure of the hurricane was also improved (Fig. 15).

### *3.5 Westerly Wind Bursts and the Diurnal Variation of Precipitation in the Tropics*

The western Pacific warm pool is perhaps the largest diabatic heat source on our planet. The warm pool is the region in the tropics of extraordinarily light winds, deep convection and abundant heavy rainfall (with the most intense latent heat release). The extraordinarily light winds are certainly an important reason for the existence of the global SST maximum there. Convection in warm pool regions appears to possess a strong diurnal variation [i.e., 19, 101] plus modulations on longer time-scales associated with the Madden-Julian Oscillation (MJO) (60, 69, 70, 122]. The light winds are sometimes replaced by strong WWBs along the equator that can alter the structure of the convection and can play a strong role in regulating SST (see [122]). El Nino/Southern Oscillation (ENSO) warm event years can be distinguished from other years largely by the greater frequency and strength of WWBs and the related eastward migration of the warm pool. The generation of WWBs can be also associated with the eastward propagation of the ISO (Intraseasonal Oscillation) from the Indian Ocean.

(a) Westerly Wind Bursts

Several WWBs and SCCs were observed during the Tropical Oceans Global Atmosphere (TOGA) - Coupled Ocean Atmosphere Response Experiment (COARE) ([20; 102] and see [87] for a review). The successful simulation of the MJO may ultimately depend on the successful simulation of the individual life cycles of cloud clusters embedded within SCCs and WWBs.

The MM5 was used to simulate a TOGA COARE WWB event that occurred from 19 to 30 December 1992 [112]. Two nested domains with grid resolutions of 135 and 45 km, respectively, were employed. The model was initialized from NCEP data at 0000 UTC 19 December with time-varying lateral boundary conditions (at 12-h intervals). The exact timing and location of several observed convective systems were not well simulated by the MM5 (as expected). The model results, however, did capture many other observed features, such as an explosive development of SCCs and their associated WWBs that propagated over the equatorial warm pool region (Fig. 16). The large-scale features that are important in this MM5 modeling study consist of a packet of westerly wind, a train of Rossby wave disturbances, and a band of cross-equatorial flow. The westerly wind packet, propagating eastward, was speculated to be associated with an ISO disturbance. In contrast, Rossby wave disturbances, propagating westward, originated from the south central Pacific Ocean. Meanwhile, the cross-equatorial flow, recurving the Northern Hemisphere easterlies into the Southern Hemisphere, was generated by inertial instability resulting from the presence of an easterly jet in the Northern Hemisphere. The convergence of the westerly wind packet, the Rossby wave disturbances, and the cross-equatorial flow apparently led to the intense

development of convection over the TOGA COARE region. Once the intense convection developed, a large-scale cyclonic circulation was produced which propagated eastward toward the western Pacific warm pool over the international dateline. The modeled WWB was closely associated with this large-scale cyclonic circulation which only occurred after the development of convection, as [63] suggested.

(b) The Diurnal and Quasi-two-day Cycle of Precipitation

The diurnal variation of precipitation processes over the tropics is a well-recognized but poorly understood phenomenon. Improved understanding of this diurnal cycle is needed in order to make reliable monthly estimates using twice-daily satellite observations. Different observational platforms (GMS IR, radar reflectivity, upper-air soundings and special mooring data) from TOGA COARE in the tropical western Pacific Ocean were analyzed to study the diurnal variation of precipitation [101]. They found that the diurnal SST cycle is important for afternoon showers during undisturbed periods while diurnal radiative processes are important for nocturnal rainfall. The satellite infrared data and in-situ surface measurements from TOGA COARE indicated that there are two different large-scale flow regimes associated with the diurnal variation of deep convection [19]. Cloud systems that developed during the convectively suppressed phases of the ISO formed, reached maximum size, and dissipated in the afternoon. During the convectively active phases of the ISO, cloud systems generally form in the afternoon and reach a maximum areal extent before dawn. A quasi-2-day cycle in precipitation during TOGA COARE was found [103]. The observation also indicated that inertia-gravity waves may be associated with these 2-day cycles. However, it was suggested in [19] that the quasi-2-day oscillation is mainly a function of the time required by the lower-tropospheric moisture field to recover from the drying caused by deep convection.

MM5 was used to examine the diurnal variation of precipitation processes associated with a TOGA COARE WWB event that occurred from 19 to 30 December 1992 [108]. The model-simulated precipitation showed a maximum at 0600Z (local time) over open ocean as observed even though the model did not allow the diurnal variation of SST. Precipitation over land had a stronger diurnal variation than over ocean. Its maximum, however, was at 0200Z while the observed is at 1800-2000Z. Figure 17 shows the MM5-simulated precipitation field and the average equivalent potential temperature analyzed and composited into four quadrants over the west Pacific warm pool region. The quasi-2-day cycle in precipitation was only simulated over one part of the ocean (Fig. 17). This quadrant also produced the most precipitation (mainly from two cyclones) of the four quadrants. All of the quadrants had a minimum in precipitation at 1400 or 1800 LST. The PBL recovery time can be estimated, approximately, by examining the variation in equivalent potential temperature (Fig. 17). The results suggest that the PBL recovery time ranged from 8 to 16 hours. These values are in good agreement with those suggested by analyzing upper-air soundings.

Upon examining the characteristics of the PBL relative to the diurnal cycle, the model results show that the relative humidity in the PBL has the same phase as the precipitation. However, the diurnal variation of PBL temperature is quite strong and is 180 degrees out phase with the precipitation. This may imply that PBL temperature is only slightly

modified by precipitation processes (i.e., cooling by evaporation of raindrops).

### *3.6 Land Surface Processes*

The surface (land/ocean) and atmosphere form a highly coupled system. Over land, the surface fluxes are coupled to the surface net radiation flux, the vegetation state, and the profiles of temperature and water below the surface and up through the atmospheric planetary boundary layer. These processes at the land-atmosphere interface are influenced in a fundamental way by topographic features and the heterogeneous character of the land surface layer. The fluxes of heat and moisture across the interface vary on spatial scales ranging from meters to thousands of kilometers. Modeling these coupled surface-atmospheric processes is crucial to the understanding and simulation of climate system interactions as well as the boundary layer and convection interactions. For example, both vegetation and soil moisture can affect the evolution of the boundary layer, as well as shallow and even deep convection (e.g, [28, 46, 71, 114]). In fact, recent studies have demonstrated the importance of having the correct soil moisture initialization and soil moisture feedbacks with regard to convective formation (e.g., [67]).

(a) The Florida Sea Breeze

[68] used the vegetation classes provided in MM5 to describe the distribution of vegetation over the Florida peninsula to study the Florida sea breeze. In addition, they developed an alternate soil initialization to the climatology provided with the standard MM5 preprocessor. In particular, they simulated PLACE offline, forced by observations prior to the their case date. Wind, precipitation, temperature and moisture fields from the National Climatic Data Center (NCDC) and from CaPE Portable Automated Mesonet (PAM) observations were ingested into PLACE offline. Given the uncertainty of the soil moisture originally input into PLACE offline, the new values of soil moisture were used as initial conditions for another offline PLACE calculation. This process was repeated until the soil moisture distribution achieved steady state (after 50 iterations). Figure 18 shows the PLACE offline initial soil moisture and temperature fields associated with widespread summertime moist convection during CaPE in the central Florida peninsula. These were obtained at the 30 observational data points where forcing data were available then interpolated to the model nested-grid using a linear interpolation technique. For comparison, Fig. 18 also shows the soil moisture and temperature fields obtained from the (control) MM5 preprocessor after converting from MM5 soil moisture availability to volumetric soil moisture. In comparison to climatology, the PLACE-derived fields contain two regions of relatively dry soil with warm soil temperatures. There are also two maxima in soil moisture, corresponding to relatively cool initial soil temperatures.

Several numerical experiments were conducted to examine the sensitivity of planetary boundary processes (schemes) and initialization with different surface characteristics (Fig. 18). The results clearly indicated that MM5 with PLACE using the TKE (1.5 order turbulent kinetic energy) scheme simulated the best overall results in terms of biases of surface variables, rainfall, and percent and root-mean-square error of cloud cover fraction for this Florida sea-breeze case. An early, isolated convective storm that formed near the east coast,

on the downwind edge of a region of anomalously wet soil, and within the dense cluster of the CaPE mesoscale observation stations, was correctly simulated in the MM5-PLACE run with the TKE scheme. It did not develop in any of the other runs. A factor separation analysis was performed. It showed that a successful simulation required the inclusion of the more sophisticated land surface model, realistic initial soil moisture and temperature, and a high-order closure PBL in order to better represent the effect of joint and synergistic (non-linear) contributions from the land and PBL on the moist convection. Furthermore, the feedback from PLACE (with PLACE initial soil moisture) can have important effects on surface humidity and wind (i.e., the sea-breeze circulation). Surface temperature and humidity also had a pronounced effect on the boundary layer structure, leading to rather important differences in accumulated rainfall between simulations that included PLACE and those that did not. In other related work, [5] also showed that the distribution of initial soil moisture influenced the timing and location of subsequent precipitation. Their work confirmed the findings of [68]. Soil moisture acts as a moisture source for the atmosphere, increases the convective available potential energy, and thus preferentially focuses heavy precipitation over existing wet soil. Differences in soil moisture can also serve to create local mesoscale circulations superimposed upon the sea-breeze circulation.

(b) The Flood Forecasting Project

The goals of the Flood Forecasting Project are: (i) to understand better the physical processes responsible for heavy precipitation and runoff, and (ii) to assess the ability of the MM5 coupled with the PLACE land surface model to predict extreme flood events. MM5-PLACE has been used to investigate extreme precipitation events for which the land surface may have a significant impact on the evolution of the system. For example, thunderstorms produced heavy rainfall and historic flash flooding in east-central Missouri on 6-7 May 2000, with up to 13 inches of rain in some areas [38, 73]. Mesoscale analysis suggests that a strong low-level jet (LLJ) contributed to the high rainfall rates of this system [73]. The Goddard modeling group is investigating the role of the land surface on LLJ development and subsequent heavy precipitation for this event [6]. Recent results indicate that for heavy events such as the 6-7 May 2000 Missouri flood, a fine, horizontal grid resolution is needed to capture strong, localized storms. In addition, high-resolution initial conditions are required to accurately reproduce LLJ evolution and the location of heavy rainfall.

To test the sensitivity of the extreme precipitation in the Missouri flood to grid resolution and initial conditions, four different simulations were performed using MM5-PLACE. Two simulations utilized default 2.5-degree NCEP global reanalysis for initialization, while two different simulations used 40-km Eta reanalysis initial conditions. Hereafter, "NCEP" and "Eta" refer to MM5-PLACE mesoscale simulations initialized by NCEP global reanalysis and Eta reanalysis, respectively. Horizontal boundaries were updated every 12 hours in the NCEP runs and every 3 hours in the Eta runs. Within each set of runs, one simulation had a 5-km inner grid spacing (with a 15-km outer grid) and the other simulation had a 1.7-km inner grid spacing (with 15-km and 5-km outer grids). The 15-km grid used the Kain-Fritsch cumulus parameterization while the other grids used the Goddard explicit cloud microphysical scheme [106, 109]. Initial soil moisture and soil temperature from MM5-supplied climatological data were used.

Grid resolution had a strong impact on the localized rainfall intensity. Figure 19 shows the 24-hour-accumulated rainfall for the four simulations with different grid resolutions and different initializations. Finer grid resolution produced heavier rainfall in both the Eta runs (Figures 19 a and c) and the NCEP runs (Figs. 19 b and d), but the general location of the heaviest rainfall remained relatively unchanged. In the Eta runs, the 1.7-km simulation produced 32% more rain at the location of the highest observed rainfall than the 5-km simulation (Fig. 20).

High-resolution initialization primarily modified the location of the heavy rainfall (Fig. 20). MM5-PLACE simulations with high-resolution Eta initialization indicated widespread precipitation over central Missouri, while the cases with NCEP global initialization concentrated the heavy precipitation in eastern Missouri. The 1.7-km Eta run agreed most closely with the observed rainfall distribution based on radar estimates (not shown). Although none of the simulations reproduced rainfall amounts near the observed peak of 344 mm, Eta runs exhibited much heavier precipitation at the location of the heaviest observed rainfall (Fig. 20). Thus, both fine-grid resolution and high-resolution initial conditions are required for accurate simulation of the 6-7 May 2000 Missouri flood.

### *3.7 Influence of Soil Heterogeneity on Land Surface Fluxes in the southwest GCIP area*

A study focusing on the influence of soil heterogeneity on the partitioning of surface energy fluxes in the southwest portion of the GEWEX Continental-Scale International Project (GCIP) was completed [50] using MM5-PLACE. The study consisted of four 12-hr simulations, from 6 AM - 6 PM, on June 10, 1992, corresponding to the *Washita '92 Hydrology Experiment* [49]. A 70 x 70 grid domain with a 15-km grid size was employed that was centered over Oklahoma and the surrounding states. The four simulations were initialized with identical NCAR initializations and vegetation distributions based on satellite data. However, soil moisture and soil texture (i.e. soil hydraulic properties of $K_{sat}$, porosity, field capacity, wilting point) were assigned as either heterogeneous or uniform, as indicated in Table 2. Heterogeneous soil texture means that the texture of each grid box was assigned according to the STASGO database [76]. Uniform texture means that the entire domain was set equal to the dominant texture of the region, or silty loam. Uniform or homogeneous soil moisture means that the initial soil moisture profile on June 10 for each grid box was computed by off-line PLACE simulations from January 1991 through June 9, 1992, driven by a combination of available meteorological data and assimilated data. For the uniform soil moisture case, the initial soil moisture profile across the domain was assumed equal to the average volumetric soil moisture of the June 10 heterogeneous field. Thus, the domain-averaged soil moisture of all four cases was identical, although their vertical and horizontal spatial distributions differed.

Once the four coupled-simulations were completed, their surface fluxes were compared. The results are provided in Table 2 in terms of 12-hr. domain averaged fluxes of net radiation, sensible heat, and evaporative fraction (latent heat/(net radiation - ground heat). Also shown in Figure 21, as a typical example, is the impact of soil moisture heterogeneity on

the resulting spatial variability in land surface latent heat flux after 6 hours of simulation.

The results indicate that soil heterogeneity affects the spatial distribution and partitioning of water and energy fluxes at the mesoscale. At least for the June 10 test case, the influence of soil moisture heterogeneity was greater than the influence of soil texture heterogeneity. Spatial averaging resulted in an over-prediction of latent heat flux from 6-10%, and an underestimation of sensible heat flux from 10-20%. On-going studies also indicate corresponding impacts on the surface meteorological fields.

| | Case I | Case II | Case III | Case IV |
|---|---|---|---|---|
| | Heter. soil moist. Heter. texture | Uniform soil moist. Heter. texture | Heter. soil moisture Uniform texture | Uniform soil moist. Uniform texture |
| **Net Radiation** | **313 (105)** | **314 (106)** | **311 (104)** | **311 (105)** |
| **Latent Heat** | **191 (67)** | **206 (61)** | **206 (73)** | **216 (67)** |
| **Sensible Heat** | **107 (68)** | **94 (49)** | **92 (59)** | **83 (40)** |
| **Ground Heat** | **8 (6)** | **7 (6)** | **7 (5)** | **7 (6)** |
| **Evaporative Fraction** | **0.64 (0.13)** | **0.68 (0.06)** | **0.69 (0.11)** | **0.72 (0.04)** |

**Table 2** Comparison of domain averaged fluxes [Mean and (Stand. Dev.) in $W/m^2$] after 12 hours of simulation on June 10, 1992 using MM5-PLACE for the GCIP Southwest Study Area

### *3.8 Narrow Cold Frontal Rainbands*

Narrow cold frontal rainbands (NCFRs) can produce very intense rainfall rates (i.e., Hobbs 1978). The cloud updrafts associated with NCFRs are quite strong for relatively shallow radar echo tops (4-5 km AGL) (i.e., [12, 45,51, 79]). Convective cells within a NCFR are often severe (e.g., heavy rain, strong surface winds, etc.) in spite of their shallow nature. In addition, NCFRs exhibit graviety current-like structures and motion [11, 12, 80, 56]. A brief review on structures and processes associated with NCFBs was given in [14, 51].

The MM5 was used [14] to conduct a series of real-data numerical experiments to study the Dec 28, 1988 NCFR case documented by [56]. This storm was characterized by severe line convection along the leading edge of a strong surface cold front propagating over the Appalachian Mountains (Fig. 22). This NCFR caused considerable damage throughout a large region and was not predicted by official weather forecasts issued that day. In order to resolve the fine structure of the front, the MM5 model was configured to have the grid domains triply nested with the inner-most grid domain covering parts of Virginia, West Virginia and Maryland. The grid resolutions for these three domains were 45, 15 and 5 km, respectively. The MM5-simulated precipitation pattern showed a dual band structure (Fig. 22b). This pattern is in good agreement with satellite and radar observations (Fig. 22a and Fig. 2 in [56]), both in the temporal and spatial dimensions of the rain band. However, MM5 was not able to predict the observed precipitation intensity that occurred in a narrow region (5-10 km). The MM5 results also showed that the simulated low-level gravity current (low-level jet ahead of the NCFR) was not generated by the evaporation or melting of hydrometeors as suggested [56]. PBL frictional processes, which can produce cross-frontal

low-level wind shear, played an important role in producing the simulated gravity current. It was also suggested that the observed intensity of the NCFR was closely related to frictionally induced PBL processes. However, the simple microphysics and grid resolution may limit the model interpretation regarding the role of evaporative cooling in maintaining the gravity current.

A NOAA P-3 instrumented aircraft observed an intense, fast-moving NCFR as it approached the Pacific Northwest coast on 19 February 2001 during the Pacific Coastal Jets Experiment. The NCFR produced hail along the California coast when it made landfall. An outstanding feature of the NCFR was the breaks (gaps) observed along the rainband by Dopplar Radar. The MM5 was used to simulate this NCFR. The numerical simulations were conducted using nested-grids with resolutions of 36km, 12km, 4km and 1.3km [51]. The high-resolution domain was able to reproduce the main structural features of the observed NCFR (Fig. 23). The breaks (gaps) along the rainband were well represented. Many other observed features (i.e., location of the band, shallow radar echo top and maximum low-level reflectivity of ~45 dBZ) were captured by the model. Observations also confirmed that the character of the modeled updrafts depended on the balance of vorticity at the leading edge. The balance between cold-pool-induced and pre-frontal ambient shears (horizontal shear instability) along the leading edge of the cloud was found to be responsible for the gaps.

### *3.9 Heavy Precipitation over Taiwan*

Flash floods occur frequently in Taiwan during the Mei-Yu season (mid-May to mid June, see [18, 59, 118, 59]) and in summer. During Mei-Yu season, precipitation systems associated with the Mei-Yu front can produce a large amount of rainfall [59] or heavy rainfall events can occur over mountain slopes as a result of the interaction between topography and the prevailing wind. Mid-July through August is one of the main rainy periods over Taiwan during the southwesterly monsoon. According to [16], the two main types of disturbances that pass over Taiwan to produce summer rainfall are typhoons and convective systems embedded in the southwesterly monsoonal flow [65, 91].

The MM5 was used to study two major precipitation events that occurred over the western side of Taiwan's complex terrain from August 10 to 13, 1994 [113]. During the first event, August 10 to 11, most of the rainfall fell over sloped areas in the morning. The heaviest daily rainfall totals were over southwestern and central Taiwan (Fig. 24 a and b). However, not much rainfall occurred over northern Taiwan. During the second event, August 12 and 13, most of the higher rainfall amounts were found over the coastal area in southwestern Taiwan. Notably, rainfall rates of more than 300 mm per day fell over the coastal area in southwestern Taiwan on August 12 and during the night of August 13 (Fig. 24 c and d). In general, the location of the precipitation was well simulated by the model (Fig. 25). But, the exact timing and the duration of the heavy precipitation were not well simulated in either case. The model results suggested that the diurnal variation of land surface temperature was responsible for the timing (morning) and location of the precipitation for the first event. The interaction between the oncoming prevailing wind and the offshore flow was

important for developing the precipitation that occurred in the late evening of August 12[7]. The model results also suggested that topographic lifting played an important role (though only secondary) in the August 10 event but not in the August 12 event.

Sensitivity tests indicated that cloud physics, land surface and radiation processes generally do not change the horizontal location or distribution of heavy precipitation. The Goddard 3-class ice scheme did however produce more rainfall than the 2-class scheme (Table 3). The Goddard multiple, broad-band radiative transfer model reduced precipitation compared to a single, broad-band (emissivity) radiation model. The Goddard land-soil-vegetation surface model also reduced the amount of rainfall compared to a simple surface model in which the surface temperature was computed from a surface energy budget following the "force-restore" method. However, model runs that included all of the Goddard physical processes enhanced the amount of precipitation significantly in both cases. The results from these runs were also in better agreement with observations. The modeling results also indicated that terrain played a major role in determining the exact location of the precipitation events. The terrain also played a major role in determining the intensity of the precipitation. [113] also found that no matter how sophisticated the model physics were, the synoptic initialization dominates the first 24 hours of the simulation. The sensitivity of the model to the physics becomes more apparent between 24 and 48 hours of simulation time.

The performance of the Goddard physical processes was only based on comparisons against the simplest physics available in the MM5. It is planned to compare the Goddard physical schemes against more sophisticated schemes for various heavy precipitation cases that have occurred in different geographic locations in the future.

| Run | Land Processes | Microphysics | Radiation | Terrain | Case | August 10 - 11 or August 12- 13 |
|---|---|---|---|---|---|---|
| 1 | Blackadar | 2-Ice | Dudhia | Yes | 1 | 41.44/18.24 |
| 2 | Blackadar | 3-Ice Goddard | Dudhia | Yes | 1 | 47.19/16.00 |
| 3 | Blackadar | 2-Ice | Goddard | Yes | 1 | 30.58/13.32 |
| 4 | PLACE | 2-Ice | Goddard | Yes | 1 | 39.93/11.80 |
| 5 | PLACE | 3-Ice Goddard | Goddard | Yes | 1 | 62.36/48.18 |
| 6 | Blackadar | 2-Ice | Dudhia | No | 1 | 33.25/5.99 |
| | | | | | | 44.80/90.97* |
| 7 | Blackadar | 2-Ice | Dudhia | Yes | 2 | 7.69/13.92 |
| 8 | Blackadar | 3-Ice Goddard | Dudhia | Yes | 2 | 28.31/38.55 |
| 9 | PLACE | 3-Ice Goddard | Goddard | Yes | 2 | 33.79/46.00 |
| 10 | Blackadar | 2-Ice | Dudhia | No | 2 | 21.45/20.53 |
| | | | | | | 59.40/31.68* |

**Table 3** Summary of the numerical experiments. The last column shows daily accumulated rainfall. For Case 1, simulated rainfall for August 10 and 11 are shown. For Case 2, August 12 and 13 are shown. * is the observed rainfall obtained from by 243 hourly rainfall stations and 22 conventional stations.

[7] In a separate study [17], westerly flow was found to decelerate along the coast and lowland areas and induce upward motion and thereafter enhance rainfall there.

### *3.10 Real Time Forecasts for CRYSTAL-FACE*

The Goddard version of MM5 can use NCEP MRF, NCEP Eta, ECMWF or Goddard GEOS global datasets for initialization. We developed a mid-Atlantic regional real-time (assimilation) modeling system. The system has been run on a SGI Power Challenge (8 processors) at the Goddard Mesoscale Atmospheric Processes Branch and a SGI Origin 3000 (1,024-processor) at the NASA Advanced Supercomputing Division (NAS) at the NASA Ames Research Center using multiple, two-way interactive, nested grids (45-, 15- and 5-km resolutions) for 24-36 h forecasting. A postprocessor was developed to show surface precipitation, temperature (a good indicator for snow/rain), wind and pressure. In addition, horizontal and vertical cross-sections of many parameters (i.e., PV, total precipitable water, equivalent potential temperature, velocities, thickness, upper level jets) are displayed on a web site.

Thirty-six-hour forecasts for the Florida region were produced daily during the NASA Earth Science Mission Cirrus Regional Study of Tropical Anvils and Layers - Florida Area Cirrus Experiment CRYSTAL-FACE during July of 2002. The simulations had two-way interactive, nested domains with an inner domain of 85 x 82 grid points at 5-km resolution. The initial and boundary conditions took advantage of NCEP high-resolution (32km) Eta model results. The Kain-Fritsch cumulus parameterization scheme was used for the outer domain (15-km resolution), and the Goddard microphysics and Blackadar PBL were used for both domains.

The key science objectives of CRYSTAL-FACE were to improve the understanding and models of i) cirrus anvil properties in relationship to the properties and strength of deep convection, ii) factors that control the lifetime and area coverage of cirrus anvils and tropical cirrus layers, iii) the effects of deep convection and cirrus on tropical upper tropospheric humidity, and iv) the processes that control lower stratospheric humidity. An essential element was to quantify, using models and a variety of observations, the transport of air from the lower to upper troposphere (cumulus mass flux). The MM5 forecasts were made to directly support near-real-time flight planning for the 6 aircraft involved in the experiment. Forecast simulations were initialized with the 00 UTC Eta fields and full graphical output was available to the forecast team via the web by 11 UTC, in time to support daily flight planning. Take-offs were typically at 15-16 UTC following a 3-hour upload and preparation time. Comparable quasi-operational simulations were also made by other groups using ARPS and RAMS in similar nested-grid configurations also initialized with Eta fields. Each day, a synopsis and comparative discussion of the model results was generated by a member of the forecast team. While each model had its good and bad days, the results were useful to the flight planning team and significantly influenced the in-flight mission direction where understanding and anticipation of the progression of events was critically important in timely re-location of aircraft patterns in a volatile and rapidly evolving environment.

The real-time MM5 forecasting system performed fairly well on many of the experiment days when compared with NEXRAD radar. Figure 26 shows an example (pre-experiment) with a front located across the Florida Panhandle and a short wave that developed ahead of the front. There was SW flow over southern Florida. Isolated convection occurred and anvilswere transported to SE on the backside of the upper trough. Overall, the

model produced a good forecast in terms of the location, onset, and development of the convection that developed primarily in response to the synoptic forcing. Another example is shown in Fig. 27 where convective systems developed along the eastern coast of southern Florida under a prevailing weak SW lower tropospheric flow that interacted with the local land-sea breeze circulation. The anvils flowed slowly toward the SW. Again, the real time forecast well captured the location and onset of the storms, the anvils of which were extensively sampled by aircraft.

The forecast simulations are being re-run for key experiment days using Eta analysis for the boundary conditions. These simulations are then used to drive a chemical transport model to study mass transport and thereby validate the convective mass flux via comparison to tracer species measurements, and also to drive a highly-detailed two-dimensional explicit microphysics (bin model) cirrus cloud model to study anvil processes.

## 4. FUTURE STUDY

This paper described the improvements to and applications of a regional scale model (MM5) at NASA GSFC. Many promising results were obtained that improved the understanding of the physical processes associated with various types of clouds, cloud systems, hurricanes and frontal rainbands that developed in different geographic locations. Although the model has been tested against rainfall, radar observations and some satellite measurements, still more observations are needed to improve and validate the model-simulated cloud structures. Despite the use of sophisticated microphysical, land surface and radiation schemes, the model is by no means perfect. Figure 28 shows a schematic diagram of how MM5 and the GCE model[8] are used to study precipitation processes and the hydrological cycle. Observational data obtained from well-planned field campaigns can provide data, especially much needed cloud microphysical properties, for model improvement and validation. The models can provide a continuous description of atmospheric fields in space and time for the development of satellite retrieval algorithms. The satellite-derived data, especially over tropical oceans, can provide additional data coverage, improving model initial conditions. An international program, the GEWEX (Global Energy and Water Cycle Experiment) Cloud System Study (GCSS), was initiated to improve the representation of cloud processes in climate and Numerical Weather Prediction (NWP) models. The GCSS Science Team [37] recommended that improved cloud-resolving models (CRMs and MM5) should be used as a test bed to develop and evaluate cloud parameterization in large-scale models. In addition, the NASA ESE advocates the use of these models as process models to understand the physical processes associated with clouds and their roles in the regional water and energy cycles.

The following lists the specific model improvements and scientific research we plan to do in the next few years:

- Implement a TOGA COARE flux algorithm [35] into MM5. Sensitivity tests showed that the TOGA COARE flux algorithm produced better agreement with observations

[8] Typically the GCE model is used to thoroughly test new model improvements against observations before implementing the new schemes into the MM5.

compared to the Blackadar scheme, which is similar to the scheme used in MM5, for two tropical squall line simulations, one over the West Pacific and one over the East Atlantic [120];

- Implement an ocean mixed layer model (OML, [2, 55]) and an ocean model (Princeton Ocean Model, POM, [75]) to improve the understanding of the impact of precipitation and changes in the planetary boundary layer upon SST variation. The coupling of MM5 with ocean model can also improve our understanding of the impact of hurricanes on ocean process;

- Implement a 1+1D rainfall assimilation technique [48] into the MM5 to improve regional-scale climate model simulations and consequently regional-scale hydrological cycles associated with high-impact tropical and subtropical weather events (i.e., MCSs, cyclones and fronts) at very high resolution (i.e., a few km). The 1+1D technique uses a variational framework to assimilate 6-hourly averaged precipitation and water vapor;

- Apply an adjoint-based 4DVAR to assimilate satellite-derived rain rates and diabatic and moistening profiles to improve weather forecasts. The impact of TRMM and GPM data on mesoscale simulations and forecasts will be evaluated;

- Implement a cloud-chemistry-aerosol module to assess the impact of aerosols on precipitation processes. In addition, the vertical transport and mixing of important chemical species by clouds and/or MCSs simulated by mesoscale models on a continental scale will be quantified and compared with those from observations and simulated by global models.

- Implement Goddard microphysical, shortwave and longwave radiation (including cloud optical properties), land surface, and rainfall and bogus vortex assimilation schemes and diagnostics into the new WRF. The WRF is a next-generation mesoscale forecast model and assimilation system that will be a candidate to replace existing forecast models (i.e., MM5, NCEP/ETA and FSL/RUC). We will perform benchmark cases for both idealized cases and real case studies, which have been simulated using either the GCE or MM5. Ultimately, the WRF will replace the Goddard MM5 for research and operational forecasts;

- Incorporate more realistic urban land surfaces into coupled atmosphere-land model simulations [90]. It is planned to utilize emerging knowledge of urban land surface properties (e.g. roughness length, leaf area index, albedo and skin temperature) from remote sensing platforms (i.e., Terra and Aqua) to strengthen the model's boundary and initial conditions and to improve the urban representations in the land surface scheme;

- Investigate the sensitivity of the strength and evolution of simulated MCSs and hurricanes to vertical and horizontal grid resolution. The impact of grid resolution on rainfall assimilation will also be examined. This research could help to improve

quantitative precipitation forecasts (QPF) and further the study of hurricanes and MCSs from numerical weather prediction models;

- Complement large-scale field experiments that would otherwise be sub-critical in terms of cloud-scale and mesoscale measurements needed to derive physically based parameterizations for NWP models and climate models;

- Provide consistent and comprehensive four dimensional cloud datasets from the improved model to TRMM and GPM rainfall retrieval algorithm developers as well as help in the design of space-based and earth-based remote sensing and in the interpretation of the datasets;

- Investigate the role of the land surface on the development of extreme precipitation events, especially the effects of topography, soil moisture feedback, and land-use variations on intensity and location of heavy rainfall; and

- Investigate the Improve the understanding of the role of land surface processes within regional land atmosphere exchanges and atmospheric circulation.

## 5. ACKNOWLEDGEMENT

The regional-scale modeling group is supported by the NASA Headquarters physical climate program, the NASA TRMM, and the interdisciplinary program of NASA Earth Science Enterprise (ESE). Co-author, Dr. R. Kakar, is the TRMM Program Scientist and the funding manager for the physical climate program. Acknowledgment is also made to NASA Goddard Space Flight Center for computer time used in the research.

## 6. REFERENCES


1. Anthes, R. A., 1990: Recent applications of the Penn State/NCAR mesoscale model to synoptic, mesoscale and climate studies. *Bull. Amer. Meteor. Soc.*, **71**, 1610-1629.

2. Adamec, D., R. L. Elsberry, R. W. Garwood and R. L. Haney, 1981: An embedded mixed-layer ocean circulation model. *Dyn. Atmos. Oceans*, 6(2), 69-96.

3. Alexander, G. D., J. A. Weinman, J. L. Schols, 1998: The Use of Digital Warping of Microwave Integrated Water Vapor Imagery to improve Forecasts of Marine Extratropical Cyclones. *Mon. Wea. Rev.*, **126**, 1469-1496.

4. Alexander, G. D., J. A. Weinman, V. M. Karyampudi, W. S. Olson and A. C. L. Lee, 1999: The effect of assimilating rain rates derived from satellites and lightning on forecasts of the 1993 Superstorm. *Mon. Wea. Rev.*, **127**, 1433-1457.

5. Baker, R. D., B. H. Lynn, A. Boone, W.-K. Tao, and J. Simpson, 2001: The influence of soil moisture, coastline curvature, and land-breeze circulations on sea-breeze initiated precipitation. *J. Hydrometeor.*, **2**, 193-211.

6. Baker, R. D, Y. Wang, W.-K. Tao, and P. Wetzel, 2002: Soil moisture, land-atmosphere interaction, and the 6-7 May 2000 Missouri flash flood event. *21st Conference on Severe Local Storms*, San Antonio, TX, *Amer. Meteor. Soc.*, 679-681.

7. Betts, A. K., and M. J. Miller, 1986: A new convective adjustment scheme. Part II: Single column tests using GATE wave, BOMEX, ATEX and arctic air-mass data sets. *Quart. J. Roy. Met. Soc.*, **112**, 677-691.

8. Boone, A. and P. J. Wetzel, 1999: A simple scheme for modeling sub-grid soil texture variability for use in an atmospheric climate model. *J. Met. Soc. Japan*, **77**, 317-333.

9. Braun, S. A., 2002: A cloud-resolving simulation of Hurricane Bob (1991): Storm structure and eyewall buoyancy. *Mon. Wea. Rev.*, **130**, 1573-1592.

10. Braun, S. A., and W.-K. Tao, 2000: Sensitivity of high-resolution simulations of Hurricane Bob (1991): To planetary boundary layer parameterizations. *Mon. Wea. Rev.*, **128**, 3491-3961.

11. Braun, S. A., R. A. Houze, Jr., B. F. Smull, 1997: Airborne dual-Doppler observations of an intense frontal system approaching the Pacific Northeast coast. *Mon. Wea. Rev.*, **125**, 3131-3156.

12. Carbone, R. E., 1982: Severe frontal rainband. Part I: Stormwide dynamic structure. *J. Atmos. Sci.*, **39**, 258-279.

13. Chang, D.-E., J. A. Weinman, C. A. Morales, W. S. Olson, 2001: The Effect of Spaceborne Microwave and Ground Based Continuous Lightning Measurements on Forecasts of the 1998 Ground-hog Day Storm. *Mon. Wea. Rev.*, **129**, 1809-1833.

14. Chen, C., C. Bishop, G. Lai, and W.-K. Tao, 1997: Numerical simulations of an observed narrow cold frontal rainband,. *Mon. Wea. Rev.*, 125, 1027-1045.

15. Chen, C., W.-K. Tao, P.-L. Lin, G. S. Lai, S.-F. Tseng and T.-C. Chen Wang, 1998: The interaction of the low-level jet during the development of mesoscale convective systems in a Mei-Yu front. *Mon. Wea. Rev.*, 126, 349-371.

16. Chen, C.-S., and Y.-L. Chen, 2002: The precipitation characteristics of Taiwan. *Mon. Wea. Rev.*, (Accepted).

17. Chen, C. S., W.-C. Chen, and W.-K. Tao, 2002: A study of heavy summer rainfall over southwestern Taiwan. *J. Meteor. Soc. Japan,* (submitted).

18. Chen, G. T.-J., 1993: Mesoscale features onserved in the Taiwan Mei-Yu season. *J. Meteor. Soc. Japan*, **70**, 497-516.

19. Chen, S., R. A. Houze, Jr., 1997: Diurnal variation and life-cycle of deep convective systems over the tropical Pacific warm pool. *Q. J. R. Meteorol. Soc.*, **123**, 357-388.

20. Chen, S., R. A. Houze, Jr and B. E. Mapes, 1996: Multiscale variability of deep convection in relation to large-scale circulation in TOGA-COARE. *J. Atmos. Sci.*, **53**, 1380-1409.

21. Chen, Y.-L., 1993: Some synoptic-scale aspects of the surface fronts over southern China during TAMEX. *Mon. Wea. Rev.*, **121**, 50-64.

22. Chou, M.-D., 1984: Broadband water vapor transmission functions for atmospheric IR flux computation. *J. Atmos. Sci.*, **41**, 1775-1778.

23. Chou, M.-D., 1986: Atmospheric solar heating rate in the water vapor bands. *J. Climate Appl. Meteor.*, **25**, 1532-1542.

24. Chou, M.-D., 1990: Parameterization for the absorption of solar radiation by O2 and CO2 with application to climate studies. *J. Climate*, **3**, 209-217.

25. Chou, M.-D., 1992: A solar radiation model for use in climate studies. *J. Atmos. Sci.*, **49**, 762-772.

26. Chou, M.-D., and L. Kouvaris, 1991: Calculations of transmission functions in the IR CO2 and O3 Bands. *J. Geophys. Res.*, **96**, 9003-9012.

27. Chou, M.-D., and M. J. Suarez, 1994: An efficient thermal infrared radiation

parameterization for use in general circulation models. *NASA Tech. Memo.*, 104606, 3, 85 pp.

28. Clark, C., A. Paymond, and P. W. Arritt, 1995: Numerical Simulations of the Effect of Soil Moisture and Vegetation Cover on the Development of Deep Convection. *J. Applied Meteo.*, **34**, 2029–2045.

29. Cox, S. K., and K. T. Griffith, 1979: Estimates of radiative divergence during Phase III of the GARP Atlantic Tropical Experiment: Part II. Analysis of Phase III results. *J. Atmos. Sci.*, **36**, 586-601

30. Donner, L. J., 1988: An initialization for cumulus convection in numerical weather prediction models. *Mon. Wea. Rev.*, **116**, 377-385.

31. Dudhia, J., 1989: Numuerical study of convection observed during winter monsoon experiment using a mesoscale two-dimensional model. *J. Atmos. Sci.*, **46**, 3077-3107.

32. Dudhia, J., 1993: A nonhydrostatic version of the Penn State-NCAR mesoscale model: Validation tests and simulation of an Atlantic cyclone and cold front. *Mon. Wea. Rev.*, **121**, 1493-1513.

33. Emanuel, K. A., 1995: The behavior of a simple hurricane model using a convective scheme based on subcloud-layer entropy equilibrium. *J. Atmos. Sci.*, **52**, 3960-3968.

34. Emanuel, K. A., 1995: Sensitivity of tropical cyclones to surface exchange coefficients and a revised steady-state model incorporating eye dynamics. *J. Atmos. Sci.*, **52**, 3969-3976.

35. Fairall, C., E. F. Bradley, D. P. Rogers, J. B. Edson, and G. S. Young, 1996: Bulk parameterization of air-sea fluxes for TOGA COARE. *J. Geophy. Res.*, **101**, 3747-3764.

36. Fiorino, M., and T. T. Warner, 1981: Incorporating surface winds and rainfall rates into the initialization of a mesoscale hurricane model. *Mon. Wea. Rev.*, **109**, 1914-1929.

37. GEWEX Cloud System Science Team, 1993: The GEWEX Cloud System Study (GCSS). *Bull. Amer. Meteor. Soc.*, **74**, 387-399.

38. Glass, F. H., 2001: The extreme east-central Missouri flash flood of 6-7 May 2000. *Symposium on Precipitation Extremes: Prediction, Impacts, and Responses*, Albuquerque, NM, *Amer. Meteor. Soc.*, 174-179.

39. Gray, W. M., and R. W. Jacobsen, 1977: Diurnal variation of deep cumulus convection. *Mon. Wea. Rev.*, **105**, 1171-1188.

40. Grell, G. A., 1993: Prognostic evaluation of assumptions used by cumulus parameterizations. *Mon. Wea. Rev.*, **121**, 764-787.

41. Grell, G. A., J. Dudhia and D. R. Stauffer, 1994: A description of the Fifth-Generation Penn State/NCAR Mesoscale Model (MM5). NCAR Technical Note, NCAR/TN-398+IA, pp107.

42. Henderson-Sellers, Z.-L. Yang and R. E. Dickinson, 1993: The project for intercomparison of land surface parameterization schemes. *Bull. Amer. Meteor. Soc.*, **74**, 1335-1349.

43. Henderson-Sellers, A. J. Polcher, P. K. Love, K. McGuffie, and T. H. Chen, 1995: The project for intercomparison of land surface parameterization schemes (PILPS): Phases 2 and 3. *Bull. Amer. Meteor. Soc.*, **76**, 489-503.

44. Hobbs, P. V., 1978: Organization and structure of clouds and precipitation on the mesoscale and microscale in cyclonic storms. *Rev. Geophys. Space Phys.*, **16**, 741-755.

45. Hobbs, P. V., and P. O. G. Persson, 1982: The mesoscale and microscale structure of clouds and precipitation in midlatitude cyclones. Part V: The substructure of narrow cold frontal rainbands. *J. Atmos. Sci.*, **39**, 280-295.

46. Hong, X., M. J. Leach, and S. Raman, 1995: A Sensitivity Study of Convective Cloud Formation by Vegetation Forcing with Different Atmospheric Conditions. *J. Applied Meteo.*, **34**, 2008–2028.

47. Hou, A. Y., D. V. Ledvina, A. M. da Silva, S.-Q. Zhang, J. Joiner, R. M. Atlas, G. J. Huffman, and C. D. Kummerow, 2000: Assimilation of SSM/I-derived surface rainfall and total precipitable water for improving the GEOS analysis for climate studies. *Mon. Wea. Rev.*, **128**, 509-537.

48. Hou, A. Y., S.-Q. Zhang, A. M. da Silva, and W. S. Olson, 2000: Improving assimilated global datasets using TMI rainfall and columnar moisture observations. *J. Clim.*, **13**, 4180-4195.

49. Jackson, T. J., and F. R. Schiebe, Editors, 1993: Hydrology Data Report WASHITA '92., USDA Agricultural Research Service, Durant, OK, 190 pp.

50. Jin H., and M. Jasinski, 2000: A numerical study on the influence of land surface heterogeneity on land-atmosphere interactions in the GEWEX GCIP region. *Third International GEWEX Conference*, Beijing, June 2000.

51. Jorgensen, D. P., Z.-X. Pu, O. Persson and W.-K. Tao, 2002: The structure of a Pacific narrow cold frontal rainband. *Mon. Wea. Rev.*, (submitted).

52. Kain, J. S., and J. M. Fritsch, 1990: A one-dimensional entraining /detraining plume

model and its application in convective parameterization. *J. Atmos. Sci.*, **47**, 2784-2802.

53. Karyampudi, V. M., G. Lai, and J. Manobianco, 1998: Impact of initial conditions, assimilation of rainfall rates and cumulus parameterization on simulations of Hurricane Florence (1988). *Mon. Wea. Rev.*, **126**, 3077-3101.

54. King, M. D., L. F. Radke, and P. V. Hobbs, 1990: Determination of the spectral absorption of solar radiation by marine strato-cumulus clouds from airborne measurements within clouds. *J. Atmos. Sci.*, **47**, 894-907.

55. Koch, S. E., and P. J. Kocin, 1991: Frontal scale contraction processes leading to the formation of an intense narrow rainband. *Meteorol. Atmos. Phys.*, **46**, 123-154.

56. Kraus, E. B., and J. S. Turner, 1967: A one-dimensional model of the seasonal thermocline, II, The general theory and its consequences. *Tellus*, **19**, 98-106.

57. Krishnamurti, T. N., J. Xue, H. S. Bedi, K. Ingles, and O. Oosterhof, 1991: Physical initialization for numerical weather prediction over the tropics. *Tellus*, **43A**, 53-81.

58. Krishnamurti, T. N., H. S. Bedi, and K. Ingles, 1993: Physical initialization using SSM/I rain rate. *Tellus*, **45A**, 274-269.

59. Kuo, Y.-H., and G. T.-J. Chen, 1990: The Taiwan Area Mesocale Experiment (TAMEX): An overview. *Bull. Amer. Meteor. Soc.*, **71**, 488-503.

60. Lau, K.-M., L. Peng, C. H. Sui, and T. Nakazawa, 1989: Dynamics of super cloud clusters, westerly wind bursts, 30-60 day oscillations and ENSO: An unified view. *J. Meteor. Soc. Japan*, **67**, 205-219.

61. Lau, K. M., Y. Ding, J.-T. Wang, R. Johnson, T. Keenan, R. Cifelli, J. Geriach, O. Thiele, T. Rickenbach, S.-C. Tsay, and P.-H. Lin, 2000: A report of the field operations and early results of the South China Sea Monsoon experiment (SCSMEX). *Bull. Amer. Meteor. Soc.*, **81**, 1261-1270.

62. Le Dimet, F. X., and O. Talagrand, 1986: Variational algorithms for analysis and assimilation of meteorological observations. Theoretical aspects. T*ellus*, **38**A, 97-110.

63. Lin, X., and R.H. Johnson, 1996: Kinematic and thermodynamic characteritics of the flow over the western pacific warm pool during TOGA-COARE. *J. Atmos. Sci.*, **53**, 695-715.

64. Lin, Y.-L., R. D. Farley, and H. D. Orville, 1983: Bulk parameterization of the snow field in a cloud model. *J. Clim. Appl. Meteor.*, **22**, 1065-1092.

65. Lin, Y.-L., S. Chiao, T.-N. Wang, M.-L., Kaplan, and R. P. Weglarz, 2001: Some common ingredients for heavy orographic rainfall. *Weather and Forecasting*, **16**, 633-

660.

66. Liou, K.-N., Q. Fu, and T. P. Ackerman, 1988: A simple formulation of the delta-four-stream approximation for radiative transfer parameterizations. *J. Atmos. Sci.*, **45**, 1940-1947.

67. Lynn, B. H., W.-K. Tao, and P. Wetzel, 1998: A study of landscape generated deep moist convection. *Mon. Wea. Rev.*, **126**, 928-942.

68. Lynn, B. H., D. Stauffer, P. Wetzel, W.-K. Tao, P. Alpert, N. Perlin, R. D. Baker, R. Munoz, A. Boone, and Y. Jia, 2001: Improved simulation of Florida summer convection using the PLACE land surface model and a 1.5-order turbulence parameterization coupled to the Penn State/NCAR mesoscale model. *Mon. Wea. Rev.*, **129**, 1441-1461.

69. Madden, R., and P. Julian, 1972: Description of global scale circulation cells in the tropics with a 40-50 day period. *J. Atmos. Sci.*, **29**, 1109-1123.

70. Madden, R. and P. Julian, 1994: Observations of the 40-50 day tropical oscillation - A review. *Mon. Wea. Rev.*, **122**, 814-837.

71. Mahfouf, J.-F., E. Richard, and P. Mascart, 1987: The Influence of Soil and Vegetation on the Development of Mesoscale Circulations. *J. Applied Meteor.*, **26**, 1483–1495.

72. Manobianco, J., S. E. Koch, V. M. Karyampudi, and A. J. Negri, 1994: The impact of assimilating satellite-derived precipitation rates on numerical simulations of the ERICA IOP 4 cyclone. *Mon. Wea. Rev.*, **122**, 341-365.

73. Market, P. S., A. R. Lupo, C. E. Halcomb, F. A. Akyuz, and P. Guinan, 2001: Overview of the 7 May 2000 extreme rain event in Missouri. *Symposium on Precipitation Extremes: Prediction, Impacts, and Responses,* Albuquerque, NM, *Amer. Meteor. Soc.*, 162-165.

74. McCumber, M., W.-K. Tao, J. Simpson, R. Penc, and S.-T. Soong, 1991: Comparison of ice-phase microphysical parameterization schemes using numerical simulations of convection. *J. Appl. Meteor.*, **30**, 987-1004.

75. Mellor, G. L., 1996: User guide for a three dimensional, primitive equation numerical ocean model. *Princeton University*, 39pp.

76. Miller, D. (1994), personal communication. STATSGO data obtained from archives maintained at the Earth System Science Center, Penn State University.

77. Molinari, J., 1982: Numerical hurricane prediction using assimilation of remotely-sensed rainfall rates. *Mon. Wea. Rev.*, **110**, 553-571.

78. Navon, I. M., X. Zou, J. Deber, and J. Sela, 1992: Variational data assimilation with an

adiabatic version of the NMC spectral model. *Mon. Wea., Rev.*, **120**, 1433-1446.

79. Parsons, D. B., 1992: An explanation of intense frontal updrafts and narrow cold-frontal rainbands. *J. Atmos. Sci.*, **49**, 1810-1825.

80. Parsons, D. B., C. G. Mohr, and T. Gal-Chen, 1987: A severe frontal rainband. Part III: Derived thermodynamic structure. *J. Atmos. Sci.*, **44**, 1613-1631.

81. Pickering, K., A. Thompson, Y. Wang, W.-K Tao, Bradshaw, Kirchhoff, Alvala, Gregory, Blake, McNamara, and Kucsera, 1996: Convective transport of biomass burning emissions over Brazil during TRACE-A. *J. Geophys. Res.*, **101**, D19, 23993-24012.

82. Pu, Z.-X., and S. A. Braun, 2001: Evaluation of bogus vortex techniques with four-dimensional data assimilation. *Mon. Wea. Rev.*, **129**, 2023-2039.

83. Pu, Z.-X., and W.-K. Tao, 2003: Mesoscale assimilation of TRMM data with 4DVAR. *J. Meteor. Soc. of Japan,* (submitted).

84. Pu, Z.-X., W.-K. Tao, S. Braun, Y. Jia, J. Simpson, J. Halverson, W. Olson, and A. Hou, 2002: The impact of TRMM data on mesoscale numerical simulation of Super Typhoon Paka. *Mon. Wea. Rev.*, **130**, 2448-2458.

85. Qian, J.-H., W.-K. Tao, and K.-M. Lau, 2003: Mechanisms of torrential rain associated with the Mei-yu development during SCSMEX-98. *Mon. Wea. Rev.*, (accepted).

86. Randall, D. A., Harshvardhan, and D. A., Dazlich, 1991: Diurnal variability of the hydrologic cycle in a general circulation model. *J. Atmos. Sci.*, **48**, 40-62.

87. Redelsperger, L., S. Chen, R. H. Johnson, M. A. LeMone, T. Nakazawa, D. B. Parsons, S. A. Rutledege, W.-K. Tao, and M. Yanai, 2000: Review of convection in TOGA COARE. *World Meteorology Organization Monograph,* WCRP-107, 16-42.

88. Rodgers, E. B., W. S. Olson, V. M. Karyampudi, and H. Pierce, 1998: Satellite-derived latent heating distribution and environmental influences in Hurricane Opal (1995). *Mon. Wea. Rev.*, **126**, 1229-1247.

89. Rutledge, S. A., and P. V. Hobbs, 1984: The mesoscale and microscale structure and organization of clouds and precipitation in mid-latitude clouds. Part XII: A diagnostic modeling study of precipitation development in narrow cold frontal rainbands. *J. Atmos. Sci.*, **41**, 2949-2972.

90. Shepherd, J. M., H. Pierce, and A. J. Negri, 2002: On Rainfall Modification by Major Urban Areas-Part I: Observations from Space-borne Radar on TRMM. *J. Applied Meteor.*, **41**, 689-701.

91. Sheih, C.-F., and P.-H. Sheih, 1989: A case study for the reasons on heavy rainfall Aug. 14, 1988. *Weather Forecast and Analysis*, 121, 65-76. (in Chinese with English abstract.)

92. Simpson, J., and W.-K. Tao, 1993: The Goddard Cumulus Ensemble Model. Part II: Applications for studying cloud precipitating processes and for NASA TRMM. *Terrestrial, Atmospheric and Oceanic Sciences*, **4**, 73-116.

93. Simpson, J., J. B., Halverson, B. S. Ferrier, W. A. Petersen, R. H. Simpson, R. Blakeslee, and S. L. Durden, 1998: On the role of "hot towers" in tropical cyclone formation. *Meteorol. Amos. Phys.*, **67**, 15-35.

94. Smith, J., L. A. McMurdie, and J. A. Weinman, 2003: Satellite Detection of Precipitation over the North Pacific. *83rd Annual Meeting of the Am. Met. Soc.*, 2003.

95. Smolarkiewicz, P. K., 1983: A simple positive definite advection scheme with small implicit diffusion. *Mon. Wea. Rev.*, **111**, 479-486.

96. Smolarkiewicz, P. K., 1984: A fully multidimensional positive definite advection transport algorithm with small implicit diffusion. *J. Comput. Phys.*, **54**, 325-362.

97. Smolarkiewicz, P. K., and W.W. Grabowski, 1990: The multidimensional positive advection transport algorithm: nonoscillatory option. *J. Comput. Phys.*, **86**, 355-375.

98. Soong, S.-T., and Y. Ogura, 1973: A comparison between axisymmetric and slab-symmetric cumulus cloud models. *J. Atmos. Sci.*, **30**, 879-893.

99. Stephens, G. L., 1983: The influence of radiative transfer on the mass and heat budget of ice crystals falling in the atmosphere. *J. Atmos. Sci.*, **40**, 1729-1739.

100. Sui, C.-H., and K.-M. Lau, 1988: Origin of low-frequency (Intraseasonal) oscillations in the tropical atmosphere. Part II: Structure and propagation of mobile wave-CISK modes and their modification by lower boundary forcings. *J. Atmos. Sci.*, **46**, 37-56.

101. Sui, C.-H., K.-M. Lau, Y. Takayabu, and D. Short, 1997: Diurnal variations in tropical oceanic cumulus convection during TOGA COARE. *J. Atmos. Sci.* **54**, 637-655.

102. Sui, C.-H., X. Li, K.-M. Lau, and D. Adamec, 1997: Multi-scale air-sea interaction during TOGA COARE. *Mon. Wea. Rev.*, **125**, 448-462.

103. Takayabu, Y. N., K.-M. Lau, C.-H. Sui, 1996: Observation of a quasi two-day wave during TOGA COARE. *Mon. Wea. Rev.*, **124**, 1892-1913.

104. Tao, W.-K., 2002: Goddard Cumulus Ensemble (GCE) model: Application for understanding precipitation processes. *AMS Meteorological Monographs - Cloud Systems, Hurricanes and TRMM.* (in press).

105. Tao, W.-K., and J. Simpson, 1989: Modeling study of a tropical squall-type convective line. *J. Atmos. Sci.*, **46**, 177-202.

106. Tao, W.-K., and J. Simpson, 1993: The Goddard Cumulus Ensemble Model. Part I: Model description. *Terrestrial, Atmospheric and Oceanic Sciences*, **4**, 35-72.

107. Tao, W.-K., J. Simpson, and M. McCumber, 1989: An ice-water saturation adjustment. *Mon. Wea. Rev.*, 117, 231-235.

108. Tao, W.-K., Y. Jia, C.-H. Sui, and C. Chen, 1998: The diurnal cycle in TOGA-COARE: Regional scale model simulations. *WMO/Would Climate Research Program-107, COARE 98*, Ed. F. Bradley and R. Lukas, 321-322.

109. Tao, W.-K., J. Simpson, D. Baker, S. Braun, D. Johnson, B. Ferrier, A. Khain, S. Lang, C.-L. Shie, D. Starr, C.-H. Sui, Y. Wang, and P. Wetzel, 2002: Microphysics, Radiation and Surface Processes in a Non-hydrostatic Model. *Meteorology and Atmospheric Physics,* (invited paper – in press).

110. Tao, W.-K., Y. Wang, J. Qian, W. K.-M. Lau, C.-L. Shie, and R. Kakar, 2002: Mesoscale Convective Systems during SCSMEX: Simulations with a Regional Climate Model and a Cloud-Resolving Model. *INDO-US Climate Research Program*, (in press).

111. Tao, W.-K., C.-L. Shie, D. Johnson, R. Johnson, S. Braun, J. Simpson, and P. E. Ciesielski, 2002: Convective Systems over South China Sea: Cloud-Resolving Model Simulations. *J. Atmos. Sci.* (submitted).

112. Tao, W.-K., C. Chen, D. Duffy, G. Lai, P.-H. Lin, and Y. Jia, 2003: A modeling study of the December 1992 Westerly Wind Burst Event during TOGA COARE. *J. Meteor. Soc. Japan,* (submitted).

113. Tao, W.-K., C.-S. Chen, Y. Jia, S. Lang, R. D. Baker, P. Wetzel, W. K.-M. Lau, Y.-H. Kuo, and J. Dudhia, 2003: A study of precipitation events in Taiwan during 10-11 August 1994: Regional Scale Model Simulations. *J. Meteor. Soc. Japan* (in revision).

114. Texier, D., N. de Noblet, and P. Braconnot, 2000: Sensitivity of the African and Asian Monsoons to Mid-Holocene Insolation and Data-Inferred Surface Changes. *J. of Climate*, **13**, 164–181.

115. Thompson, A. M., W.-K. Tao, K. E. Pickering, J. Scala, and J. Simpson, 1997: Tropical deep convection and ozone formation. *Bull. Amer. Meteor. Soc.*, **78**, 1043-1054.

116. Tsuyuki, T., 1997: Variational data assimilation in the Tropics using precipitation data. Part III: Assimilation of SSM/I precipitation. *Mon. Wea. Rev.*, **125**, 1447-1464.

117. Vongsaard, J., L. Chiu, T. El-Ghazawa, J. Weinman, and C. Yang, 2001: Tracking

Continuous Rain Systems Using a Genetic Based Wavelet Image Registration Technique. *11th AMS Conf. on Satellite Meteorology and Oceanography*, P-57, Madison, WI, Oct. 2001

118. Wang, S.-T., H. Cheng, and Y.-K. Chao, 1984: Natural seasons of the weather in the Taiwan area (in Chinease with English abstract). *Atmos. Sci.*, **11**, 101-120.

119. Wang, Y., W.-K. Tao, K. Pickering, A. Thompson, J. Kain, R. Adler, J. Simpson, P. Keehn, and G. Lai, 1996: Mesoscale model (MM5) simulation of TRACE and PRESTORM Convective Systems and Associated Tracer Transport. *J. Geophys. Res.*, **101, D19**, 24013-24027.

120. Wang, Y., W.-K. Tao, and J. Simpson, and S. Lang, 2002: The sensitivity of tropical squall lines (GATE and TOGA COARE) to surface fluxes: 3-D Cloud resolving model simulations. *Q. J. R. Met. Soc.*, (in press).

121. Wang, Y., W.-K. Tao, K.-M. Lau, and P. J. Wetzel, 2003: Simulation of southeast Asian monsoon onset during 1997 and 1998: The impact of surface processes. *J. Geophy. Res.*, (submitted).

122. Webster, P. J., and R. Lukas, 1992: TOGA COARE: the coupled Ocean Atmosphere Response Experiment. *Bull. Amer. Meteor. Soc.*, **73**, 1377-1417.

123. Webster, P. J., and G. L. Stephens, 1980: Tropical upper troposphere extended clouds: Inferences from Winter MONEX. *J. Atmos. Sci.*, **37**, 1521-1541.

124. Wetzel, P. J., and A. Boone,1995: A parameterization for land-atmosphere-cloud exchange (PLACE): Documentation and testing of a detailed process model of the partly cloudy boundary layer over heterogeneous land. *J. of Climate* , **8,** 1810-1837.

125. Xiao, Q., X. Zou, and B. Wang, 2000: Initialization and simulation of a landfaling hurricane using a variational bogus data assimilation scheme. *Mon. Wea. Rev.*, **128**, 2252-2269.

126. Zhang, D.-L., and R. A. Anthes, 1982: A high-resolution model of the planetary boundary layer-sensitivity tests and comparisons with SESAME-79 data. *J. Appl. Meteor.*, **21**, 1594-1609.

127. Zhang, D.-L., Y. Liu, and M. K. Yau, 2000: A multiscale numerical study of Hurricane Andrew (1992). Part III: Dynamically induced vertical motion. *Mon. Wea. Rev.*, **128**, 3772-3788.

128. Zou, X., and Y.-H. Kuo, 1996: Rainfall assimilation through an optimal control of initial and boundary conditions in a limited-domain mesoscale model. *Mon. Wea. Rev.*, **124**, 2859-2882.

129. Zou, X., and Q. Xiao, 2000: Studies on theinitialization and simulation of a mature hurricane using a variational bogus data assimilation scheme. *J. Atmos. Sci.*, **57**, 836-860.

130. Zou, X., W. Huang and Q. Xiao, 1998: A user's guide to the MM5 adjoint modeling system. NCAR TN-437+IA. MMM Division, NCAR. [Available from NCAR Publication Office, P. O. Box 3000, Boulder, CO 80307]

131. Zupanski, D., and F. Mesinger, 1995: Four-dimensional variational assimilation of prediction data. *Mon. Wea. Rev.*, **123**, 1112-1127.

# FIGURE CAPTIONS

Fig. 1 Meridonal distribution of daily rain rate (mm $day^{-1}$), averaged from 110 E to 122 E for the TRMM observed (dash-circle), station observed (long dash), control run (solid) and NF (dash).

Fig. 2 The two right panels show time series of daily rainfall simulated by the improved MM5 (with 60 and 20 km-nested domains) for 1997 and 1998. TRMM- and GPCP-derived rainfall are also shown for comparison. The impact of surface temperature is small for both cases but not with regard to land processes. The use of a sophisticated and realistic land surface model (PLACE) and land characteristics produced better agreement with observations and satellite-derived rainfall. The two left panels show the water vapor budget over the northern part of the S. China Sea. Water vapor inflow into the box is positive and outflow is negative. P is precipitation; E is the evaporation from the surface; W is the total change in water vapor; and R is the residual. The units are $10^{13}$kg/day.

Fig. 3 Vertical profiles of change in CO over the TRACE-A fine mesh domain comparing transport by grid and sub-grid scale (parameterized) components.

Fig. 4 MM5 simulation results of CO transport. Mixing ratios at 1200 UTC September 27, 1992, at altitudes of **(a)** 9.5 km and **(b)** 11.5 km. The region shown is for the MM5 fine-grid domain (30-km resolution). The results are due to both grid-scale and sub-grid (parameterized) transport. Solid lines represent the NASA DC-8 aircraft tracks along which cloud-processed air was sampled.

Fig. 5 Frequency distributions of both observed and simulated CO for a TRACE-A event at **(a)** 11.5 km and **(b)** 9.5 km. GR stands for the Grell [40] cumulus parameterization scheme and KF for the Kain and Fritsch [52] scheme.

Fig. 6 Horizontal cross section of vertical velocity (light shading > 1 m $s^{-1}$, dark shading > 3 m $s^{-1}$) and perturbation virtual potential temperature (positive contours only, drawn at 1 K intervals starting at 0.5 K) associated with wavenumbers 2 and higher at the 3.2 km level from a 1.3-km grid scale simulation of Hurricane Bob. (Adapted from [9])

Fig. 7 **(a)** Profiles of trajectory radius versus height for a set of air parcel trajectories released within the eyewall at the 2-km level. Trajectories are calculated backward for 2 h and forward for 4 h using 2-min model output. Trajectories 1-3 show the paths of parcels into the storm and rising within the eyewall. Trajectory 4 originates within the eye and is eventually entrained into the eyewall. **(b)** Profiles of trajectory $\theta_e$ versus height. In (a) and (b), small arrows indicate the general direction of movement of the air parcels. (Adapted from [9])

Fig. 8 Location of the model domains for the simulation of Hurricane Bonnie (1998). Domain C is the 36-km grid and domain D is the nested 12-km grid used in the forecast. Domain D is moved during the simulation from D1 to D2 at 18 h. Estimates of the center location at 6-h intervals are marked by circles. The minimum Sea Level Pressure (hPa) and maximum surface wind (m $s^{-1}$) are shown inside the brackets. The period included in the simulation is marked by the bold segment of the track.

Fig. 9 Model-predicted minimum sea level pressure (mb) and total (convective and non-convective) rainfall rates (mm/h; scale given at the side of each panel) at 12 and 24 h from the control simulations (top), with rainfall assimilation (middle) and with ODW-enhanced initial conditions (bottom).

Fig. 10 Minimum sea level pressure forecasts from the control and the two sensitivity simulations (one assimilating SSM/I-derived rainrates and the other assimilating both rainrates and vertical latent heating profiles). The observed central pressure from the best track data is also shown for comparison.

Fig. 11 Left, center and right images show rainfall rate distributions derived from SSM/I microwave radiometry. The second and fourth images are morphed rainfall distributions using IR and lightning to scale the motion and intensity at intervening times.

Fig. 12 Minimum sea level pressure vs time. The observed trend is compared to several model runs that assimilated rainfall using several different techniques.

Fig. 13 Sample composite from SSM/I, NOAA-15, NOAA-16, and TMI microwave radiometers **(a)**. Sample time is 17:00 UTC 4 December 2001. Satellite overpasses are within four hours of this time and storms were moved using GOES-derived winds. **(b)** is the same as (a) except that the composite is produced by simply averaging the swaths together without first moving them. **(c)** GOES-10 infrared brightness temperature imagery at 8-km horizontal resolution obtained at 17:00 UTC on 4 December 2001.

Fig. 14 Mesoscale numerical model simulaton of super typhoon Paka (1997) using two-way interactive nested grids (at 135-, 45- and 15-km resolution) and Goddard Data Assimilating System (GDAS) data for model initialization. The left and middle panels show model-simulated rate rates without and with TRMM rainfall assimilation into the GDAS, respectively. Convective structures of the storm represented by SSM/I 85 GHz brightness temperature are shown in left panel for comparison.

Fig. 15 Rainfall forecast for Hurricane Bonnie (1998) from a regional scale model using a 4-km grid size. Rainfall with **(a)** and without **(b)** assimilating TMI rainfall into the model using 4DVAR. TMI retrieved rainfall is shown in **(c)** for comparison.

Fig. 16 MM5-simulated rain rates (shaded, mm $h^{-1}$) and streamlines at height of 1 km. The top panel is for 0000 UTC on December 25 (after 10 days of model integration). Boxes with labels are used to identify the location of disturbances associated with large-scale waves. The modeled WWB (strong gradient in the streamlines) is closely associated with a large-scale cyclonic circulation (number 5). The middle and bottom panels are for 0000 UTC on December 27 and 29, respectively. Satellite IR images showed a strong cyclonic circulation near 12 S and 170 E.

Fig. 17 Four-hour accumulated precipitation field (top 4 panels) and PBL equivalent potential temperature (bottom 4 panels) simulated by MM5 and composited into four quadrants over the west Pacific warm pool region. The MM5 domain extends from 30 S to 20 N and from 150 E to 165 W. Two nested domains with grid resolutions of 135 and 45 km, respectively, were employed. The simulation was run for 12 days, from 19 to 30 December 1992.

Fig. 18 MM5 preprocessor provided soil moisture (top left) and soil temperature (bottom left). Offline simulations of the PLACE model produced soil moisture and soil temperature fields, shown in plots respectively, at the top right and bottom right. The time was 0000 UTC 27 July 1991. Lake Okeechobee is shown at the lower right corner of the domain. Note that the domain is assumed to contain no grid cells dominated by permanent wetlands. All soils are assumed to be well drained to at least 1-m in depth.

Fig. 19 Twenty four-hour accumulated rainfall for the 6-7 May 2000 Missouri flood simulations: **(a)** 5-km grid spacing with 40-km Eta reanalysis initialization, **(b)** 5-km grid spacing with 2.5 degree NCEP global reanalysis initialization, **(c)** 1.7-km grid spacing with Eta initialization, and **(d)** 1.7-km grid spacing with NCEP initialization. Note that the inner domain in the 5-km runs covers a larger area than the inner domain in the 1.7-km runs.

Fig. 20 Time series of accumulated rainfall at 38.2 N, 91.5 W for the four 6-7 May 2000 Missouri flood simulations. This location experienced the heaviest observed rainfall of the event (344 mm).

Fig. 21 Influence of soil moisture heterogeneity on land surface latent heat distribution as modeled by MM5-PLACE for June 10, 1992, 12PM local time. Results presented are after six hours of simulation. Cases I and II possess equal domain-averaged initial soil moisture amounts but different sub-domain distributions. The different soil moisture spatial distributions lead to differences in domain-averaged latent heat.

Fig. 22 **(a)** Visible GOES satellite imagery at 2003 UTC 28 December 1988. Note the two bands of convection interconnected with each other in a region from Washington D. C. to Fredericksburg, Virginia (adapted after [56]). **(b)** MM5-simulated rain rate (shaded, mm $h^{-1}$) at 2000 UTC 28 December 1998.

Fig. 23 MM5 was used to simulate a Narrow Cold Frontal Rainband (NCFR) that occurred during PACJET 2001. The numerical simulations were conducted using nested-grids with resolutions of 36km, 12km, 4km and 1.3km. The high-resolution domain was able to reproduce the main structural features of the observed NCFR. The breaks (gaps) along the rainband are well represented. Based on the simulated results, many aspects of NCFR structure depicted in previous studies were confirmed [51].

Fig. 24 Daily rainfall amount on **(a)** August 10, **(b)** August 11, **(c)** August 12, and **(d)** August 13, 1994. The contour intervals for topography are 500, 1500, 2500m (dashed lines). The rainfall amount is denoted by the gray scale with 10, 20, 40, 80, 160, 320 and 400 mm. They are estimated by 243 hourly rainfall stations and 22 conventional stations.

Fig. 25 Daily accumulated rainfall simulated by the MM5 for **(a)** August 10, **(b)** August 11, **(c)** August 12 and **(d)** August 13, 1994. The simulated rainfall is obtained from the 5-km resolution domain. LST stands for local standard time.

Fig. 26 **(a)** shows the MM5 forecast surface rainfall at 2100 UTC June 15. **(b)** is the NEXRAD radar for comparison.

Fig. 27 Same as Fig. 26 except for a sea-breeze convective event.

Fig. 28 Schematic diagram shows the regional modeling activities at NASA Goddard Space Flight Center.

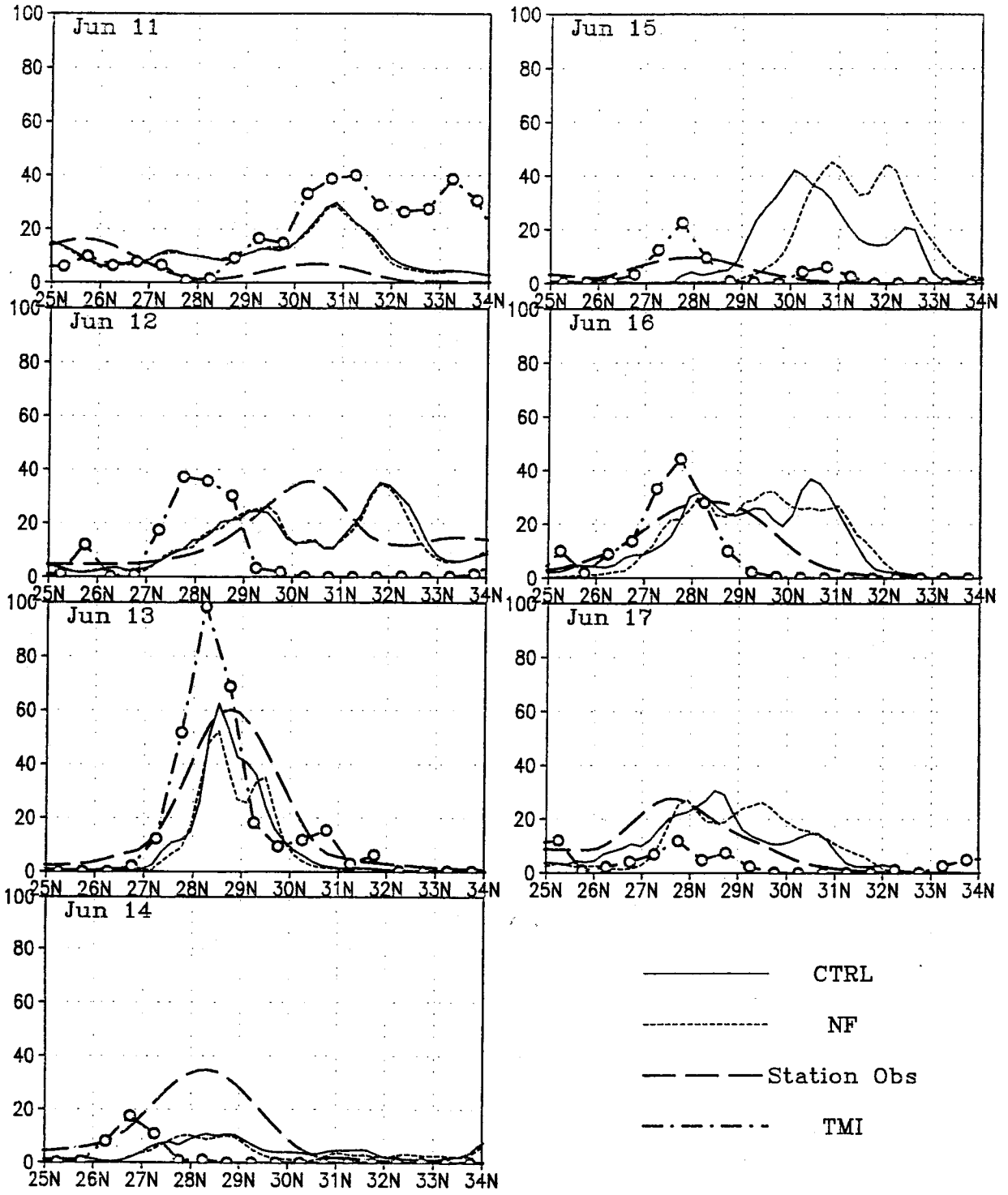


Fig. 1 Meridonal distribution of daily rain rate (mm $day^{-1}$), averaged from 110 E to 122 E for the TRMM observed (dash-circle), station observed (long dash), control run (solid) and NF (dash).

# Regional Climate Simulations over S. China Sea

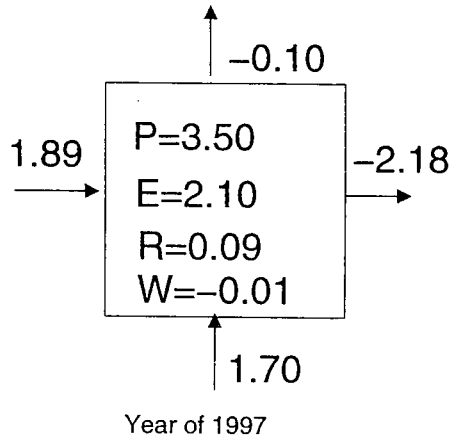


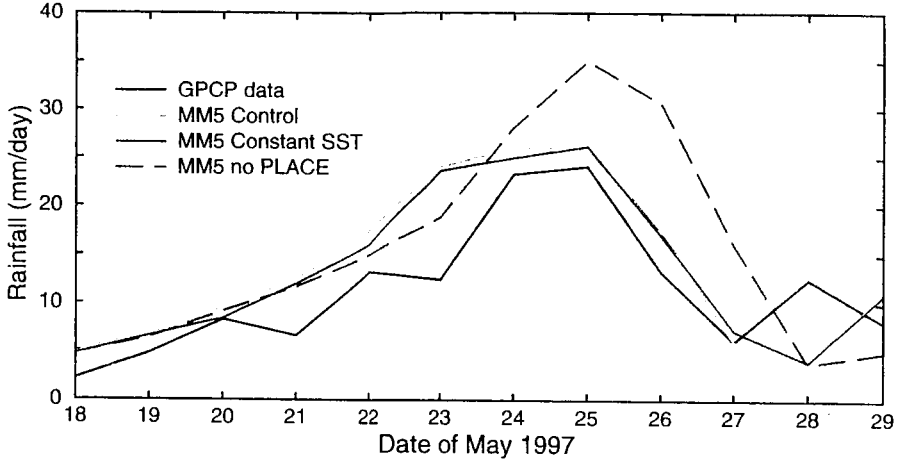


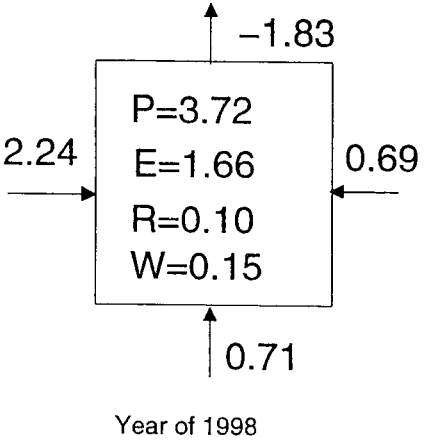


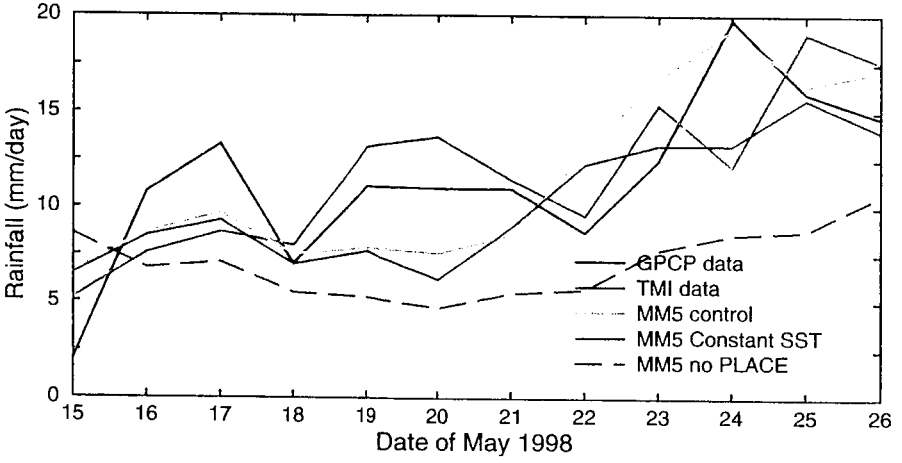


Fig. 2 The two right panels show time series of daily rainfall simulated by the improved MM5 (with 60 and 20 km-nested domains) for 1997 and 1998. TRMM- and GPCP-derived rainfall are also shown for comparison. The impact of surface temperature is small for both cases but not with regard to land processes. The use of a sophisticated and realistic land surface model (PLACE) and land characteristics produced better agreement with observations and satellite-derived rainfall. The two left panels show the water vapor budget over the northern part of the S. China Sea. Water vapor inflow into the box is positive and outflow is negative. P is precipitation; E is the evaporation from the surface; W is the total change in water vapor; and R is the residual. The units are $10^{13}$kg/day.

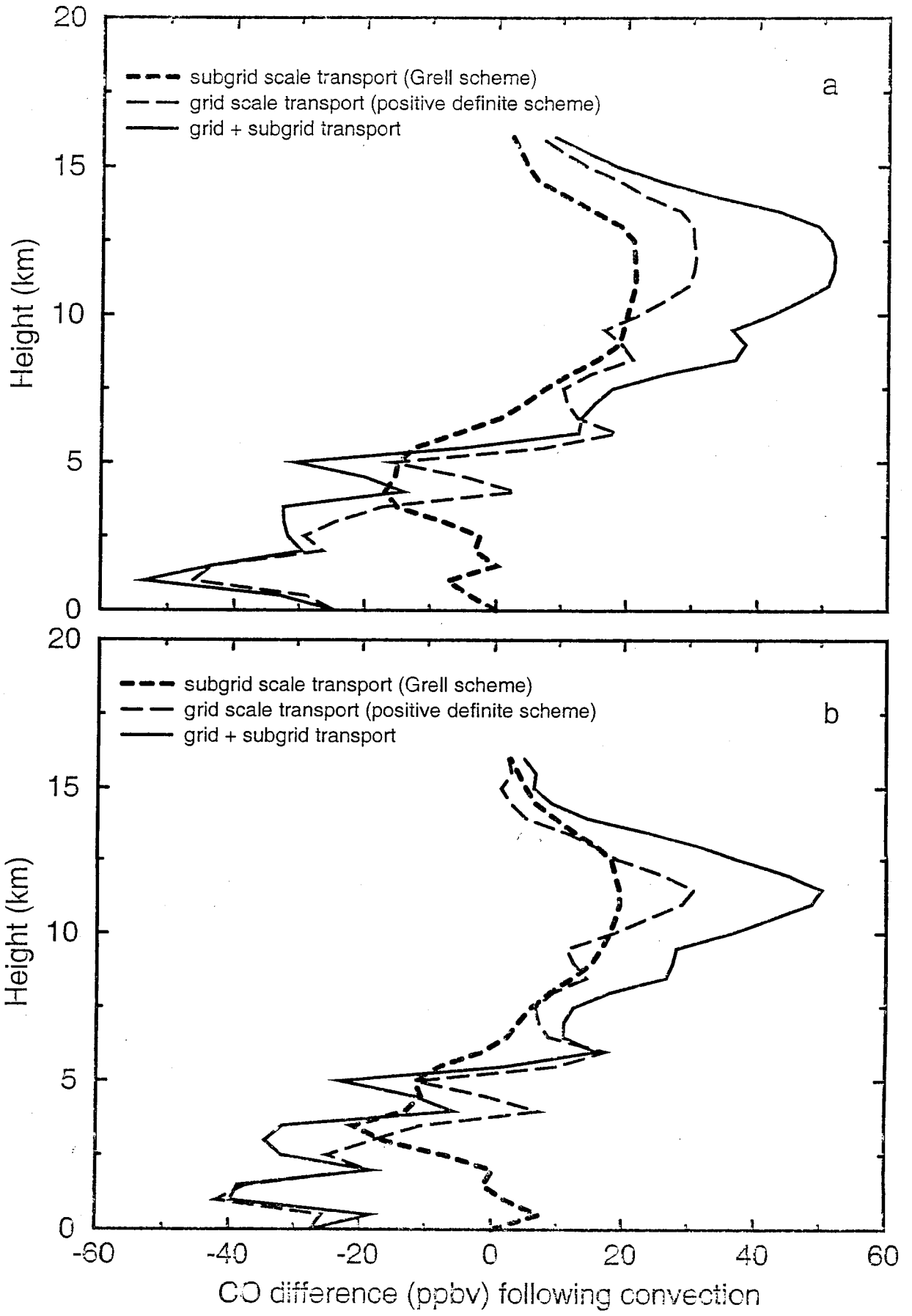


Fig. 3 Vertical profiles of change in CO over the TRACE-A fine mesh domain comparing transport by grid and sub-grid scale (parameterized) components.

# MM5 Simulation of System Sampled on GTE/TRACE-A

## Positive definite scheme, grid+subgrid scale transport

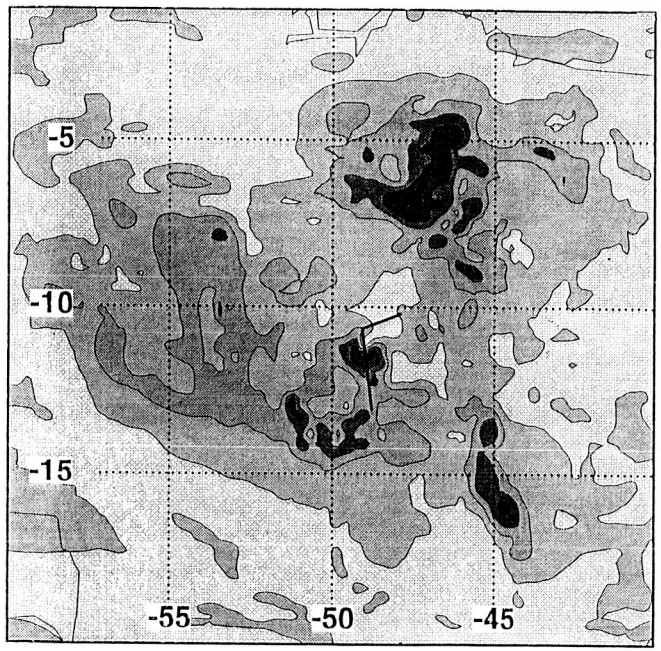


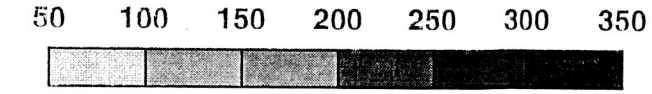


CO mixing ratio(ppbv) at Z=9.5 km (GR scheme)

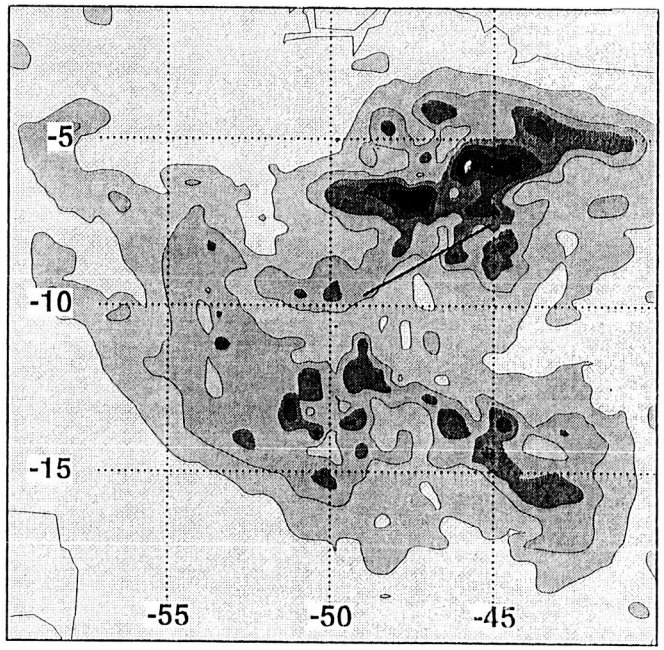


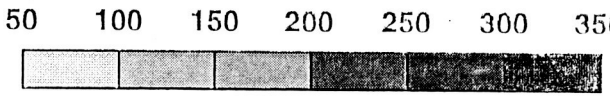


CO mixing ratio(ppbv) at Z=11.5 km (GR scheme)

Fig. 4 MM5 simulation results of CO transport. Mixing ratios at 1200 UTC September 27, 1992, at altitudes of (a) 9.5 km and **(b)** 11.5 km. The region shown is for the MM5 fine-grid domain (30-km resolution). The results are due to both grid-scale and sub-grid (parameterized) transport. Solid lines represent the NASA DC-8 aircraft tracks along which cloud-processed air was sampled

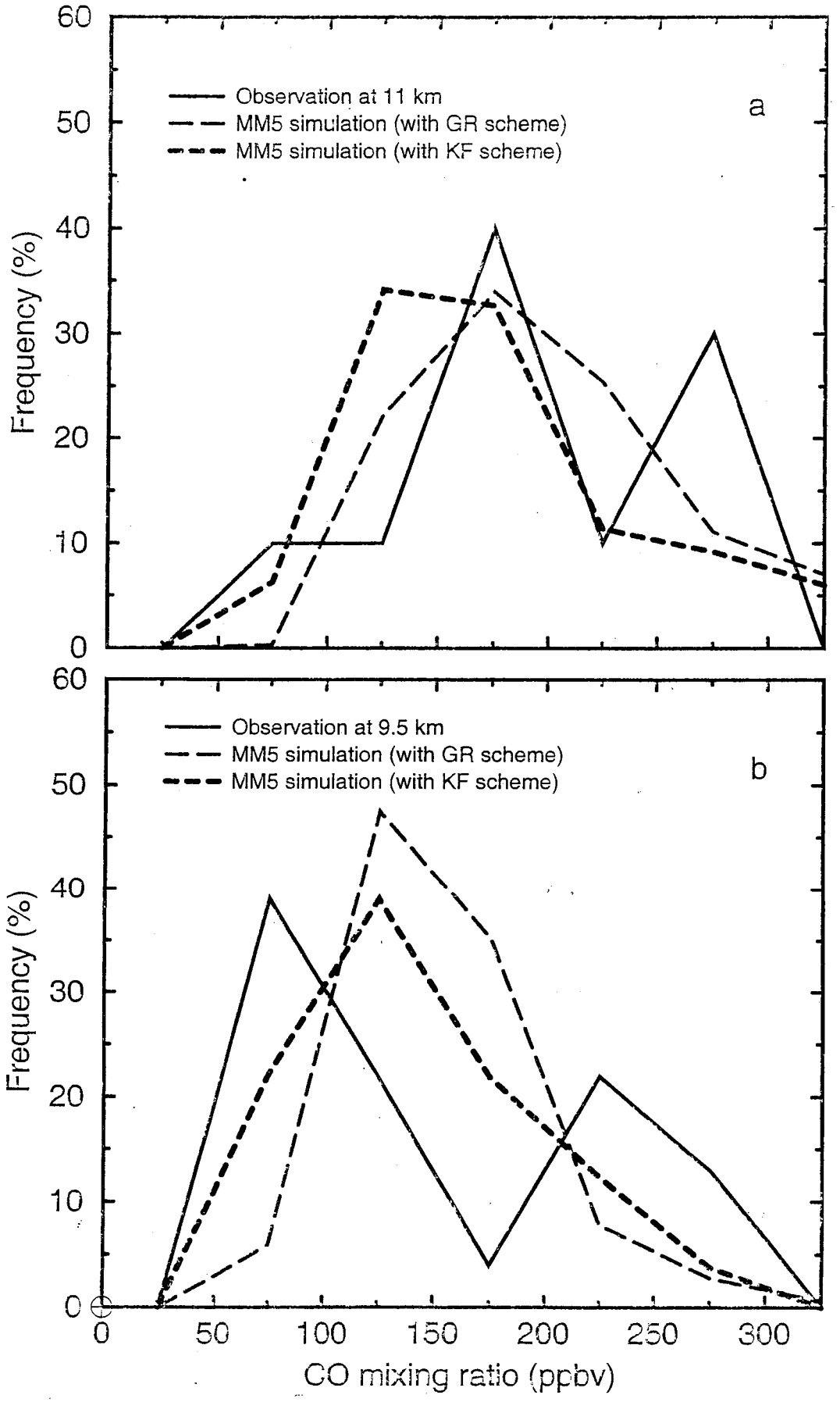


Fig. 5 Frequency distributions of both observed and simulated CO for a TRACE-A event at (a) 11.5 km and (b) 9.5 km. GR stands for the Grell [40] cumulus parameterization scheme and KF for the Kain and Fritsch [52] scheme.

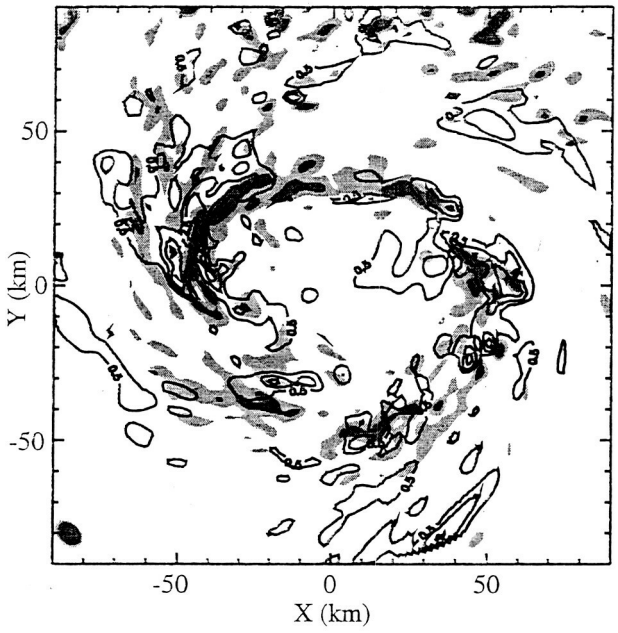


Fig. 6 Horizontal cross section of vertical velocity (light shading > 1 m $s^{-1}$, dark shading > 3 m $s^{-1}$) and perturbation virtual potential temperature (positive contours only, drawn at 1 K intervals starting at 0.5 K) associated with wavenumbers 2 and higher at the 3.2 km level from a 1.3-km grid scale simulation of Hurricane Bob. (Adapted from [9])

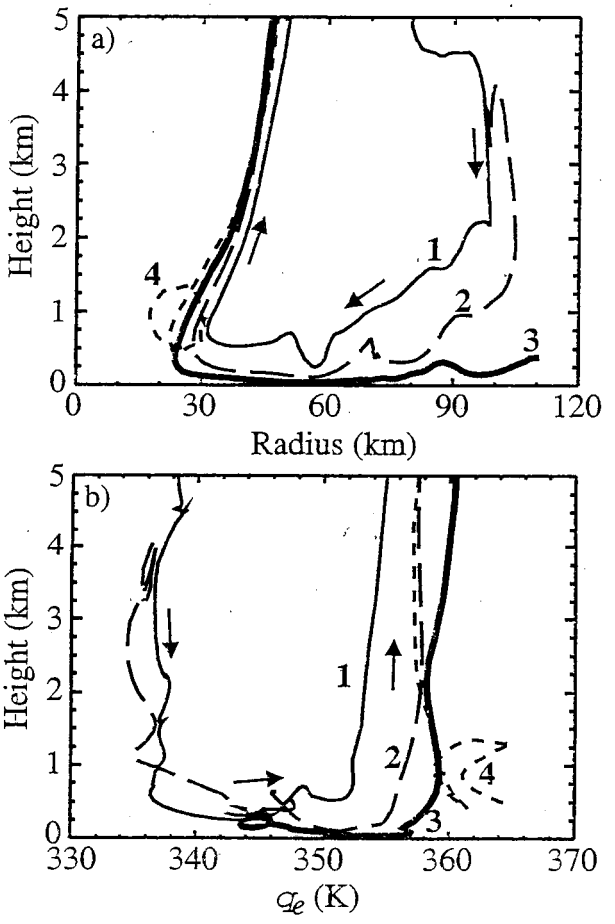


Fig. 7 **(a)** Profiles of trajectory radius versus height for a set of air parcel trajectories released within the eyewall at the 2-km level. Trajectories are calculated backward for 2 h and forward for 4 h using 2-min model output. Trajectories 1-3 show the paths of parcels into the storm and rising within the eyewall. Trajectory 4 originates within the eye and is eventually entrained into the eyewall. **(b)** Profiles of trajectory $\theta_e$ versus height. In (a) and (b), small arrows indicate the general direction of movement of the air parcels. (Adapted from [9])

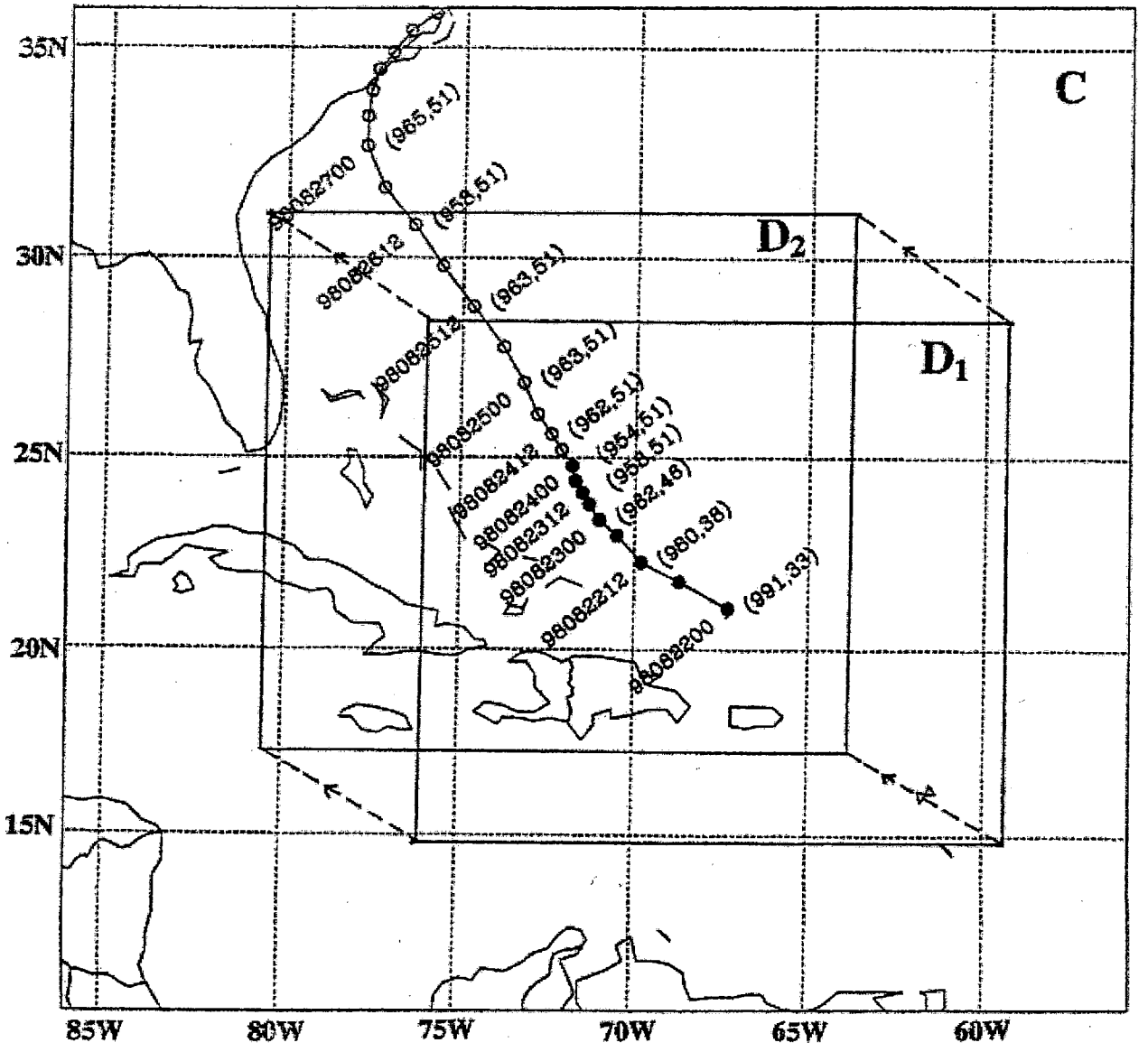


Fig. 8 Location of the model domains for the simulation of Hurricane Bonnie (1998). Domain C is the 36-km grid and domain D is the nested 12-km grid used in the forecast. Domain D is moved during the simulation from D1 to D2 at 18 h. Estimates of the center location at 6-h intervals are marked by circles. The minimum Sea Level Pressure (hPa) and maximum surface wind (m $s^{-1}$) are shown inside the brackets. The period included in the simulation is marked by the bold segment of the track.

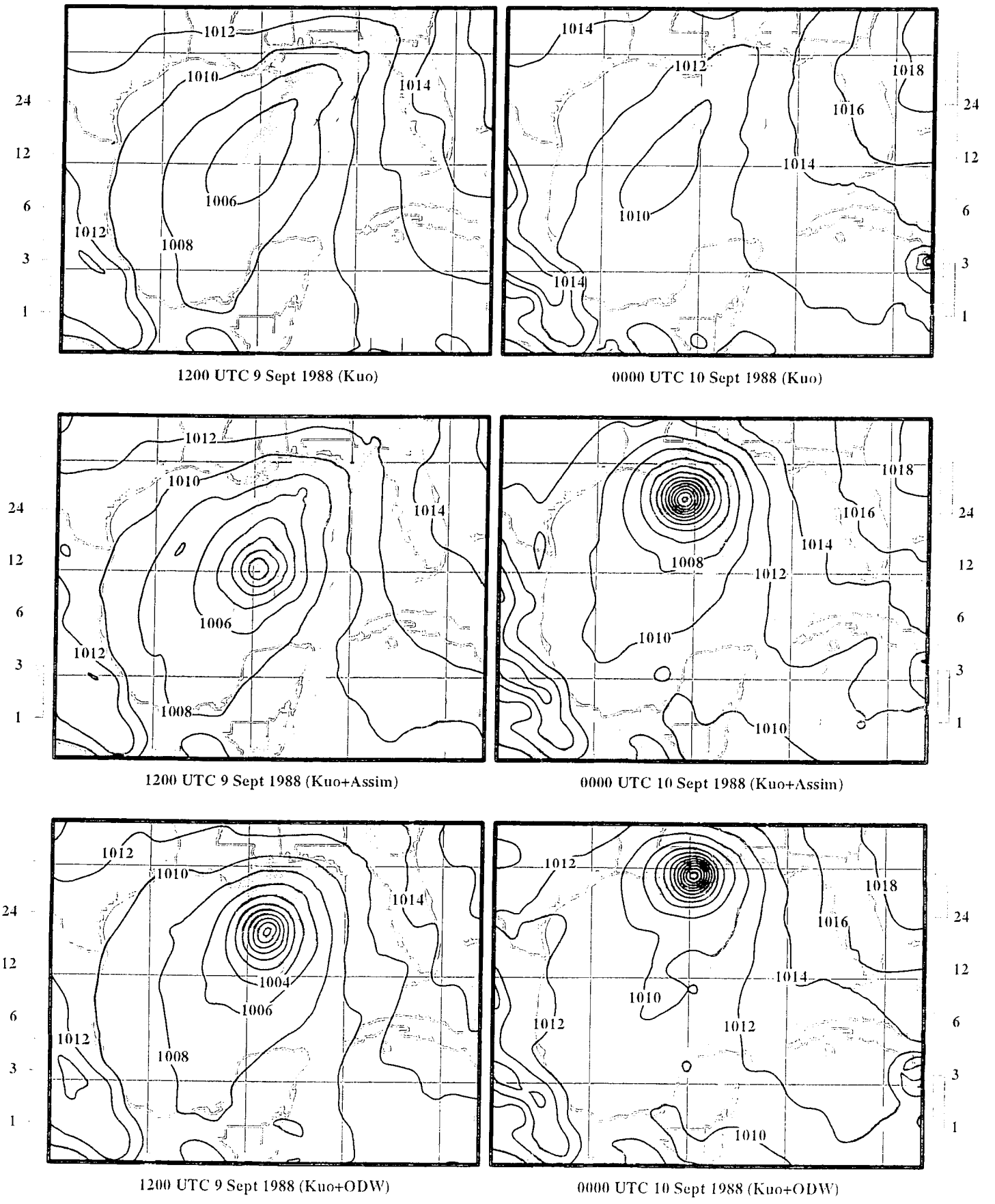


Fig. 9 Model-predicted minimum sea level pressure (mb) and total (convective and non-convective) rainfall rates (mm/h; scale given at the side of each panel) at 12 and 24 h from the control simulations (top), with rainfall assimilation (middle) and with ODW-enhanced initial conditions (bottom).

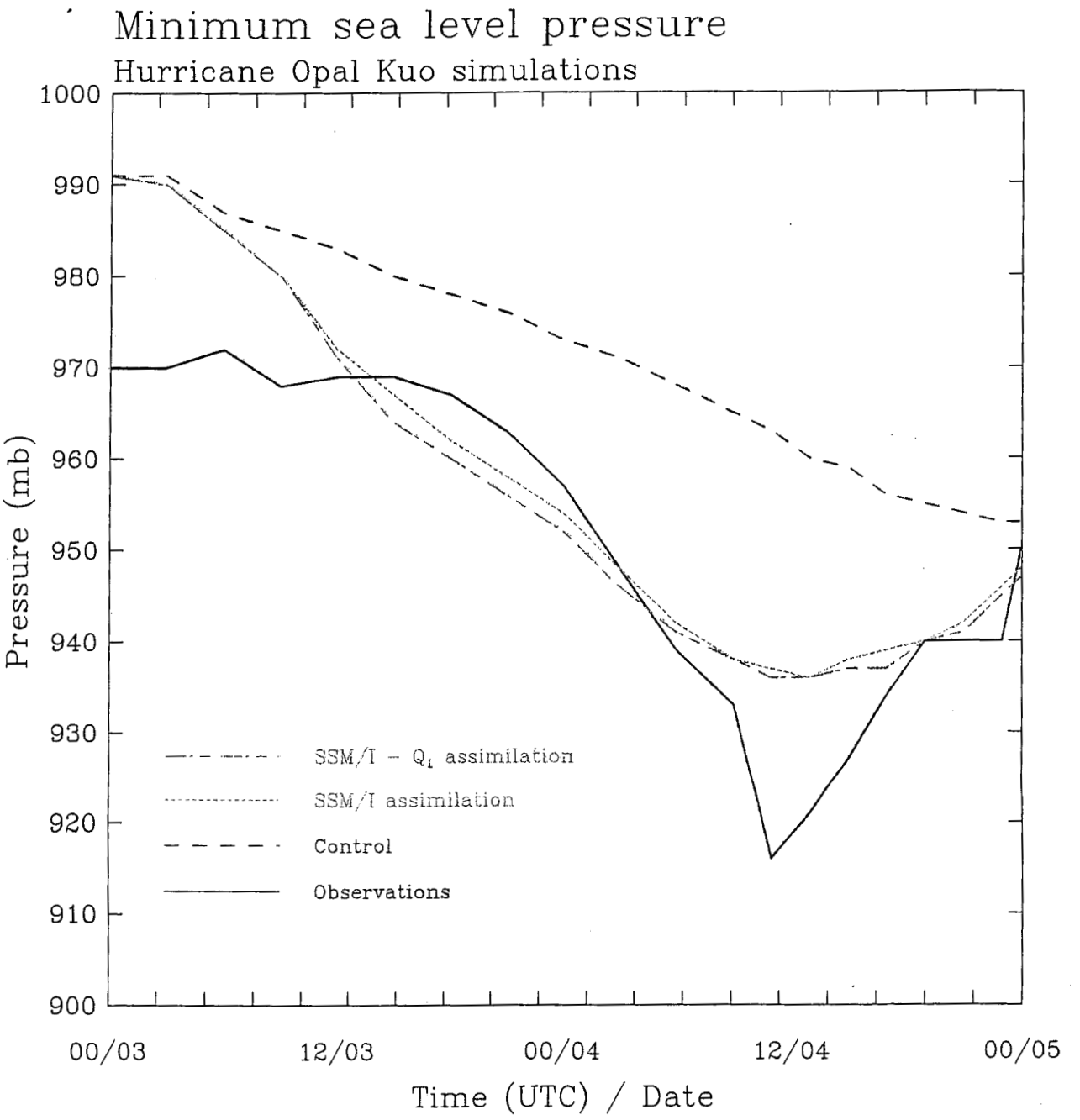


Fig. 10 Minimum sea level pressure forecasts from the control and the two sensitivity simulations (one assimilating SSM/I-derived rainrates and the other assimilating both rainrates and vertical latent heating profiles). The observed central pressure from the best track data is also shown for comparison.

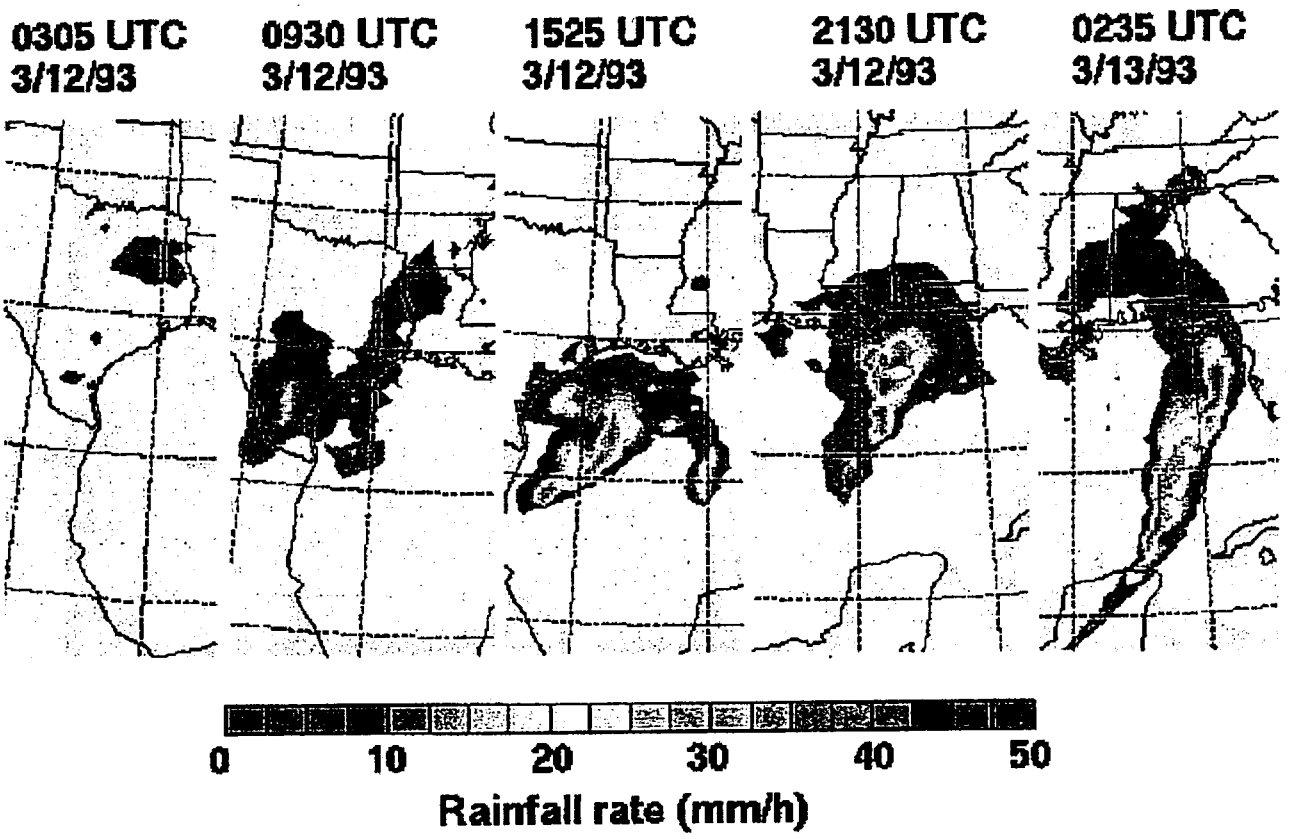


Fig. 11 Left, center and right images show rainfall rate distributions derived from SSM/I microwave radiometry. The second and fourth images are morphed rainfall distributions using IR and lightning to scale the motion and intensity at intervening times.

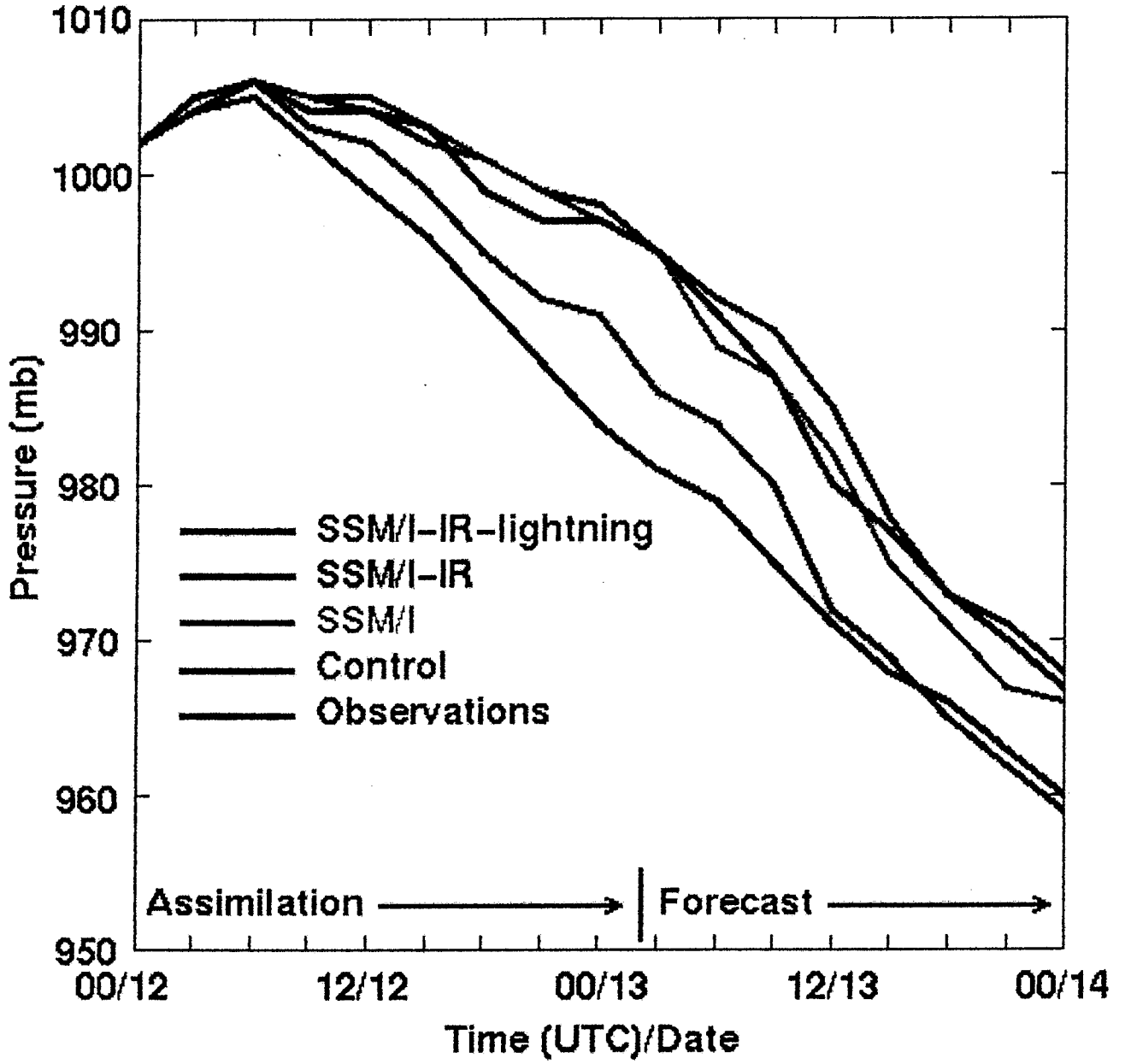


Fig. 12 Minimum sea level pressure vs time. The observed trend is compared to several model runs that assimilated rainfall using several different techniques.

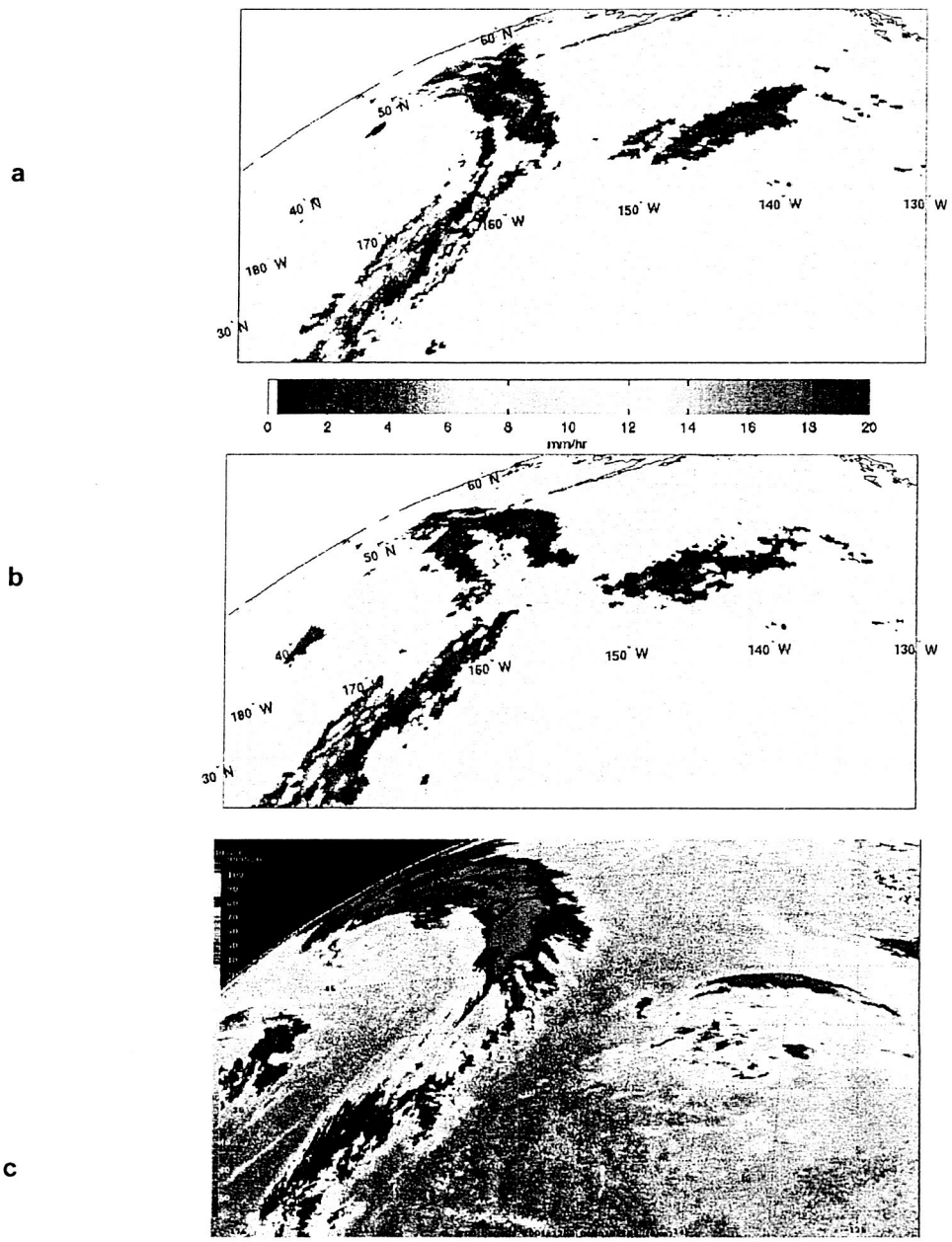


Fig. 13 Sample composite from SSM/I, NOAA-15, NOAA-16, and TMI microwave radiometers **(a)**. Sample time is 17:00 UTC 4 December 2001. Satellite overpasses are within four hours of this time and storms were moved using GOES-derived winds. **(b)** is the same as (a) except that the composite is produced by simply averaging the swaths together without first moving them. **(c)** GOES-10 infrared brightness temperature imagery at 8-km horizontal resolution obtained at 17:00 UTC on 4 December 2001.

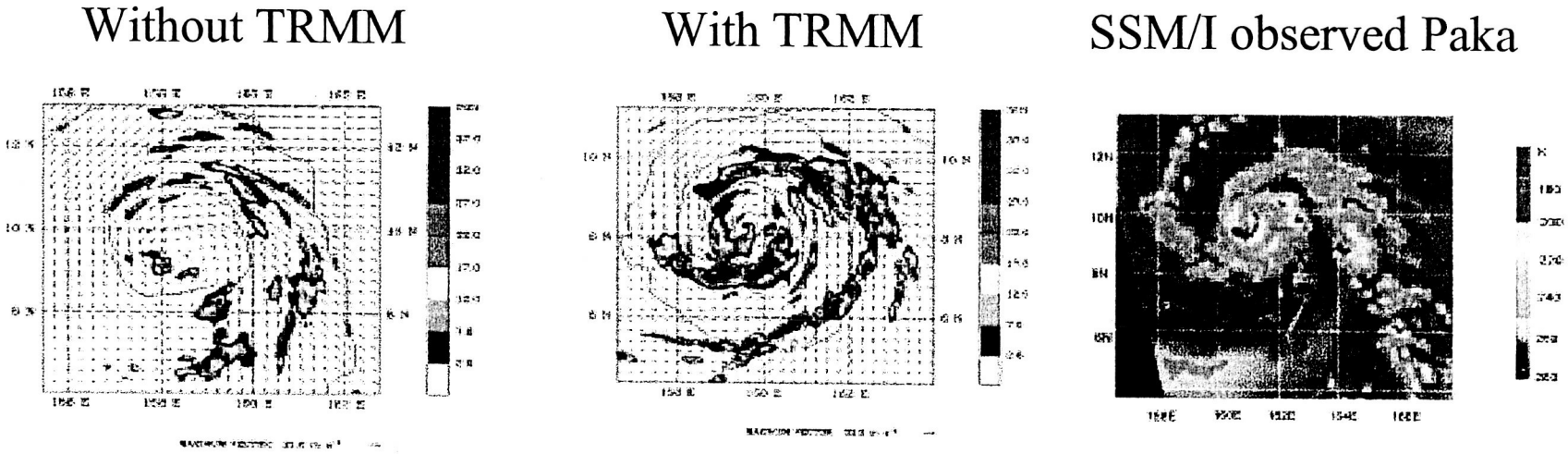


Fig. 14 Mesoscale numerical model simulaton of super typhoon Paka (1997) using two-way interactive nested grids (at 135-, 45- and 15-km resolution) and Goddard Data Assimilating System (GDAS) data for model initialization. The left and middle panels show model-simulated rate rates without and with TRMM rainfall assimilation into the GDAS, respectively. Convective structures of the storm represented by SSM/I 85 GHz brightness temperature are shown in left panel for comparison.

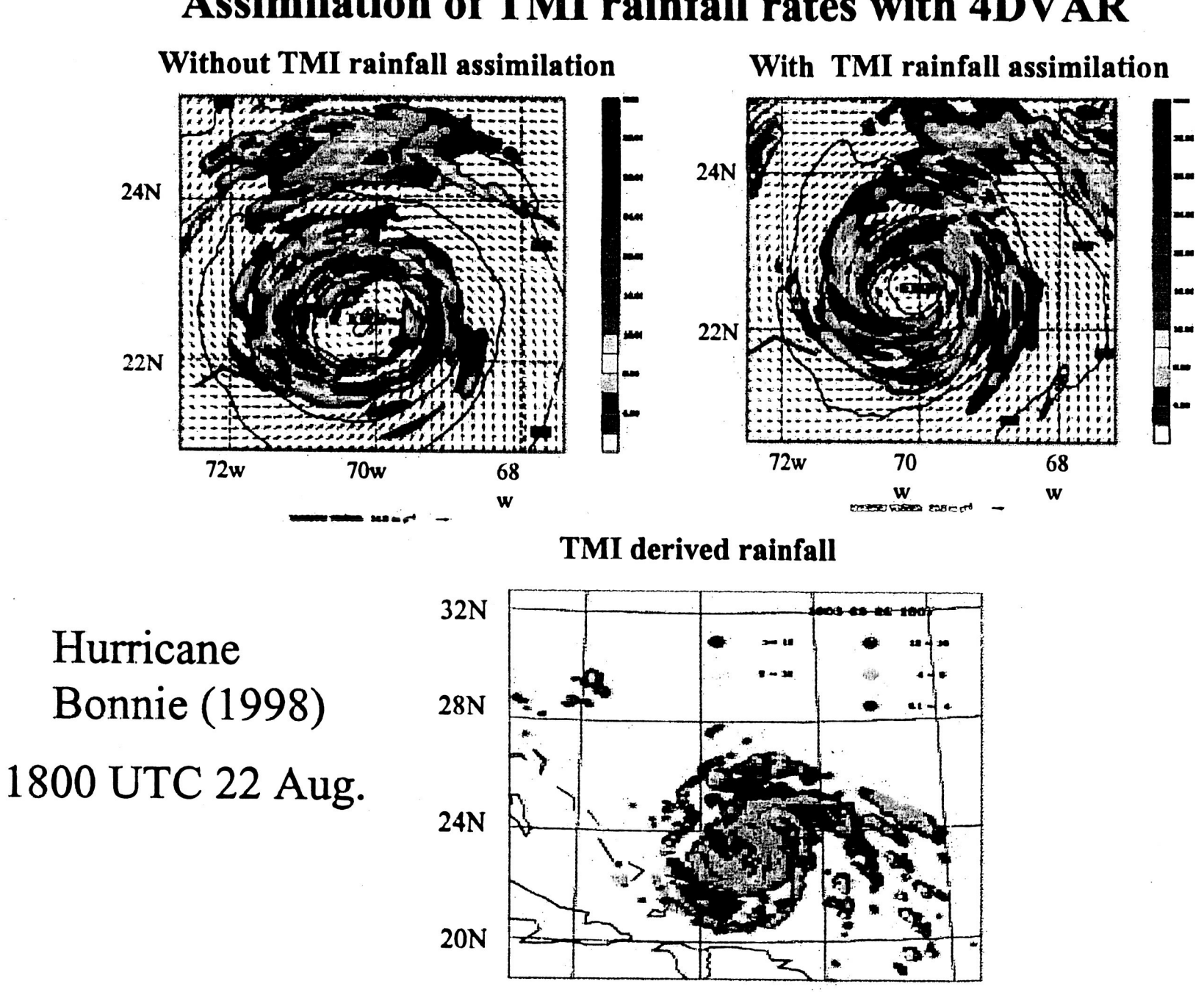


Fig. 15 Rainfall forecast for Hurricane Bonnie (1998) from a regional scale model using a 4-km grid size. Rainfall with **(a)** and without **(b)** assimilating TMI rainfall into the model using 4DVAR. TMI retrieved rainfall is shown in **(c)** for comparison.

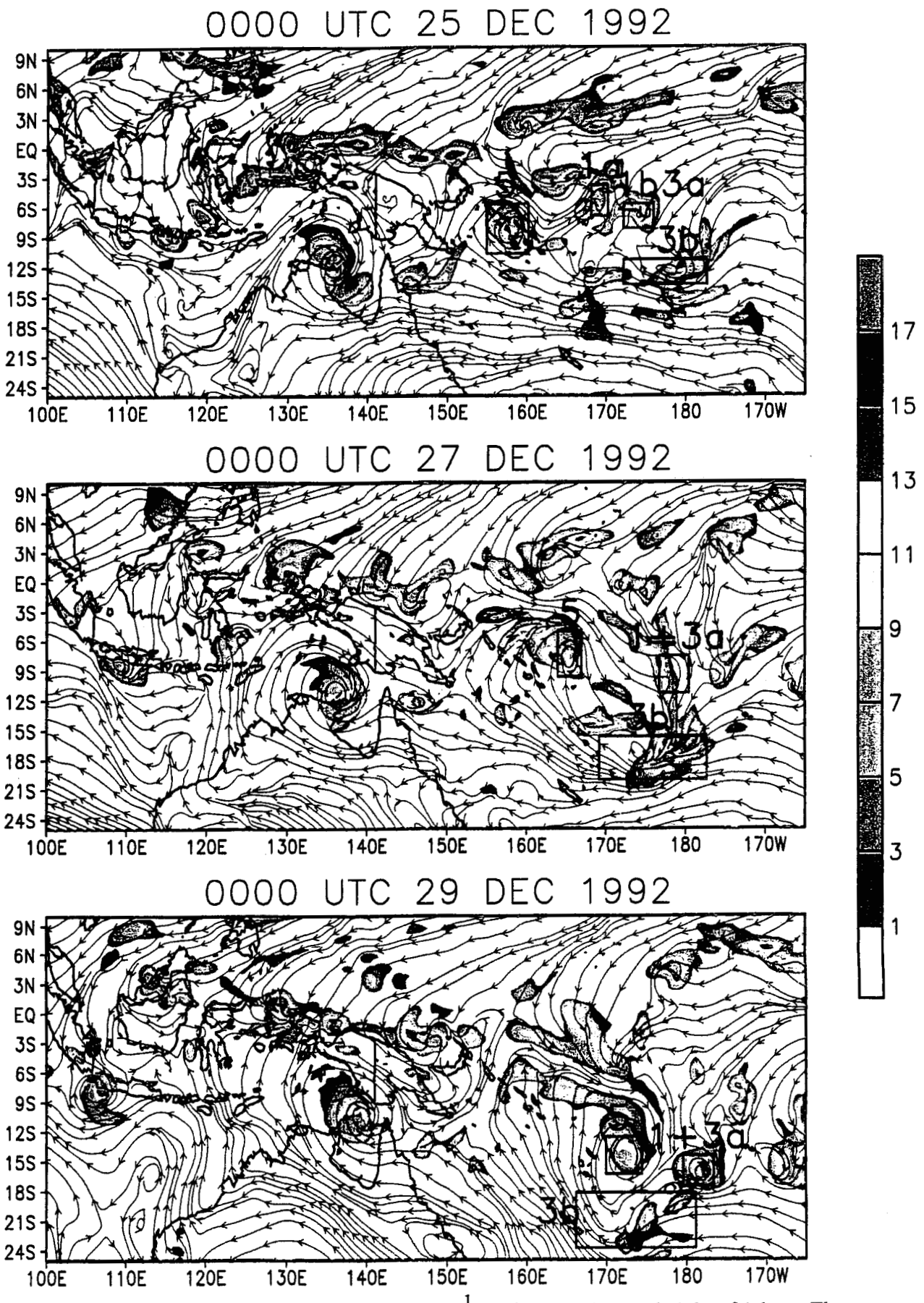


Fig. 16 MM5-simulated rain rates (shaded, mm $h^{-1}$) and streamlines at height of 1 km. The top panel is for 0000 UTC on December 25 (after 10 days of model integration). Boxes with labels are used to identify the location of disturbances associated with large-scale waves. The modeled WWB (strong gradient in the streamlines) is closely associated with a large-scale cyclonic circulation (number 5). The middle and bottom panels are for 0000 UTC on December 27 and 29, respectively. Satellite IR images showed a strong cyclonic circulation near 12 S and 170 E.

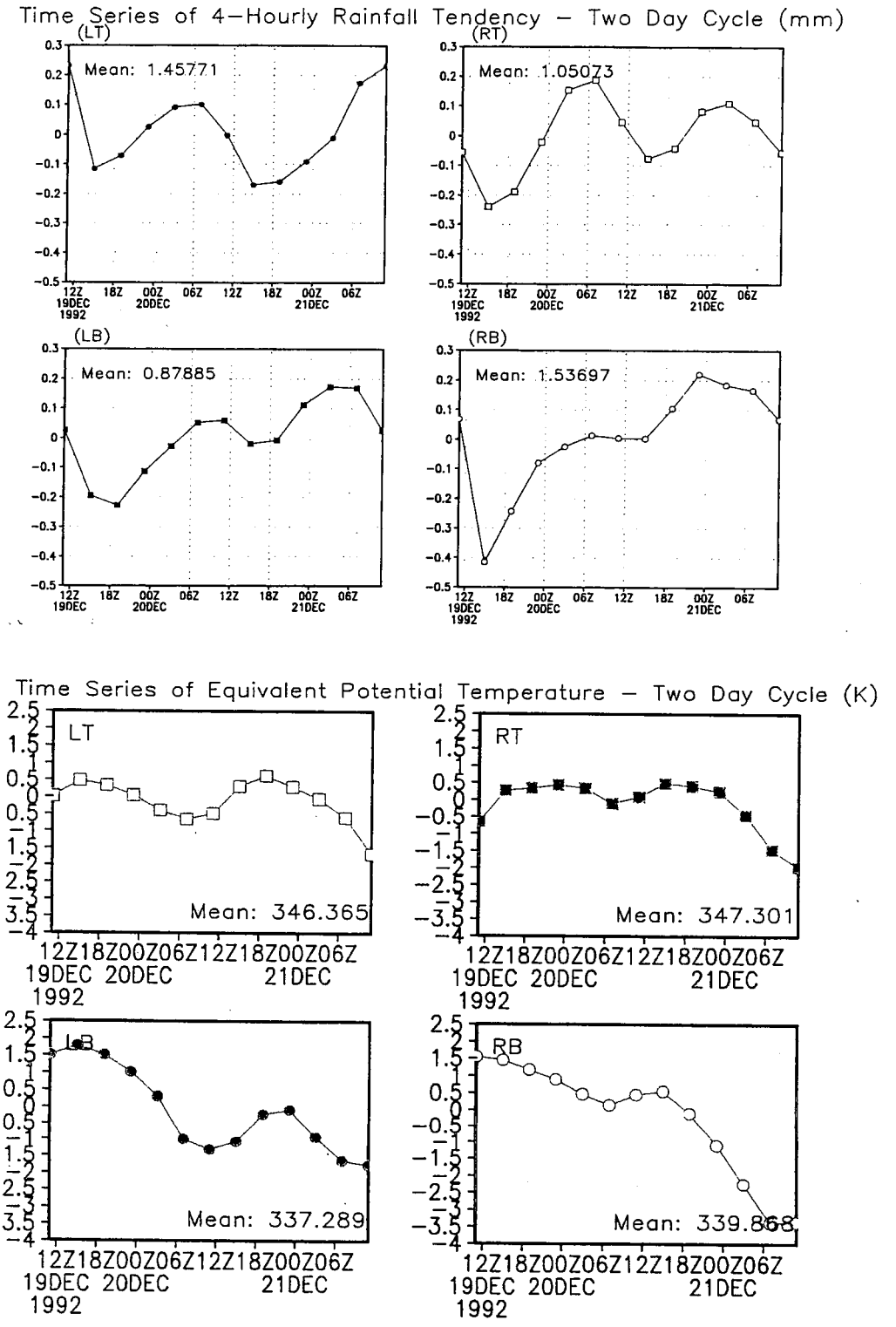


Fig. 17 Four-hour accumulated precipitation field (top 4 panels) and PBL equivalent potential temperature (bottom 4 panels) simulated by MM5 and composited into four quadrants over the west Pacific warm pool region. The MM5 domain extends from 30 S to 20 N and from 150 E to 165 W. Two nested domains with grid resolutions of 135 and 45 km, respectively, were employed. The simulation was run for 12 days, from 19 to 30 December 1992.

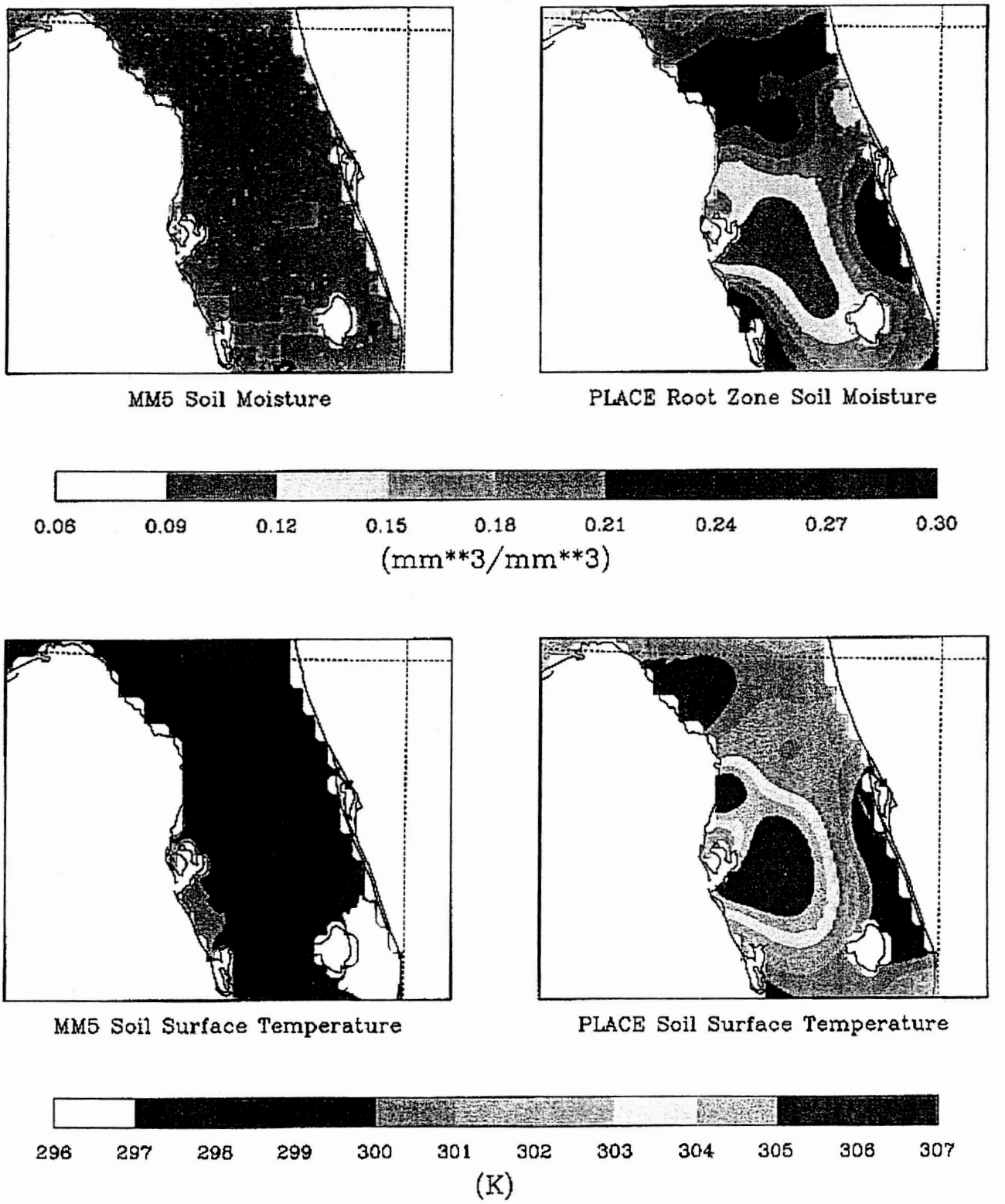


Fig. 18 MM5 preprocessor provided soil moisture (top left) and soil temperature (bottom left). Offline simulations of the PLACE model produced soil moisture and soil temperature fields, shown in plots respectively, at the top right and bottom right. The time was 0000 UTC 27 July 1991. Lake Okeechobee is shown at the lower right corner of the domain. Note that the domain is assumed to contain no grid cells dominated by permanent wetlands. All soils are assumed to be well drained to at least 1-m in depth.

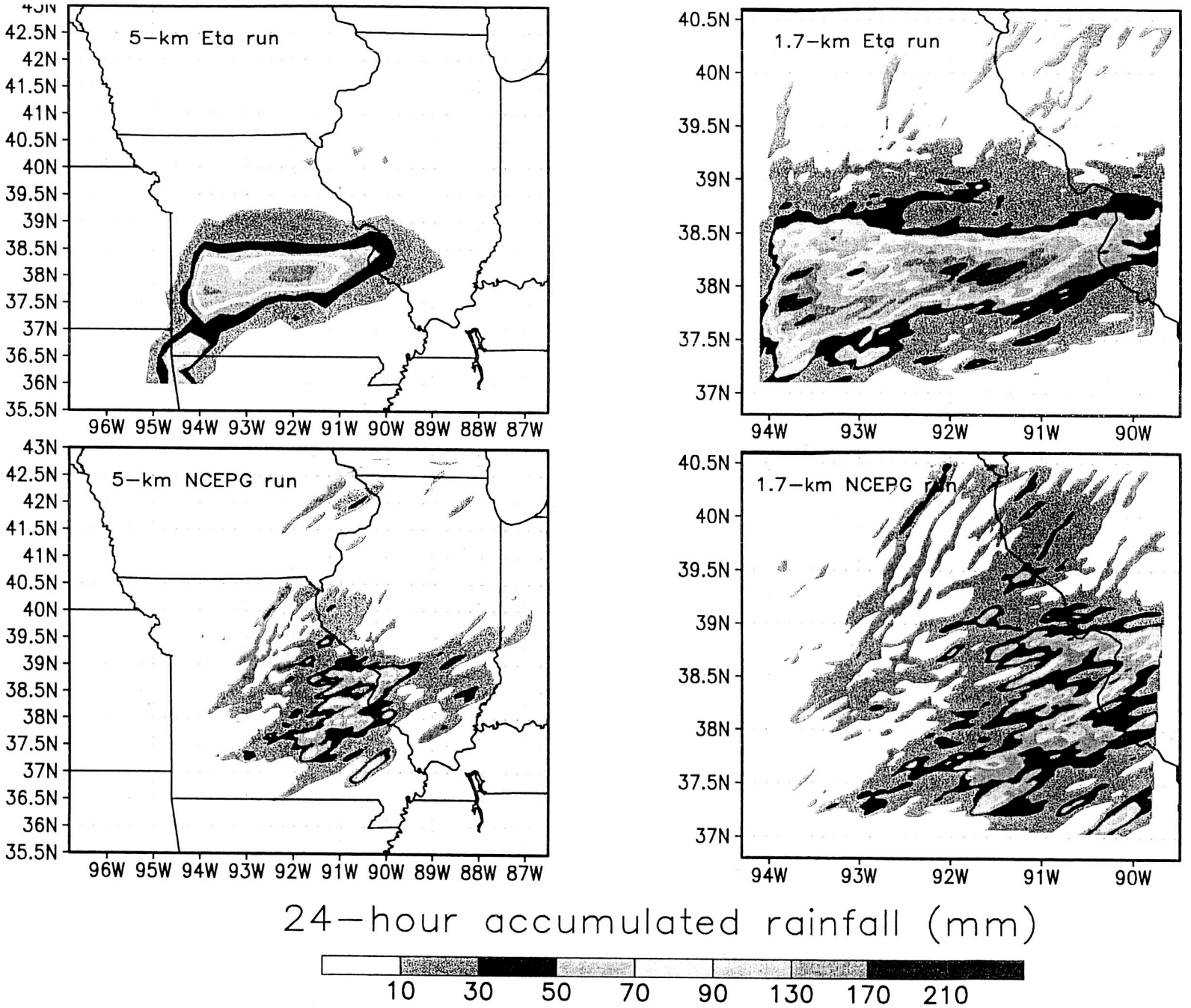


Fig. 19 Twenty four-hour accumulated rainfall for the 6-7 May 2000 Missouri flood simulations: **(a)** 5-km grid spacing with 40-km Eta reanalysis initialization, **(b)** 5-km grid spacing with 2.5 degree NCEP global reanalysis initialization, **(c)** 1.7-km grid spacing with Eta initialization, and **(d)** 1.7-km grid spacing with NCEP initialization. Note that the inner domain in the 5-km runs covers a larger area than the inner domain in the 1.7-km runs.

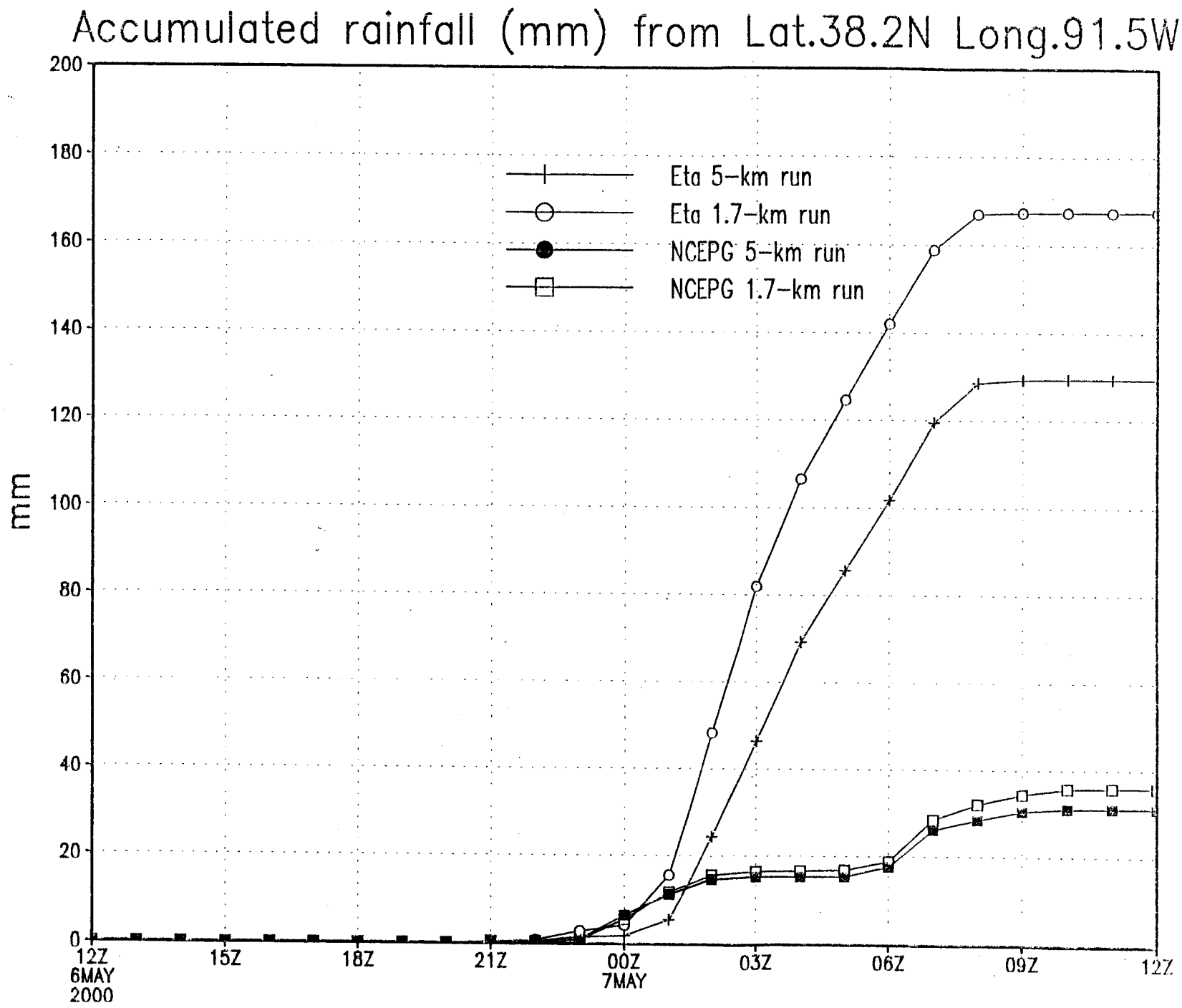


Fig. 20 Time series of accumulated rainfall at 38.2 N, 91.5 W for the four 6-7 May 2000 Missouri flood simulations. This location experienced the heaviest observed rainfall of the event (344 mm).

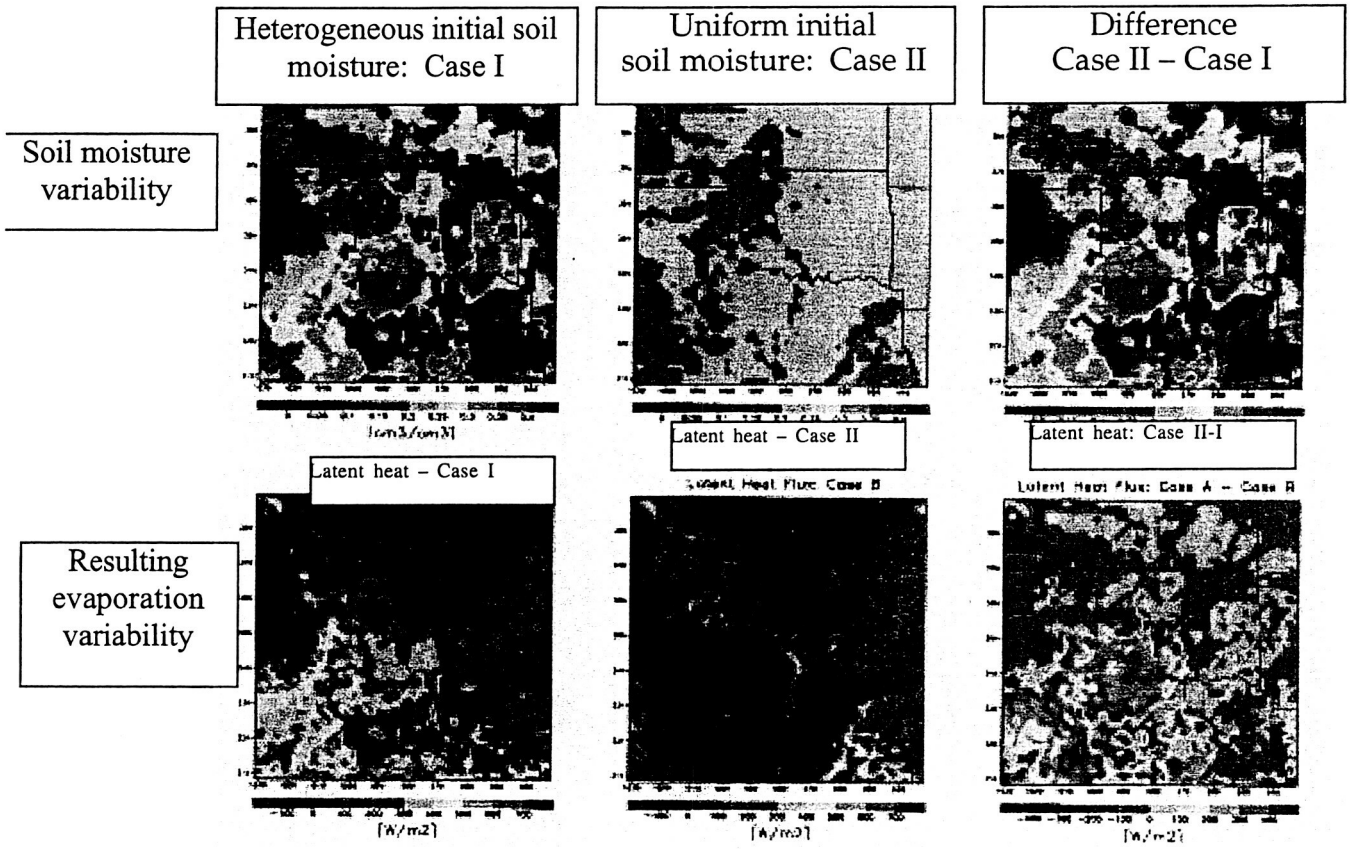


Fig. 21 Influence of soil moisture heterogeneity on land surface latent heat distribution as modeled by MM5-PLACE for June 10, 1992, 12PM local time. Results presented are after six hours of simulation. Cases I and II possess equal domain-averaged initial soil moisture amounts but different sub-domain distributions. The different soil moisture spatial distributions lead to differences in domain-averaged latent heat.

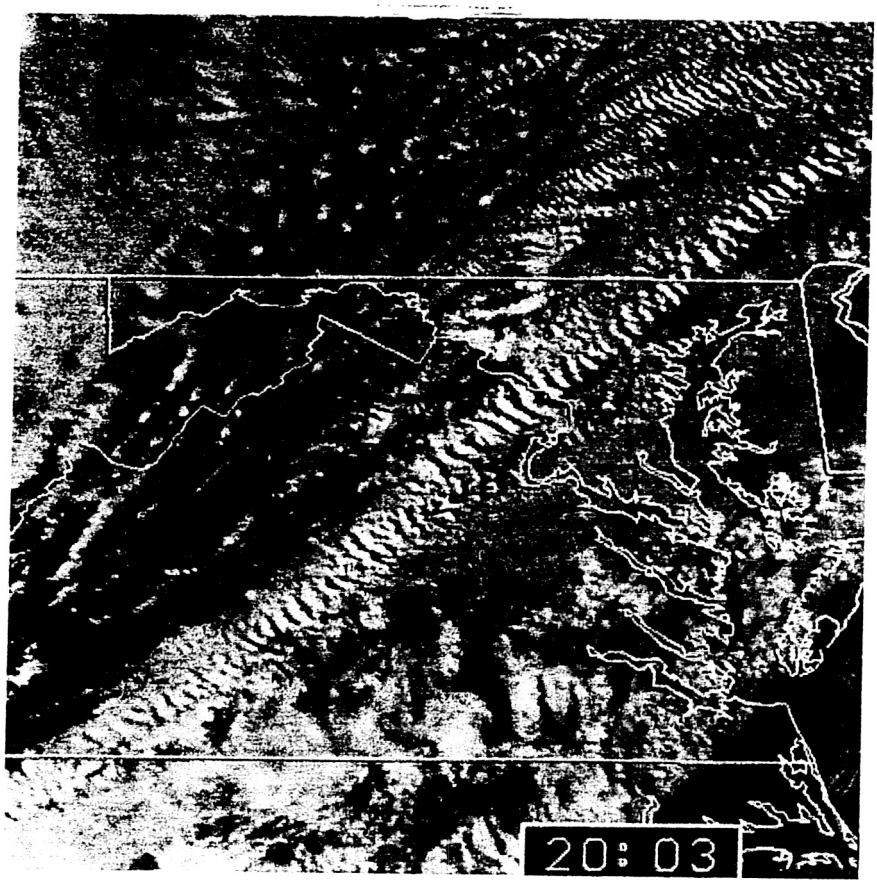


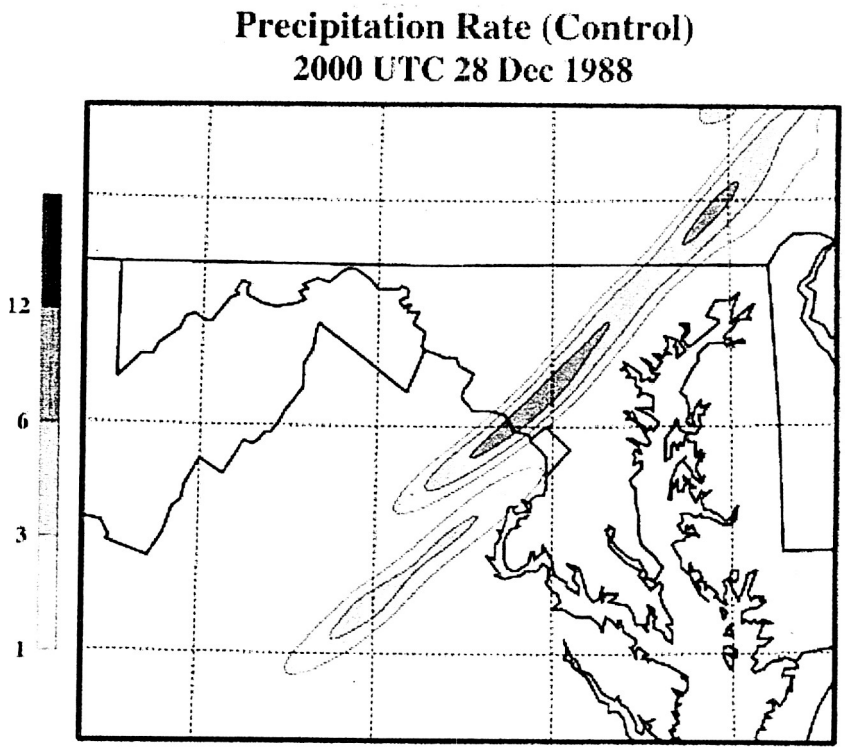


Fig. 22 **(a)** Visible GOES satellite imagery at 2003 UTC 28 December 1988. Note the two bands of convection interconnected with each other in a region from Washington D. C. to Fredericksburg, Virginia (adapted after [56]). **(b)** MM5-simulated rain rate (shaded, mm $h^{-1}$) at 2000 UTC 28 December 1998.

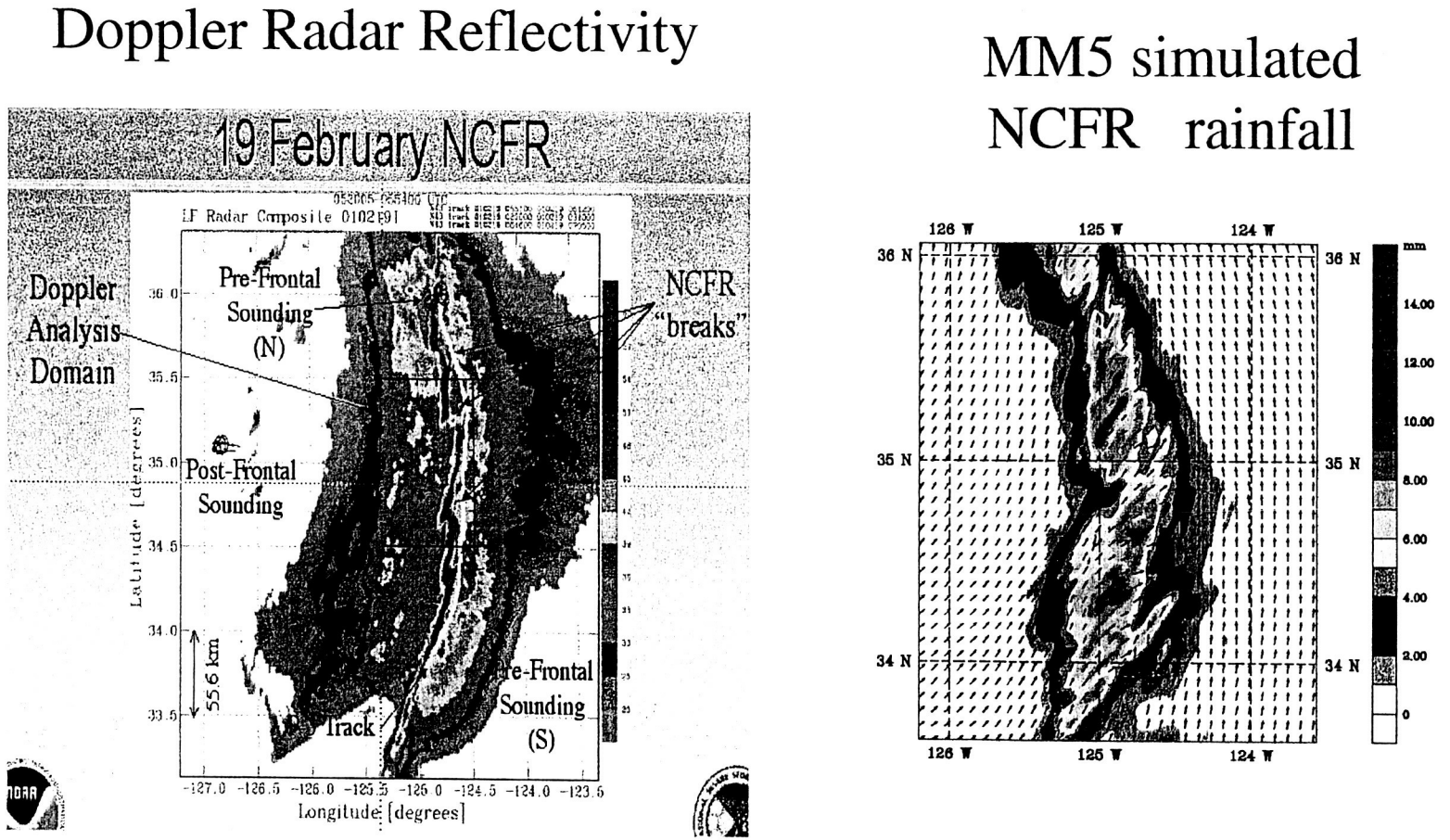


Fig. 23 MM5 was used to simulate a Narrow Cold Frontal Rainband (NCFR) that occurred during PACJET 2001. The numerical simulations were conducted using nested-grids with resolutions of 36km, 12km, 4km and 1.3km. The high-resolution domain was able to reproduce the main structural features of the observed NCFR. The breaks (gaps) along the rainband are well represented. Based on the simulated results, many aspects of NCFR structure depicted in previous studies were confirmed [51].

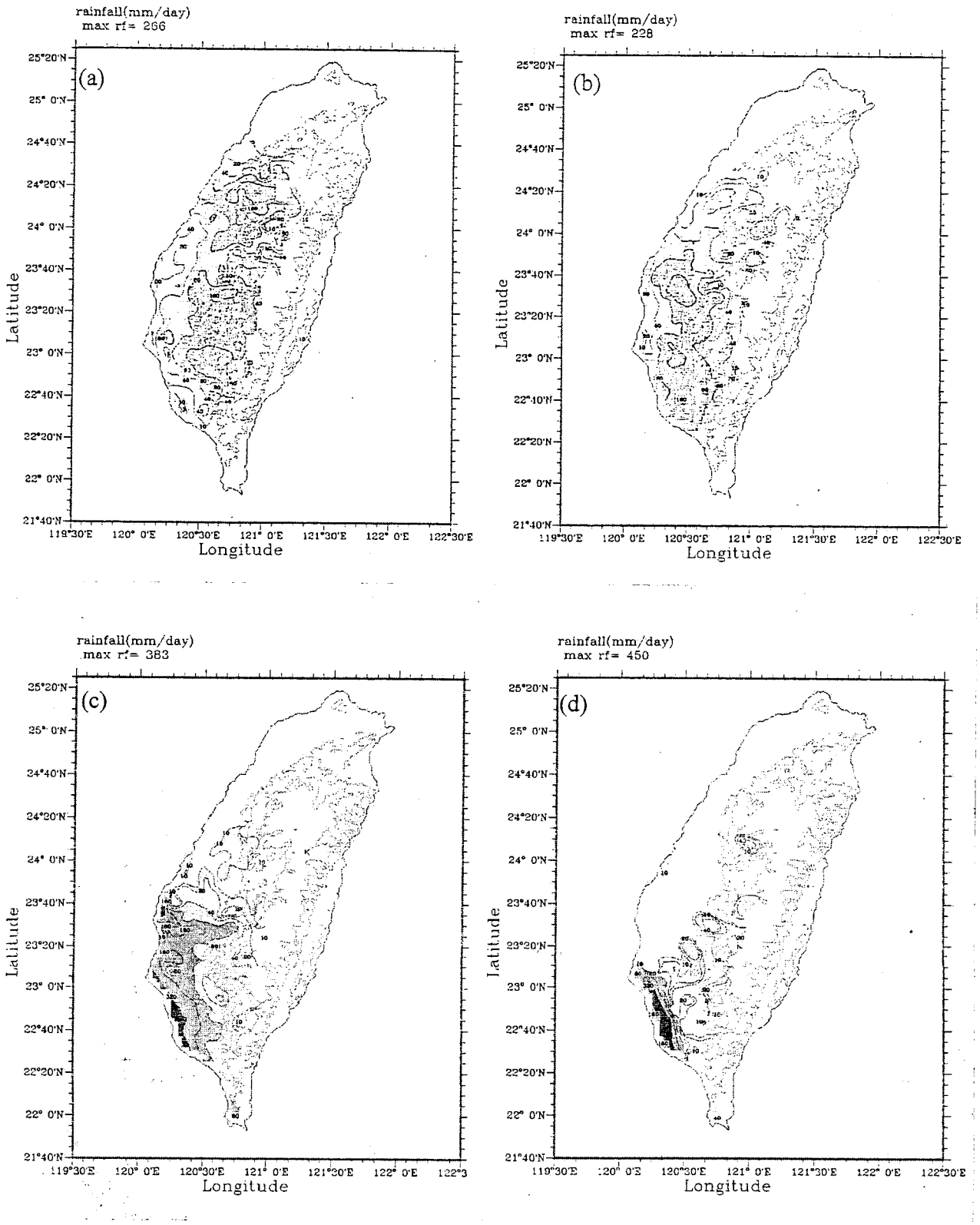


Fig. 24 Daily rainfall amount on **(a)** August 10, **(b)** August 11, **(c)** August 12, and **(d)** August 13, 1994. The contour intervals for topography are 500, 1500, 2500m (dashed lines). The rainfall amount is denoted by the gray scale with 10, 20, 40, 80, 160, 320 and 400 mm. They are estimated by 243 hourly rainfall stations and 22 conventional stations.

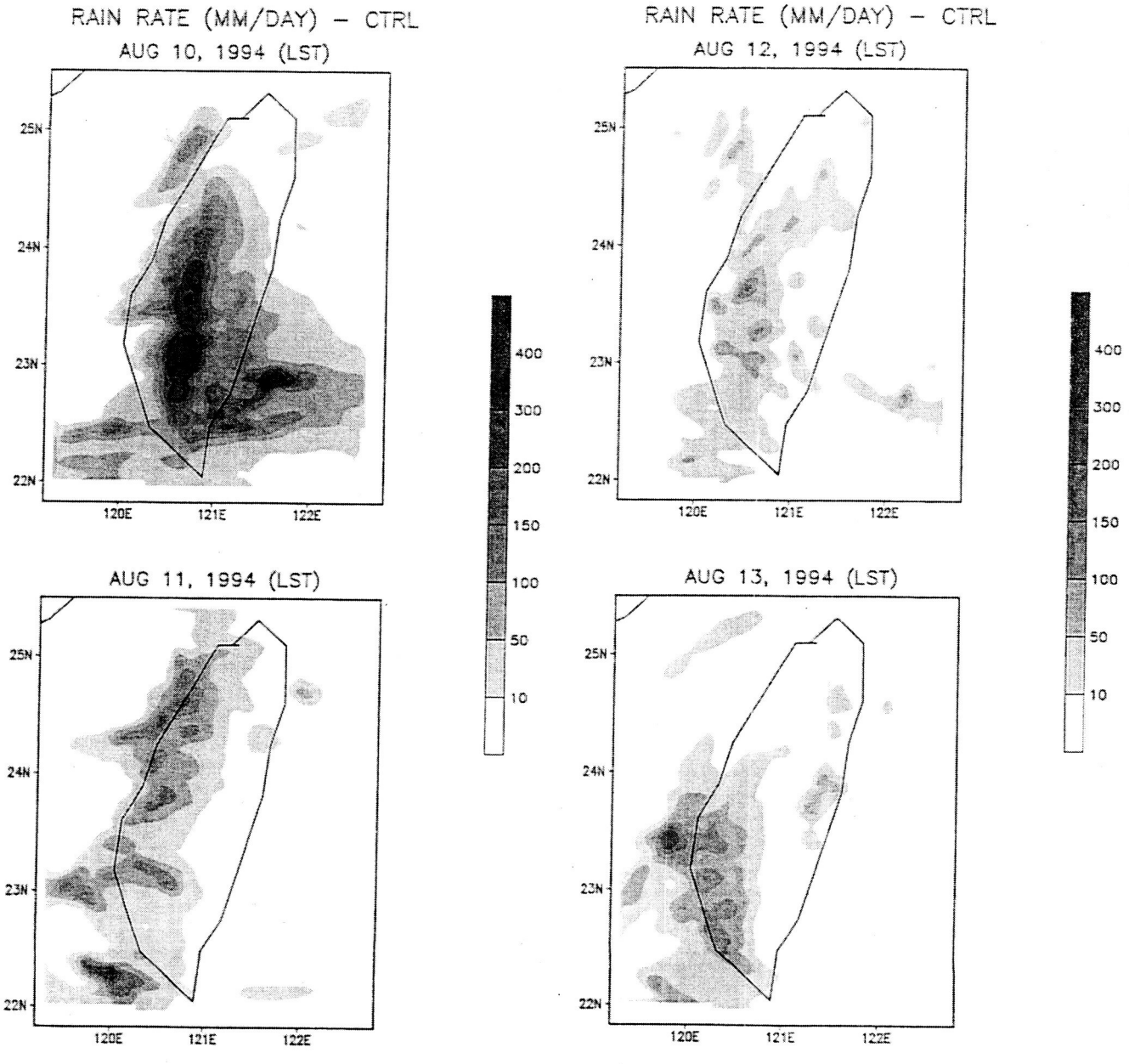


Fig. 25 Daily accumulated rainfall simulated by the MM5 for **(a)** August 10, **(b)** August 11, **(c)** August 12 and **(d)** August 13, 1994. The simulated rainfall is obtained from the 5-km resolution domain. LST stands for local standard time.

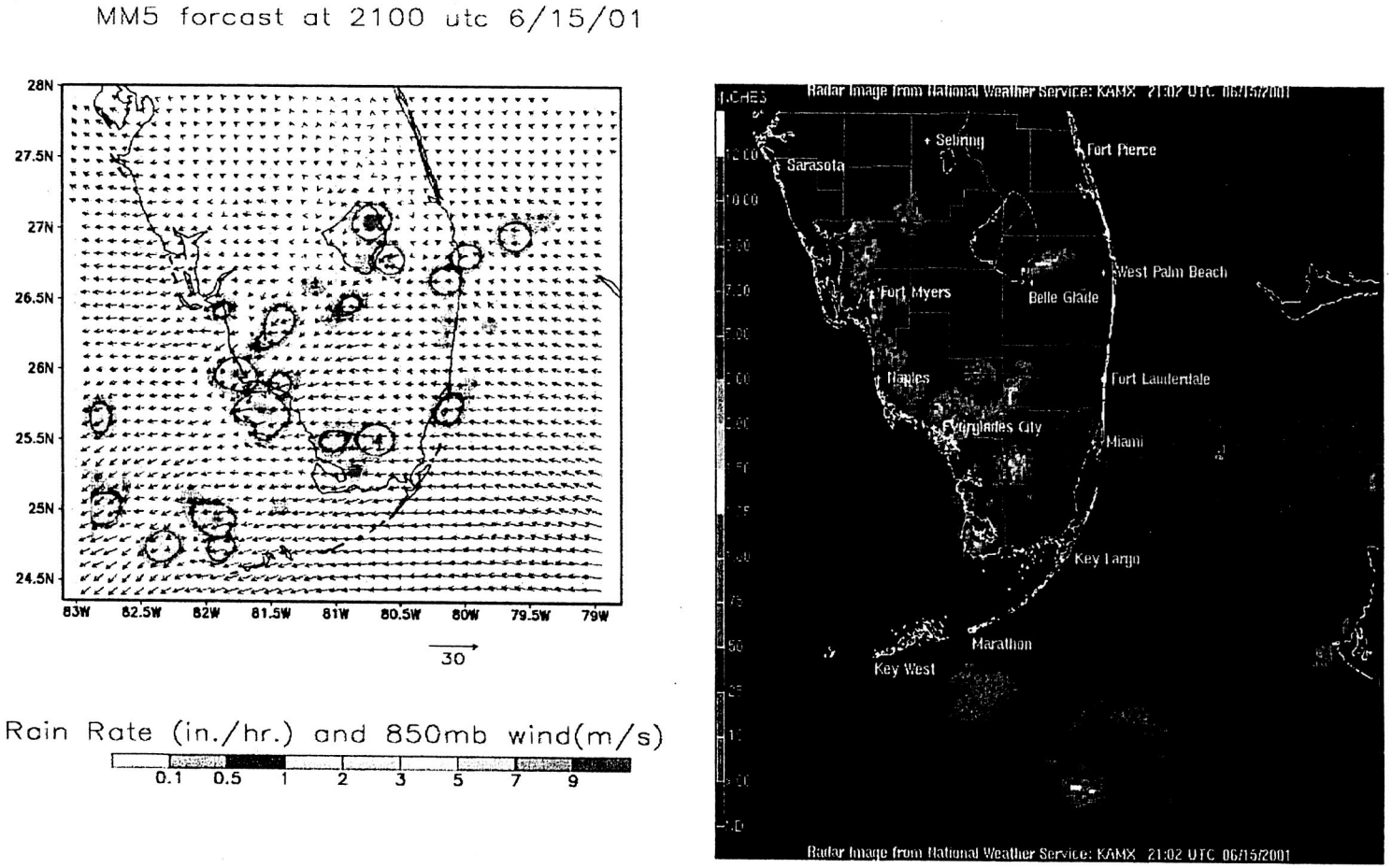


Fig. 26 **(a)** shows the MM5 forecast surface rainfall at 2100 UTC June 15. **(b)** is the NEXRAD radar for comparison.

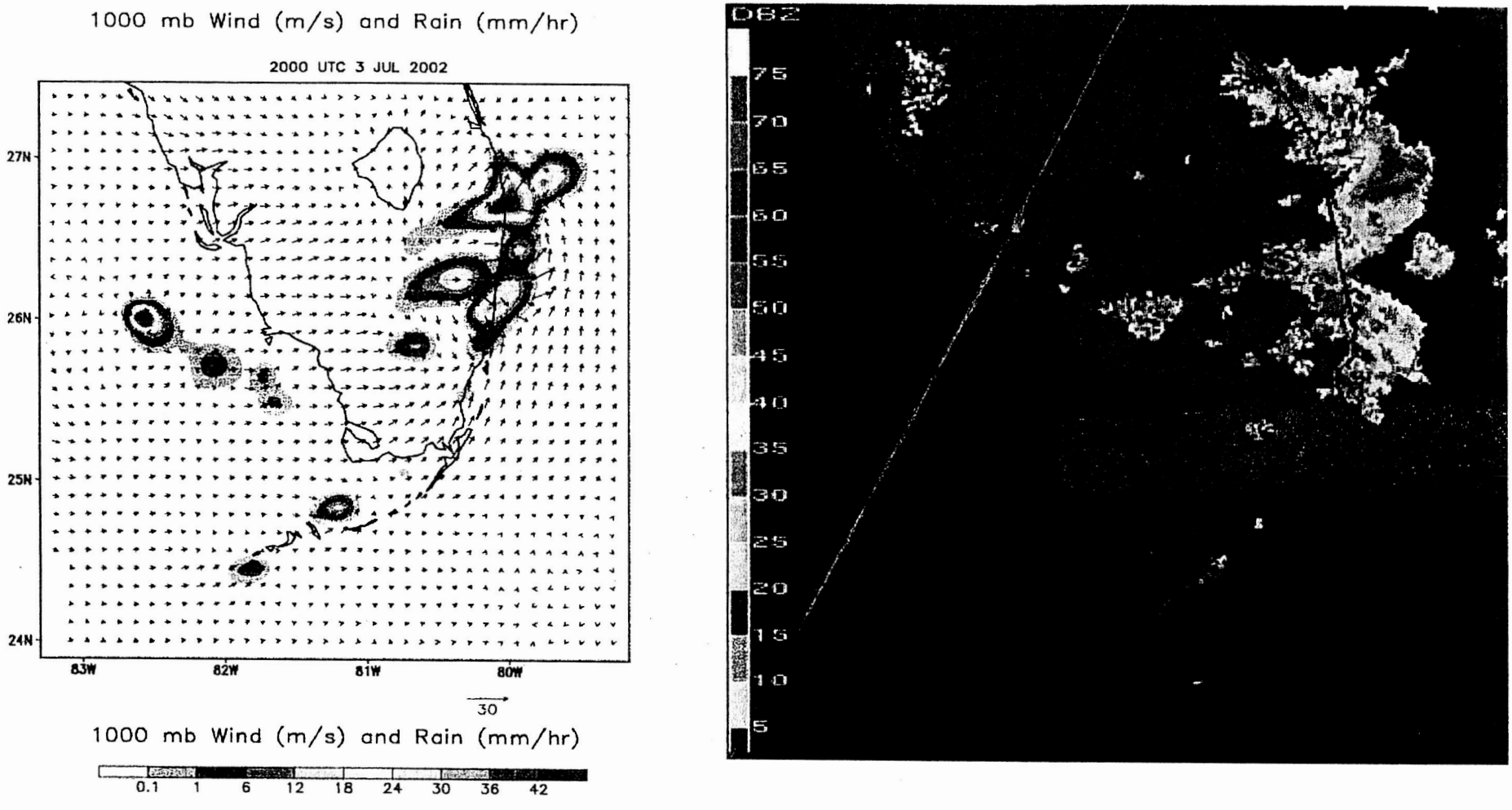


Fig. 27 Same as Fig. 26 except for a sea-breeze convective event.

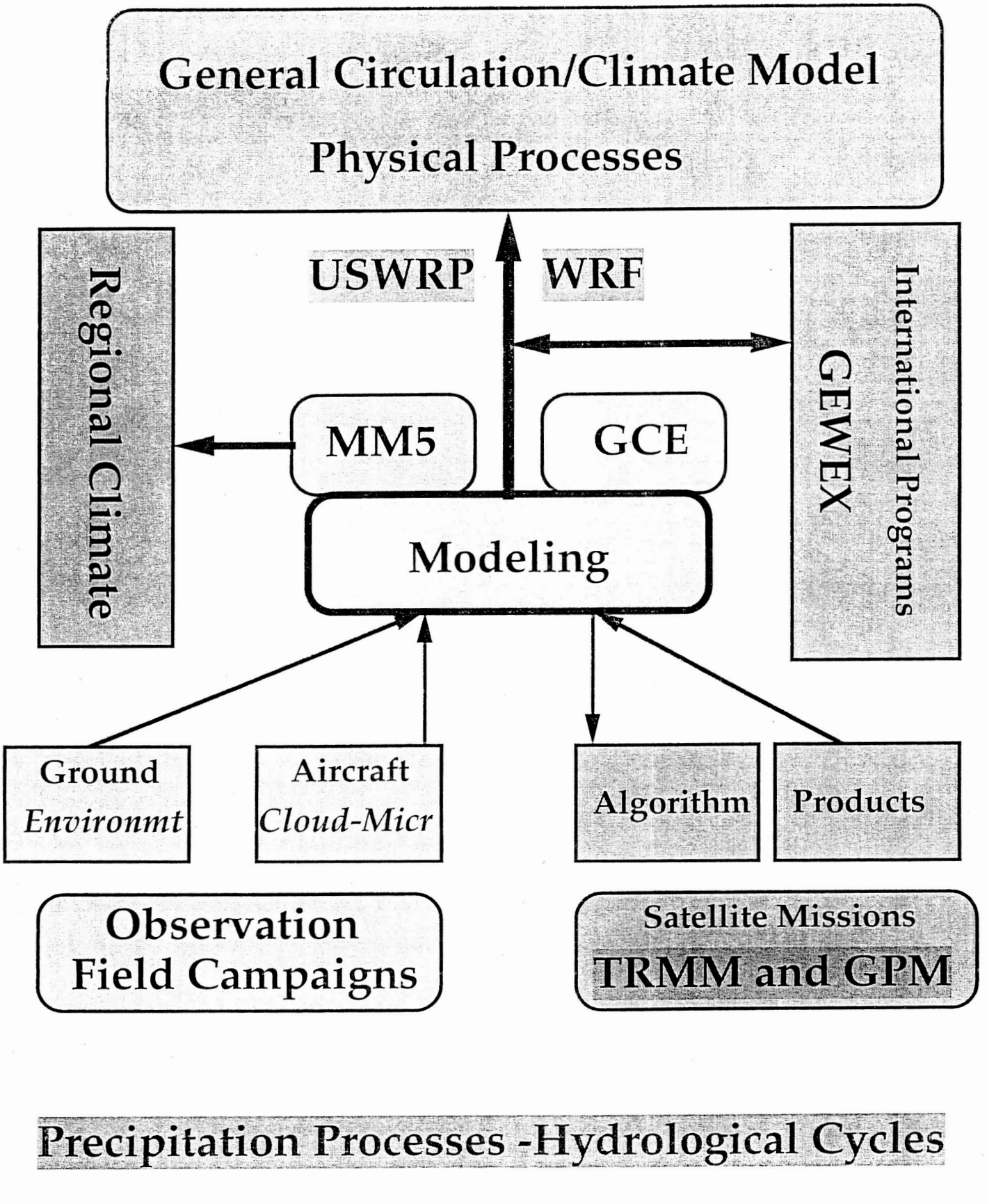


Fig. 28 Schematic diagram shows the regional modeling activities at NASA Goddard Space Flight Center.